



Dipl.-Ing. Patrick Schrey, BSc

Integrated Photodiode Verilog-A Model - Verification and Parameter Extraction

MASTERARBEIT

zur Erlangung des akademischen Grades

Diplom-Ingenieur

Masterstudium Advanced Materials Science

eingereicht an der

Technischen Universität Graz

Betreuer

Univ.-Prof. Ph.D. Peter Hadley

Institut für Festkörperphysik

In Kooperation mit ams AG

EIDESSTATTLICHE ERKLÄRUNG

Ich erkläre an Eides statt, dass ich die vorliegende Arbeit selbstständig verfasst, andere als die angegebenen Quellen/Hilfsmittel nicht benutzt, und die den benutzten Quellen wörtlich und inhaltlich entnommenen Stellen als solche kenntlich gemacht habe. Das in TUGRAZonline hochgeladene Textdokument ist mit der vorliegenden Masterarbeit identisch.

Datum

Unterschrift

Kurzfassung

Moderne Kommunikationstechnologie und der Aufschwung des Smartphone führten zu einem größeren Einsatz von opto-elektronischen Komponenten in integrierten Schaltungen. Ein schneller Entwicklungsvorgang erfordert präzise Simulationsmodelle der verwendeten Bauteile.

Herkömmliche Schaltungssimulatoren unterstützen keine optischen Größen. Deren Einfluss wird mittels elektrischen Ersatzschaltbildern dargestellt um die Implementierung in Schaltungssimulatoren zu ermöglichen. Die Struktur der Ersatzschaltbilder wird von der zugrundeliegenden Physik und den getroffenen mathematischen Vereinfachungen bestimmt. Die elektrischen Größen hingegen werden durch Charakteristiken des opto-elektronischen Bauteils definiert.

Diese Arbeit behandelt das Problem der Verifikation eines Modells und der Anpassung der Parameter anhand einer integrierten Photodiode.

Eine Analyse der opto-elektrischen Effekte wird für die Verifikation des Modells durchgeführt und die wesentlichen Annahmen dargelegt. Eine Strategie zur Parameterextraktion wird durch Variation einzelner Parameter und Beobachtung der daraus resultierenden Veränderung in der Charakteristik der Photodiode entwickelt. Mess- und Simulations-Daten bilden die Grundlage für eine Optimierung der Modellparameter.

Das angepasste Modell wird Schaltungsdesigner in Zukunft für die Simulation neuer opto-elektronischer Systeme zur Verfügung stehen. Neuentwickelte Photodioden können mit der gezeigten Parameterextraktions-Strategie in die Entwicklungsumgebung integriert werden.

Abstract

Integrated opto-electronic devices have become increasingly important due to the rise of smart phones and modern communication technology.

Traditional circuit simulation tools do not provide the designer with opto-electronic components or optical signals. Typically, equivalent circuits are used in order to mimic the opto-electronic behavior. Photophysics determines the structure of the equivalent circuit for a certain type of device, while the values of the equivalent circuit components are defined by the characteristics of the particular opto-electronic device. Accurate device models for circuit simulation lead to shorter development processes.

This thesis presents the verification of a photodiode model and the adjustment of its parameters according to measurements and simulation results.

An analysis of opto-electronic effects will verify the model, its assumptions and simplifications. The observation of the photodiode characteristics while changing the parameters results in a parameter extraction strategy.

The model enables designers to simulate future opto-electronic systems. Newly created photodiodes are integrated into the design environment using the proposed parameter extraction strategy.

Contents

1	Introduction	1
2	Fundamentals	3
2.1	Basic Physics	4
2.1.1	Absorption	7
2.1.2	Loss Mechanism	9
2.1.3	Reflection in Multi-layered Material	11
2.2	Photodiodes	16
2.2.1	Working Principle	16
2.2.2	Characteristics of Photodiodes	18
2.2.3	Structures of Photodiodes	22
3	Model Verification	25
3.1	Depletion Layer	26
3.2	Quasi-neutral Regions	30
3.2.1	n-Well Region	33
3.2.2	Bulk Quasi-neutral Region	35
3.3	Equivalent Circuit	47
4	Parameter Extraction Strategy	49
4.1	Parameters	50
4.2	Responsivity Parameter Extraction	52
4.3	Frequency Response Parameter Extraction	53
4.4	Extraction Strategy	54
5	Measurement of Photodiode Characteristics	55
5.1	Responsivity Measurement	58
5.2	Frequency Response Measurement	62
6	Parameter Optimization and Results	69
6.1	Responsivity Fitting	70
6.2	Frequency Response Fitting	71
7	Conclusion	75
A	Laplace Transformation of Transient Response	78

List of Figures

2.1	Absorption coefficient as a function of wavelength	8
2.2	Generation and recombination in an intrinsic direct-band semiconductor . .	9
2.3	Generation and recombination in an extrinsic direct-band semiconductor . .	10
2.4	Leakage current in an exemplary structure	10
2.5	Optical wave impinging on a coated surface	12
2.6	Transmittance of a TARC and a BARC	15
2.7	Charge carrier separation in a p-n-photodiode.	16
2.8	Divergence of current density changes charge carrier concentration	18
2.9	Exemplary responsivity plot	21
2.10	Structure of a p-n- and a p-i-n-photodiode.	22
2.11	Different structures of anti-reflective coatings.	24
3.1	Geometry for the model verification.	26
3.2	Exemplary doping profile of a photodiode.	27
3.3	Equivalent circuit of a photodiode with epitaxial grown layer	48
4.1	Parameter <i>dbarc</i> sets BARC thickness	50
4.2	<i>dnpp</i> and <i>aE</i> inside the photodiode	50
4.3	Responsivity parameter impact	52
4.4	Frequency response parameter impact at 670 nm	53
4.5	Frequency response parameter impact at 850 nm	54
5.1	Photo of the opto-laboratory	55
5.2	Photo of a wafer inside the prober	56
5.3	Photo of the fiber assembly	56
5.4	Fiber position over a photodiode	57
5.5	Schematic for light source calibration	58
5.6	Responsivity measurement setup	59
5.7	p-i-n-photodiode measured current and optical power	60
5.8	p-i-n-photodiode responsivity measurement result	60
5.9	Frequency response measurement setup	62
5.10	Frequency response measurement setup equivalent circuit	64
5.11	p-i-n-photodiode transient response measurement results for 670 nm	65
5.12	p-i-n-photodiode transient response measurement results for 850 nm	65
5.13	Fit of the p-i-n-photodiode transient response for 670 nm	66
5.14	Fit of the p-i-n-photodiode transient response for 850 nm	66

5.15	p-i-n-photodiode Bode plot for 670 nm illumination	67
5.16	p-i-n-photodiode Bode plot for 850 nm illumination	67
6.1	Fitted Responsivity	70
6.2	Frequency response for 670 nm illumination	71
6.3	Fitted frequency response for 850 nm illumination	72
6.4	Transient response for 670 nm illumination	73
6.5	Transient response for 850 nm illumination	73
6.6	Comparison between measurement, model output and TCAD simulation . .	74

List of Tables

2.1	Refractive indices for the calculation of the transmittance	14
4.1	Parameter optimization order	54
5.1	Equipment for responsivity measurement	59
5.2	Equipment for frequency response measurement	63
6.1	Fitted parameter for responsivity	70
6.2	Fitted parameter for frequency response	72

List of Symbols

Symbol	Unit	Description
a	$1/\text{m}^4$	Impurity gradient
A	m^2	Area
α	$1/\text{m}$	Absorption coefficient
c	m/s	Speed of light in vacuum
C	F	Capacitance
D	m^2/s	Diffusion constant
δ	1	Phase delay
\mathbf{e}	1	Unit vector
E	J	Energy
\mathbf{E}	V/m	Electric field
ϵ	F/m	Permittivity, dielectric constant
ϵ_0	F/m	Permittivity of free space, dielectric constant of free space
ϵ_r	1	Relative permittivity, relative dielectric constant
f	Hz	Frequency
G	$1/\text{s}$	Generation rate
h	$\text{J} \cdot \text{s}$	Planck constant
\hbar	$\text{J} \cdot \text{s}$	Reduced Planck constant
\mathbf{H}	A/m	Magnetic field
H	1	Transfer function, frequency response
I	A	Electric current
j	1	Imaginary unit
\mathbf{J}	A/m^2	Current density
\mathbf{k}	$1/\text{m}$	Wave vector
k_B	J/K	Boltzmann constant
K	1	Extinction coefficient
L	m	Diffusion length or mean free path
λ	m	Wavelength
m	1	Quality factor
μ	$\text{m}^2/(\text{V} \cdot \text{s})$	Mobility
μ_m	H/m	Permeability
μ_0	H/m	Permeability of free space
μ_r	1	Relative permeability
n	1	Refractive index

Symbol	Unit	Name
n	$1/\text{m}^3$	Electron density
n_{ph}	1	Number of photons
\mathbf{n}	1	Normal unit vector
N	$1/\text{m}^3$	Doping concentration
ω	$1/\text{s}$	Angular frequency
p	$1/\text{m}^3$	Hole density
\mathbf{p}	$\text{kg} \cdot \text{m}/\text{s}$	Momentum
P	W	Power
Φ	$1/(\text{m}^2 \cdot \text{s})$	Photonic flux
q	C	Elementary charge
Q	C	Electric charge
QE	1	Quantum efficiency
$\vec{\mathbf{r}}$	m	Position vector
R	Ω	Electrical resistance
R	1	Reflectance, reflection coefficient
\mathfrak{R}	A/W	Responsivity
s	$1/\text{s}$	Complex frequency
S	m/s	Surface recombination velocity
\mathbf{S}	W/m^2	Poynting vector, Intensity
σ	m^2	Capture cross section
ς	1	Step function, Heavyside function
t	s	Time
T	K	Temperature
T	1	Transmittance, transmission coefficient
τ	s	Life time
Θ	rad	Angle measured from the interface normal
U	$1/\text{s}$	Recombination rate
\mathbf{v}	m/s	Velocity
V	V	Voltage
\mathbf{V}	m^3	Volume
x	m	Position in one dimension
ξ	1	Collection efficiency
Y	S	Admittance
Z	Ω	Impedance

Chapter 1

Introduction

Motivation

The daily use of the internet and hand-held devices such as smart phones requires high data rates. Optical fiber networks have been established and free-space optical communication systems seem promising to tackle data traffic and security demands. Integrated circuits (IC) on the other hand are the electronic backbone of data processing. The incident optical signal has to be transformed into an electrical one at the receiver. Photodiodes allow for the transformation of impinging light into electrical current. Accuracy of measurement equipment like optical spectrometers depends on the properties of this transformation. But available commercial circuit simulation software covers the electrical domain only. Optical signals and light sources are represented by electrical components. Faster development of opto-electronic integrated circuits (OEIC) requires accurate results of DC, AC and transient simulations.

Problem

Several photodiode models for device and circuit simulation have been published in the past [1, 2, 3, 4, 5, 6, 7]. These models come up with different implementation techniques and assumptions. Each of which simplifies the expression for the generated photocurrent to integrate the obtained model into the simulation environment. Considering all contributing effects in a photodiode would lead to an inappropriate complex model and long simulation cycles. Photodiode models are created with a set of problems in mind. These models solve their corresponding problems only and are less suitable for other issues. A model for a p-n-photodiode for example will not be able to represent an avalanche photodiode.

Photodiode models and their parameters are valid for a few process technologies only. As long as the device structure is conserved it is sufficient to adapt the model parameters to the new process or device. The physics based relations of the model can be reused. This thesis reports on the parameter modification of a photodiode model to a different manufacturing process.

A Verilog-A photodiode model shall be adjusted to match experimentally obtained data. The measurement of device characteristics include the responsivity \mathfrak{R} and frequency response $H(f)$. In order to predict the measurement results by simulation the parameters of the model have to be adjusted by a least-mean-square fit. The model is simulated in Matlab for future parameter optimization. The model has to be validated by comparison of the simulation and measurement results.

A brief discussion on basic photodiode physics is given at the beginning to understand the performed measurements and model parameters. The influence of certain parameters on characteristics of the photodiode and the extraction strategy are presented followed by an explanation of the measurement principles. In order to validate the model simulation results are compared to test readings. A summary and a concluding discussion of the obtained model finalizes the thesis.

Chapter 2

Fundamentals

This chapter covers principle physics and describes photodiode structures in order to understand how a photodiode works. In this progress terms used throughout this thesis are clarified.

Basic properties of light and materials are discussed first. Charge carrier generation and recombination as well as their movement are covered. A detailed outline of the absorption process and the loss mechanisms follows since both have a major impact on the photodiodes behavior. Beside these opto-electric phenomena pure optical ones like transmission and reflection in multiple layers are examined.

Typical photodiode structures, the p-n- and the p-i-n-photodiode are presented in order to demonstrate the working principle. Additional anti-reflective coatings (ARC) deposited on top of photodiodes in order to enhance their performance are discussed.

Photodiode characteristics compare different photodiodes in certain aspect like response speed and conversion efficiency. Frequency response along with dark current, capacitance and responsivity are the photodiode characteristics treated in this thesis.

2.1 Basic Physics

Light is the most prominent subject of the wave-particle duality. It has to be regarded as wave and particle at the same time to wholly describe its properties. In a bottom-up approach the characteristics of photons are covered first.

As any particle a photon has a momentum \vec{p} , which corresponds to a de Broglie wavelength λ given by

$$\vec{p} = \hbar \cdot \vec{k} = \frac{h}{\lambda} \cdot \vec{e}_k \quad (2.1)$$

where \vec{k} is the wave vector and \vec{e}_k the unit vector pointing in the direction of \vec{k} . h and \hbar are the Planck constant and the normalized Planck constant, respectively. The energy E_{ph} of a single photon is determined by the Planck-Einstein-relation. Either the frequency f , the angular frequency ω or the wavelength can be used to calculate the photon energy.

$$E_{ph} = h \cdot f = \hbar \cdot \omega = \frac{h \cdot c}{\lambda} \quad (2.2)$$

The wavelength dependence of the photon energy will be particular important when discussing the absorption process in a semiconductor. Only a photon with sufficient energy, i.e. short wavelength will be absorbed and creates an electron-hole pair.

While the energy of a single photon is well defined the energy E_{Beam} and power P_{Beam} of a light beam are not. There is no detailed information on the illuminated area A nor the location where the photons impinge. Instead of the beam power P_{Beam} the intensity \vec{S} is used. The intensity gives the power transferred to a unit area. The light exposed area A with normal vector \vec{n}_A is used to relate the intensity with the beam power.

$$P_{Beam} = \int \vec{S} \circ \vec{n}_A dA \quad (2.3)$$

Later on the power transferred to a surface is of little interest. The flux density $\vec{\Phi}$ will be more important. The flux density gives the number of photons passing through a certain area per time. It is related to the intensity by

$$\vec{\Phi} = \frac{\vec{S}}{E_{ph}} \quad (2.4)$$

The properties of light as a particle stream have been outlined up to now. The idea of a photon is useful when interactions between particles are of interest.

For the analysis of macroscopic effects like interference the interpretation of light as an electromagnetic wave is advantageous. Therefore a brief discussion on wave properties will be given next.

An electrical wave \vec{E} for example is described by

$$\vec{E} = \hat{E} \cdot e^{j \cdot (\vec{k} \circ \vec{r} - \omega \cdot t)} \cdot \vec{e}_E \quad (2.5)$$

where $\hat{\mathbf{E}}$ is the amplitude, $\vec{\mathbf{r}}$ the position vector into the direction of motion and $\vec{\mathbf{e}}_E$ the unity vector in direction of the electric field. The hollow circle represents the dot product of two vectors.

A wave propagating in x -direction and omitting the vector notation is given as

$$\mathbf{E} = \hat{\mathbf{E}} \cdot e^{j \cdot \left(\frac{2 \cdot \pi}{\lambda} \cdot x - \omega \cdot t\right)} \quad (2.6)$$

In order to determine the velocity \mathbf{v} one has to determine a relation between x and t . Therefore a certain point, e.g. a extrema of the wave is tracked. Arbitrarily tracing a maxima of the wave means the exponent must be 0.

$$\frac{2 \cdot \pi \cdot x}{\lambda} \stackrel{!}{=} \omega \cdot t \quad (2.7)$$

The derivative of the function $x(t)$ gives the velocity of the wave

$$\begin{aligned} \mathbf{v} &= \frac{dx}{dt} \\ \mathbf{v} &= \frac{\lambda \cdot \omega}{2 \cdot \pi} \end{aligned} \quad (2.8)$$

When the wave travels through a material its velocity is determined by the dielectric constant or electric permittivity ϵ and the magnetic permeability μ_m as material properties.

$$\mathbf{v} = \frac{1}{\sqrt{\epsilon \cdot \mu_m}} \quad (2.9)$$

The permittivity and permeability are composed of a vacuum and a relative component.

$$\begin{aligned} \epsilon &= \epsilon_0 \cdot \epsilon_r \\ \mu_m &= \mu_0 \cdot \mu_r \end{aligned}$$

The speed of light in vacuum is obtained by equation 2.9 and setting the relative permittivity ϵ_r and permeability μ_r to 1.

$$c = \frac{1}{\sqrt{\epsilon_0 \cdot \mu_0}} \quad (2.10)$$

The velocity of the wave in a medium is related to the speed of light in vacuum by combining equation 2.9 and 2.10.

$$\mathbf{v} = \frac{c}{\sqrt{\epsilon_r \cdot \mu_r}} \quad (2.11)$$

In most materials in optical applications the relative permeability μ_r can be considered unity. Thus equation 2.11 simplifies to

$$\mathbf{v} = \frac{c}{\sqrt{\epsilon_r}} \quad (2.12)$$

The relative dielectric constant ϵ_r is wavelength dependent. This can be seen by combining equations 2.8 and 2.12.

$$\sqrt{\epsilon_r} = \frac{2 \cdot \pi \cdot c}{\lambda \cdot \omega} \quad (2.13)$$

The refractive index n and the extinction coefficient K are related to the dielectric constant.

$$\sqrt{\epsilon_r} = n + j \cdot K \quad (2.14)$$

Furthermore as the relative dielectric constant ϵ_r is wavelength dependent the refractive index n and the extinction coefficient K change with λ .

Replacing λ in equation 2.6 with the velocity \mathbf{v} given in equation 2.8

$$\mathbf{E} = \hat{\mathbf{E}} \cdot e^{j \cdot \omega \cdot (\frac{x}{v} - t)} \quad (2.15)$$

Substitution of the velocity by equation 2.12 and the dielectric constant by equation 2.14 results in

$$\mathbf{E} = \hat{\mathbf{E}} \cdot e^{j \cdot \omega \cdot (n \cdot \frac{x}{c} - t)} \cdot e^{-\omega \cdot K \cdot \frac{x}{c}} \quad (2.16)$$

The first exponential is a harmonic oscillation while the second one describes the decrease of the electric field along x due to extinction.

The counterpart of the intensity in the wave regime is known as the Poynting vector $\vec{\mathbf{S}}$ which equals the vector product of the electrical field $\vec{\mathbf{E}}$ and the magnetic field $\vec{\mathbf{H}}$.

$$\vec{\mathbf{S}} = \vec{\mathbf{E}} \times \vec{\mathbf{H}} \quad (2.17)$$

Replacing the vectors with their magnitudes and unit vectors gives

$$\begin{aligned} \mathbf{S} \cdot \vec{\mathbf{e}}_S &= (\mathbf{E} \cdot \vec{\mathbf{e}}_E) \times (\mathbf{H} \cdot \vec{\mathbf{e}}_H) \\ \mathbf{S} \cdot \vec{\mathbf{e}}_S &= \mathbf{E} \cdot \mathbf{H} \cdot (\vec{\mathbf{e}}_E \times \vec{\mathbf{e}}_H) \end{aligned}$$

The electric and magnetic field are related to each other by [8]

$$\sqrt{\mu_m} \cdot \mathbf{H} = \sqrt{\epsilon} \cdot \mathbf{E} \quad (2.18)$$

Therefore the Poynting vector can be written as

$$\mathbf{S} \cdot \vec{\mathbf{e}}_S = \frac{\sqrt{\epsilon}}{\sqrt{\mu_m}} \cdot \mathbf{E}^2 \cdot (\vec{\mathbf{e}}_H \times \vec{\mathbf{e}}_E) \quad (2.19)$$

2.1.1 Absorption

Absorption means a photon is consumed somehow inside the semiconductor. This process is directly related to the extinction coefficient K mentioned in section 2.1. Absorption can be investigated in the wave and particle representation of light.

The magnitude of the Poynting vector as given in equation 2.19 for the electric field in equation 2.6 equals

$$\mathbf{S} = \frac{\sqrt{\epsilon}}{\sqrt{\mu_m}} \cdot \hat{\mathbf{E}}^2 \cdot e^{j \cdot 2 \cdot \omega \cdot \left(n \cdot \frac{x}{c} - t\right)} \cdot e^{-2 \cdot \omega \cdot K \cdot \frac{x}{c}} \quad (2.20)$$

where the absorption coefficient α is introduced as

$$\alpha = \frac{2 \cdot \omega \cdot K}{c} \quad (2.21)$$

The Poynting vector can be expressed by the photonic flux Φ as given in equation 2.3. Thus absorption leads to an exponential decrease in the magnitude of the Poynting vector and photonic flux Φ .

$$\mathbf{S} \sim \Phi \sim e^{-\alpha \cdot x} \quad (2.22)$$

Note the dependence of the absorption coefficient α on the angular frequency ω of the impinging light given in equation 2.21. Furthermore the angular frequency is related to the wavelength λ by equation 2.8. Therefore absorption increases with decreasing wavelength λ . Figure 2.1 shows the absorption over wavelength for different materials and temperatures.

A mechanism for absorption in a semiconductor is the excitation of an electron-hole pair. Since this thesis reports on photodiodes the word absorption will be used as a synonym for photoexcitation. Intrinsic photoexcitation means a band-to-band transition. Extrinsic photoexcitation involves transition between forbidden-gap energy levels and the valence or conduction band. Therefore the critical photon energy for extrinsic photoexcitation is less than the intrinsic one.

For an intrinsic semiconductor the photons energy must exceed the band gap energy E_g . Since energy E_{ph} and wavelength λ are related to each other by equation 2.2 there is a maximum wavelength λ_c a certain semiconductor may absorb [9].

$$\lambda_c = \frac{h \cdot c}{E_g} \quad (2.23)$$

The semiconductor is transparent for photons with longer wavelength than the critical wavelength λ_c . This is called the long-wavelength cutoff.

The aforementioned absorption coefficient α is a crucial quantity when investigating optoelectronic devices. On the right hand side of figure 2.1 the light penetration depth is given as the reciprocal of the absorption coefficient. Long wavelength light penetrates deep into the semiconductor. One can see that for a short wavelength the penetration depth is small and the photons will be absorbed near the surface. Due to the high defect density near the surface the lifetime is very short and most of the charge carriers cannot be collected

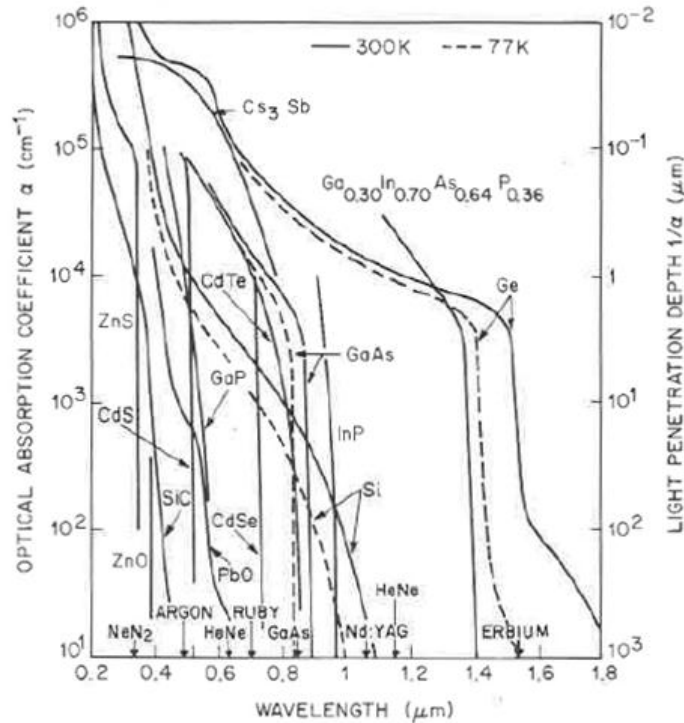


Figure 2.1: Absorption coefficient α as a function of wavelength λ for different semiconductors. Solid lines for 300K, dashed lines for 77K [9], page 750.

by the electric field of the depletion region. This leads to a short-wavelength cutoff for the photodiode.

Furthermore figure 2.1 indicates the temperature dependence of the absorption coefficient. The absorption coefficient α in Silicon for example increases with increasing temperature T due to the decreasing band gap energy E_g .

The absorption coefficient $\alpha(\lambda, T)$ as a function of wavelength and temperature is crucial for the upcoming photodiode model. It defines where the bulk of charge carriers is going to be generated. The shorter the distance the charge carriers have to travel the faster the device will respond to a change in irradiation.

Assuming a light wave traveling along the x direction and omitting the vector notation the photon flux $\Phi(x)$ at a certain position x from the surface exponentially decreases by equation 2.24

$$\Phi(x) = \Phi_0 \cdot e^{-\alpha \cdot x} \tag{2.24}$$

where Φ_0 is the photon flux impinging on the surface.

Assuming each photon creates an electron-hole pair the generation rate equals the decay of photons over distance. Using equation 2.24 one can calculate the generation rate by

$$G = -\nabla \circ \vec{\Phi} = \Phi_0 \cdot \alpha \cdot e^{-\alpha \cdot x} \tag{2.25}$$

2.1.2 Loss Mechanism

Recombination processes try to reestablish the thermal-equilibrium condition of the semiconductor. In an intrinsic direct-band semiconductor an electron-hole pair recombines by a band-to-band transition as presented in figure 2.2.

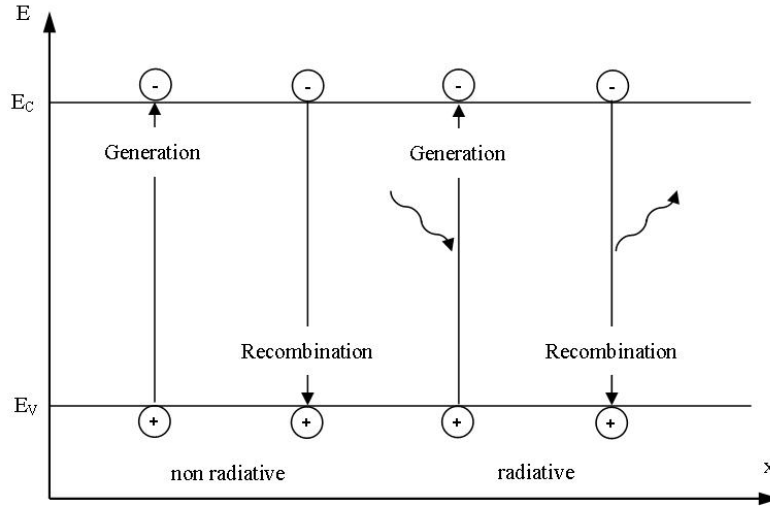


Figure 2.2: Band-to-band generation and recombination of an electron-hole pair in an intrinsic direct-band semiconductor as per [10]. E_C and E_V are the conduction and valence band edge, respectively.

Transitions are categorized into radiative and non-radiative according to photon contribution.

In an extrinsic semiconductor dopants create energy levels in the forbidden band. This energy levels can be utilized by generation and recombination processes as shown in figure 2.3. The transition probability of charge carriers increases with decreasing energy difference. Therefore defects lead to stronger recombination and limit the lifetime of charge carriers [10].

The numbers given in figure 2.3 indicate the different processes of recombination. Process 1 is generation and recombination in donor levels near the conduction band edge. In acceptor levels near the valence band edge this is called Process 2. Process 3 requires two different types of dopants and is a charge transfer from one level to another one. At room temperature all dopants are ionized, i.e. a captured charge carrier is immediately released. However, the charge carriers may be trapped at the impurity level if the energy difference exceeds the thermal energy. Traps near the middle of the band edge can capture charge carriers from the conduction band and emit them into the valence band as pictured by process 4. This has a strong impact on the charge carrier lifetime. The minority-carrier lifetime τ equates to

$$\tau = \frac{1}{\sigma \cdot \mathbf{v}_{th} \cdot N_t} \quad (2.26)$$

where σ is the capture cross section, \mathbf{v}_{th} the thermal velocity and N_t the trap density [9].

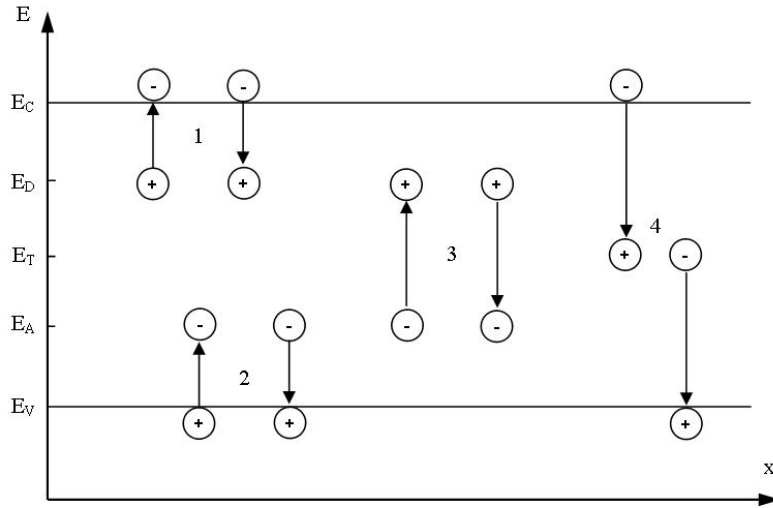


Figure 2.3: Generation and recombination in an extrinsic direct-band semiconductor as per [10]. E_C and E_V are the conduction and valence band edge, respectively. E_D is the donor level, E_A the acceptor level. E_T is the trap energy level.

As the minority-carrier lifetime is proportional to $1/N_t$ the carriers recombine at a faster rate in damaged regions like near a surface.

Leakage is another loss of charge carriers in integrated photodiodes. In contrast to recombination the charge carriers get separated but travel to other contacts or sinks than intended. A possible path for the leakage current is presented in figure 2.4.

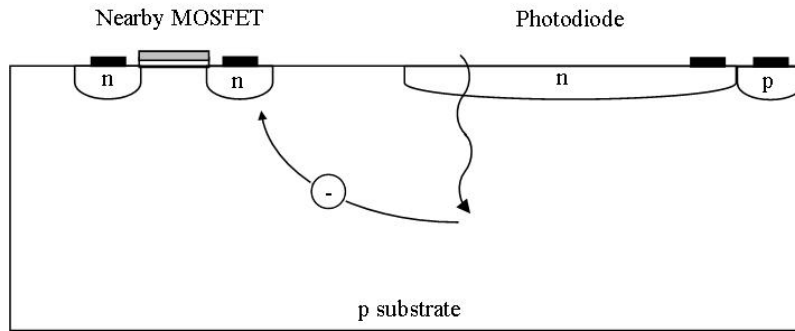


Figure 2.4: Leakage current in an exemplary structure. The minority electron does not contribute to the photocurrent as it diffuses to a nearby MOSFET.

Recombination is an effect inside the device while leakage is caused by the device surroundings and strongly influenced by the chip layout. Thus leakage cannot be properly modeled in a photodiode model used in a schematic design environment. The distance to neighboring structures is defined in the layout process. Hence leakage can be accommodated by layout design rules to decrease its impact.

2.1.3 Reflection in Multi-layered Material

Previous to the discussion of multi-layered material it is necessary to examine the reflection on a single surface.

The portion of the reflected light on the surface is defined as the reflectance or reflection coefficient R . It depends on the permittivities ϵ_1 and ϵ_2 of the involved media and therefore on the wavelength of the impinging light. At an incident angle other than perpendicular the reflection coefficient may differ for s- and p-polarized light. The s stands for senkrecht and p for parallel. The Fresnel equations for a lossless media¹ are used to determine the reflection coefficient [8].

$$R_p = \frac{\mathbf{E}_{rp}}{\mathbf{E}_{ip}} = \frac{\sqrt{\epsilon_2} \cdot \cos(\Theta_1) - \sqrt{\epsilon_1} \cdot \cos(\Theta_2)}{\sqrt{\epsilon_2} \cdot \cos(\Theta_1) + \sqrt{\epsilon_1} \cdot \cos(\Theta_2)} \quad (2.27a)$$

$$R_s = \frac{\mathbf{E}_{rs}}{\mathbf{E}_{is}} = \frac{\sqrt{\epsilon_2} \cdot \cos(\Theta_2) - \sqrt{\epsilon_1} \cdot \cos(\Theta_1)}{\sqrt{\epsilon_1} \cdot \cos(\Theta_1) + \sqrt{\epsilon_2} \cdot \cos(\Theta_2)} \quad (2.27b)$$

Where Θ_1 is the angle of incident and Θ_2 the angle of refraction. The indices p and s represent the polarization. Incident and reflected light are denoted by i and r , respectively. Complementary to the reflectance the transmittance or transmission coefficient T gives the portion of light traveling through the surface. In a lossless media the energy of the reflected and the transmitted wave must be identical to the incident energy. Therefore the reflectance plus the transmittance must equal unity.

$$R + T = 1 \quad (2.28)$$

If the surface is coated by another material with a dielectric constant ϵ_C the light wave is reflected multiple times between interface 1 and 2. This leads to a more complicated calculation of the total reflectance and transmittance, respectively. A coated surface shown in figure 2.5 with interface 1 and 2 is considered. The arrangement will be illuminated from the left hand side and the absorbing media is located at the right hand side. The total optical wave in the different regions is decomposed into waves going to left and right hand side, respectively.

The reflectance is calculated as a relation between the fields at interface 1 and 2. The electric field at interface 2 is assumed to be given and the electric field on boundary 1 is the object of research.

During the further investigation the vector arrows will be omitted.

Assuming perpendicular illumination the electric and magnetic field are tangential to the boundaries. The tangential electric field on a surface is continuous. As the current density on the boundary is zero the magnetic field is also continuous. The tangential fields on interface 1 are

$$\begin{aligned} \mathbf{E}_{in} &= \mathbf{E}_I + \mathbf{E}_{R1} = \mathbf{E}_{T1} + \mathbf{E}_{R2} \\ \mathbf{H}_{in} &= \mathbf{H}_I - \mathbf{H}_{R1} = \mathbf{H}_{T1} - \mathbf{H}_{R2} \end{aligned}$$

¹A lossless media has a negligible extinction coefficient K .

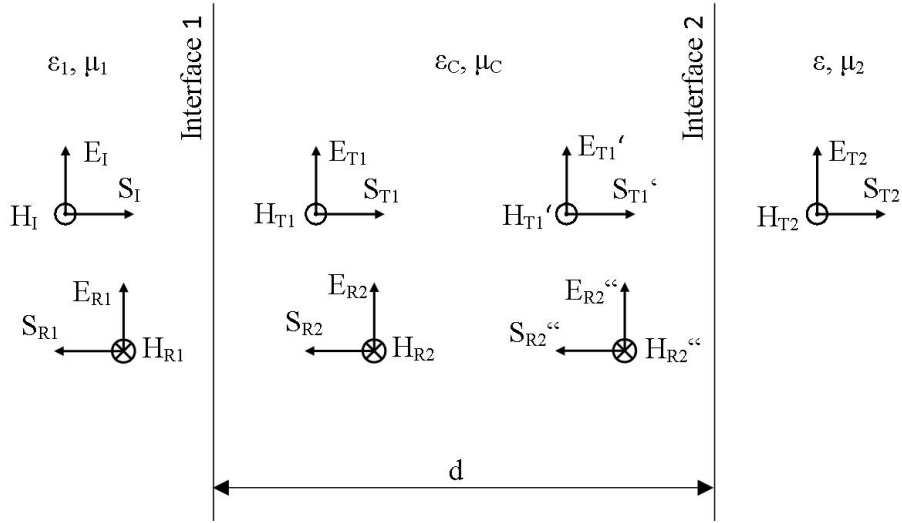


Figure 2.5: An optical wave impinging on a coated surface. A magnetic field vector pointing into the image plane is marked by a cross. A central dot indicates that the magnetic field vector points out of the plane.

The magnetic and the electric field are related to each other by the wave admittance Y .

$$Y = \frac{\mathbf{H}}{\mathbf{E}} \quad (2.29)$$

Furthermore with equation 2.18 the wave admittance can be written as

$$Y = \sqrt{\frac{\epsilon}{\mu_m}} = \sqrt{\frac{\epsilon_0 \cdot \epsilon_r}{\mu_0 \cdot \mu_r}} \quad (2.30)$$

For most materials used in optical applications μ_r is 1 and the relative permittivity ϵ_r determines the wave admittance.

One can substitute the magnetic field

$$\begin{aligned} \mathbf{E}_{in} &= \mathbf{E}_{T1} + \mathbf{E}_{R2} \\ \mathbf{H}_{in} &= Y_C \cdot \mathbf{E}_{T1} - Y_C \cdot \mathbf{E}_{R2} \end{aligned}$$

Using a matrix notation gives

$$\begin{pmatrix} \mathbf{E}_{in} \\ \mathbf{H}_{in} \end{pmatrix} = \begin{bmatrix} 1 & 1 \\ Y_C & -Y_C \end{bmatrix} \cdot \begin{pmatrix} \mathbf{E}_{T1} \\ \mathbf{E}_{R2} \end{pmatrix} \quad (2.31)$$

As the light travels between boundary 1 and 2 there is a phase difference δ .

$$\delta = \frac{2 \cdot \pi \cdot n_C}{\lambda} \cdot d \quad (2.32)$$

For light traveling to the right hand side is denoted with a single dash and its phase difference is negative. Light traveling to the left hand side is marked with a double dash and has a positive phase shift. Again the magnetic field is expressed as the admittance times the electric field.

$$\begin{aligned}\mathbf{E}'_{T1} &= \mathbf{E}_{T1} \cdot e^{-j\cdot\delta} \\ \mathbf{H}'_{T1} &= Y_C \cdot \mathbf{E}_{T1} \cdot e^{-j\cdot\delta}\end{aligned}$$

$$\begin{aligned}\mathbf{E}''_{R2} &= \mathbf{E}_{R2} \cdot e^{+j\cdot\delta} \\ \mathbf{H}''_{R2} &= Y_C \cdot \mathbf{E}_{R2} \cdot e^{+j\cdot\delta}\end{aligned}$$

No reflected wave arrives from the right hand side since all light is assumed to be absorbed inside the rightmost region. The electric and magnetic fields at boundary 2 are

$$\begin{aligned}\mathbf{E}_2 &= \mathbf{E}'_{T1} + \mathbf{E}''_{R2} = \mathbf{E}_{T2} \\ \mathbf{H}_2 &= \mathbf{H}'_{T1} - \mathbf{H}''_{R2} = \mathbf{H}_{T2}\end{aligned}$$

Using the expressions for \mathbf{E}'_{T1} , \mathbf{H}'_{T1} , \mathbf{E}''_{R2} and \mathbf{H}''_{R2} results in

$$\begin{aligned}\mathbf{E}_2 &= \mathbf{E}_{T1} \cdot e^{-j\cdot\delta} + \mathbf{E}_{R2} \cdot e^{+j\cdot\delta} \\ \mathbf{H}_2 &= Y_C \cdot \mathbf{E}_{T1} \cdot e^{-j\cdot\delta} - Y_C \cdot \mathbf{E}_{R2} \cdot e^{+j\cdot\delta}\end{aligned}$$

and in matrix notation

$$\begin{pmatrix} \mathbf{E}_2 \\ \mathbf{H}_2 \end{pmatrix} = \begin{bmatrix} e^{-j\cdot\delta} & e^{+j\cdot\delta} \\ Y_C \cdot e^{-j\cdot\delta} & -Y_C \cdot e^{+j\cdot\delta} \end{bmatrix} \cdot \begin{pmatrix} \mathbf{E}_{T1} \\ \mathbf{E}_{R2} \end{pmatrix} \quad (2.33)$$

Solving for \mathbf{E}_{T1} and \mathbf{E}_{R2} gives

$$\begin{pmatrix} \mathbf{E}_{T1} \\ \mathbf{E}_{R2} \end{pmatrix} = \begin{bmatrix} e^{-j\cdot\delta} & e^{+j\cdot\delta} \\ Y_C \cdot e^{-j\cdot\delta} & -Y_C \cdot e^{+j\cdot\delta} \end{bmatrix}^{-1} \cdot \begin{pmatrix} \mathbf{E}_2 \\ \mathbf{H}_2 \end{pmatrix} \quad (2.34)$$

The inverse of a 2×2 matrix is computed as the adjoint over the determinant.

$$\begin{bmatrix} a & b \\ c & d \end{bmatrix}^{-1} = \frac{1}{a \cdot d - b \cdot c} \cdot \begin{bmatrix} d & -b \\ -c & a \end{bmatrix} \quad (2.35)$$

Combining equations 2.34 and 2.35 results in

$$\begin{pmatrix} \mathbf{E}_{T1} \\ \mathbf{E}_{R2} \end{pmatrix} = \frac{1}{2} \cdot \begin{bmatrix} e^{+j\cdot\delta} & \frac{1}{Y_C} \cdot e^{+j\cdot\delta} \\ e^{-j\cdot\delta} & -\frac{1}{Y_C} \cdot e^{-j\cdot\delta} \end{bmatrix} \cdot \begin{pmatrix} \mathbf{E}_2 \\ \mathbf{H}_2 \end{pmatrix} \quad (2.36)$$

The equation above can be used in equation 2.31

$$\begin{aligned} \begin{pmatrix} \mathbf{E}_{in} \\ \mathbf{H}_{in} \end{pmatrix} &= \frac{1}{2} \cdot \begin{bmatrix} 1 & 1 \\ Y_C & -Y_C \end{bmatrix} \cdot \begin{bmatrix} e^{+j\cdot\delta} & \frac{1}{Y_C} \cdot e^{+j\cdot\delta} \\ e^{-j\cdot\delta} & -\frac{1}{Y_C} \cdot e^{-j\cdot\delta} \end{bmatrix} \cdot \begin{pmatrix} \mathbf{E}_2 \\ \mathbf{H}_2 \end{pmatrix} \\ \begin{pmatrix} \mathbf{E}_{in} \\ \mathbf{H}_{in} \end{pmatrix} &= \frac{1}{2} \cdot \begin{bmatrix} e^{+j\cdot\delta} + e^{-j\cdot\delta} & \frac{1}{Y_C} \cdot e^{+j\cdot\delta} - \frac{1}{Y_C} \cdot e^{-j\cdot\delta} \\ Y_C \cdot e^{+j\cdot\delta} - Y_C \cdot e^{-j\cdot\delta} & e^{+j\cdot\delta} + e^{-j\cdot\delta} \end{bmatrix} \cdot \begin{pmatrix} \mathbf{E}_2 \\ \mathbf{H}_2 \end{pmatrix} \end{aligned} \quad (2.37)$$

With the trigonometric identities

$$\begin{aligned} \sin(x) &= \frac{1}{2 \cdot j} \cdot (e^{j \cdot x} - e^{-j \cdot x}) \\ \cos(x) &= \frac{1}{2} \cdot (e^{j \cdot x} + e^{-j \cdot x}) \end{aligned}$$

and the wave admittance equation 2.37 becomes

$$\begin{pmatrix} \mathbf{E}_{in} \\ Y_{in} \cdot \mathbf{E}_{in} \end{pmatrix} = \begin{bmatrix} \cos(\delta) & \frac{j}{Y_C} \cdot \sin(\delta) \\ j \cdot Y_C \cdot \sin(\delta) & \cos(\delta) \end{bmatrix} \cdot \begin{pmatrix} \mathbf{E}_2 \\ Y_2 \cdot \mathbf{E}_2 \end{pmatrix} \quad (2.38)$$

Note the determinant of the matrix is identically unity as the media are assumed to be lossless.

For a multi-layered structure one starts at the layer next to the bulk assuming $\mathbf{E}_2 = 1$. For this layer the output vector is calculated and forms the input vector of the next layer. This progress is repeated until the input vector of the top most layer is determined.

For perpendicular illumination the Fresnel equation for parallel polarization in equation 2.27a must be used. The dielectric constant in the Fresnel equation can be substituted with equation 2.30. Setting $\sqrt{\epsilon_{r1}} = 1$ for air the reflectance R is than given as

$$R = \left| \frac{Y_{in} - 1}{Y_{in} + 1} \right| \quad (2.39)$$

As an example the transmittance T is calculated with the refractive indices listed in table 2.1. The results for two assumed structures is presented in figure 2.6. For the calculation of this example the refractive indices are assumed to be constant. But as discussed at the beginning of section 2.1 the refractive index changes with wavelength. The model considers this dependency and calculates the the transmittance accordingly.

Table 2.1: Refractive indices for calculating the transmittance [9]. The silicon refractive index marked with* is obtained by equation 2.14 as the square root of ϵ_r .

n_{Si}	3.45*
n_{SiO_2}	1.46
$n_{Si_3N_4}$	2.05

The model up to now offers no possibility to change the angle of incident to anything than perpendicular. Therefore also polarization has no influence on the transmission of

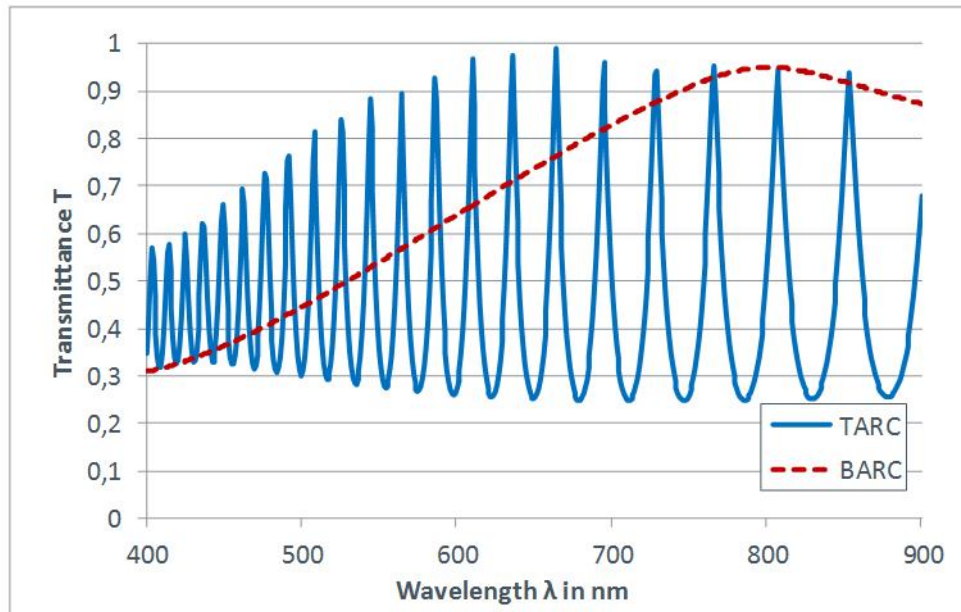


Figure 2.6: Transmittance of a TARC and a BARC on silicon. The TARC consists of 100 nm Si_3N_4 on $5\ \mu\text{m}$ SiO_2 . The BARC is a 100 nm thick Si_3N_4 layer.

the ARC. However, as the angle of incident changes the transmission characteristic of the ARC, worst case parameter sets can be used to cover non-perpendicular illumination to some extent.

2.2 Photodiodes

After getting through the basics in section 2.1 the working principle and structures of photodiodes can be studied. Simple photodiode settings like the p-n and the p-i-n will be discussed. Furthermore this section details the collection of charge carriers as well as the meaning of avalanche effect in a photodiode.

In order to compare different types of photodiodes quantitatively numerous figures have been developed. They measure the performance of a photodiode in different aspects like response speed or leakage current. A discussion of these quantities concludes this section.

2.2.1 Working Principle

Electrons and holes generated due to photoexcitation must be collected and transported to the device contacts. One method is using an electric field to separate the charge carriers and avoid recombination in the device. This electric field can be a build-in electric field like in a diode or can be applied externally as used in a photoconductor. Figure 2.7 shows a simplified image of a p-n-photodiode and the photoexcitation of an electron-hole pair. The charge carriers drift towards the contact until they arrive at the boundaries of the depletion layer. In the quasi-neutral p and n region the carriers diffuse to the contacts. Thus the photodiode can be divided into two different regions according to the movement mechanism of charge carriers

- Diffusion in quasi-neutral regions
- Drift in depletion layer

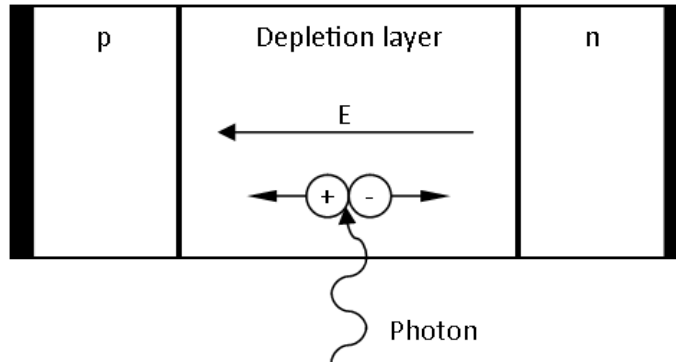


Figure 2.7: Charge carrier separation in a p-n-photodiode.

A quantitative analysis requires the solution of the continuity equation in each of the aforementioned regions for electrons and holes.

$$\frac{\partial n}{\partial t} = G_n - U_n + \frac{1}{q} \cdot \nabla \circ \vec{\mathbf{J}} \quad (2.40a)$$

$$\frac{\partial p}{\partial t} = G_p - U_p - \frac{1}{q} \cdot \nabla \circ \vec{\mathbf{J}} \quad (2.40b)$$

The temporal change of the charge carrier numbers p and n at a certain position is caused by the following reasons:

- Generation G
- Recombination U
- Spatial change in current flow $\frac{1}{q} \cdot \nabla \circ \vec{\mathbf{J}}$

The number of electrons and holes generated by photoexcitation is equal, because an electron-hole *pair* is created. Therefore both quantities G_n and G_p are given by equation 2.25. The recombination rate is the excess charge carrier density over the life time.

$$U_n = \frac{n - n_0}{\tau_n} \quad (2.41a)$$

$$U_p = \frac{p - p_0}{\tau_p} \quad (2.41b)$$

The last component of the continuity equation has different signs for electrons and holes, as a positive current means a positive flux of holes and a negative flux of electrons. In order to exemplify this figure 2.8 shows the change of charge carrier density as a reason for a non-zero divergence of current density.

This current flow is further composed of a drift and a diffusion current.

$$\vec{\mathbf{J}}_n = +q \cdot D_n \cdot \nabla n_p + q \cdot \mu_n \cdot n_p \cdot \vec{\mathbf{E}} \quad (2.42a)$$

$$\vec{\mathbf{J}}_p = -q \cdot D_p \cdot \nabla p_n + q \cdot \mu_p \cdot p_n \cdot \vec{\mathbf{E}} \quad (2.42b)$$

Thus one can write the continuity equation for electrons and holes in one dimension x assuming a constant mobility and electric field along the region of interest.

$$\frac{\partial n}{\partial t} = D_n \cdot \frac{\partial^2 n_p}{\partial x^2} + \mu_n \cdot \mathbf{E} \cdot \frac{\partial n_p}{\partial x} - \frac{n_p - n_{p0}}{\tau_n} + G(x) \quad (2.43a)$$

$$\frac{\partial p}{\partial t} = D_p \cdot \frac{\partial^2 p_n}{\partial x^2} - \mu_p \cdot \mathbf{E} \cdot \frac{\partial p_n}{\partial x} - \frac{p_n - p_{n0}}{\tau_p} + G(x) \quad (2.43b)$$

D_p and D_n are the diffusion constants, p_n and n_p are the minority carrier concentrations, p_{n0} and n_{p0} are the equilibrium minority carrier concentrations, μ_n and μ_p are the carrier mobilities, τ_n and τ_p are the lifetimes, \mathbf{E} is the electric field and $G(x)$ is the generation rate due to photoexcitation.

In order to solve these differential equations different assumptions are necessary to obtain a solution suitable for a circuit simulator. These assumptions and the derivation of the model are covered in section 3.1.

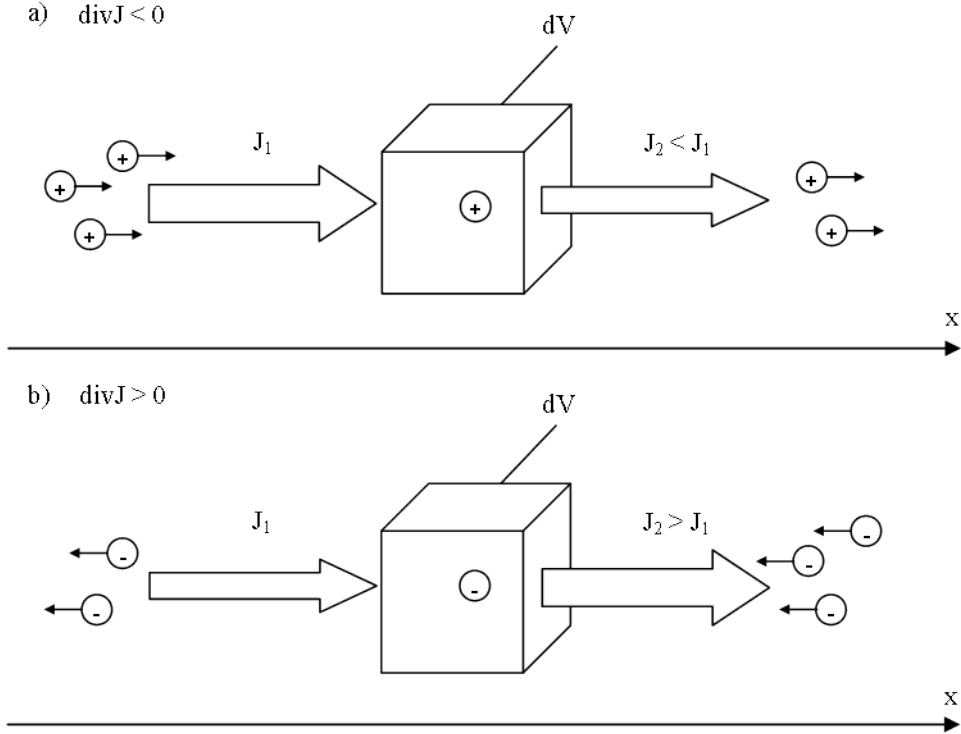


Figure 2.8: Divergence of current density causes a local change of charge carrier concentration in an infinitesimal small volume $d\mathbf{V}$.

- a) Increasing hole concentration p with $\nabla \circ \vec{\mathbf{J}} < 0$.
- b) Increasing electron concentration n with $\nabla \circ \vec{\mathbf{J}} > 0$.

2.2.2 Characteristics of Photodiodes

Numerous characteristic figures have been developed in order to compare different photodiodes. They give information of a photodiode's performance regarding specific aspects. These figures describe the performance during illumination and in dark situations as well. This allows for a standardized specification at the market and in literature. The characteristics used in this thesis are explained next.

Dark Current

Even if the photodiode is not illuminated a small current flows in a reverse biased condition. This is the very same leakage current as in any diode and is called dark current. In a photodiode it is of particular interest since it limits the sensitivity, i.e. the minimum detectable amount of light. As photodiodes are large area devices their leakage current is also important when it comes to power consumption in mobile devices. The dark current is determined by the Shockley equation [9].

$$I = J_s \cdot \left(e^{\frac{q \cdot V}{m \cdot k_B \cdot T}} - 1 \right) \cdot A \tag{2.44}$$

where I_s is the saturation current, V the forward bias voltage, m the quality factor and A is the device area. The saturation current density is determined by [9]

$$J_s = q \cdot \frac{D_p}{L_p} \cdot p_{n0} + q \cdot \frac{D_n}{L_n} \cdot n_{p0}$$

$$J_s = q \cdot n_i^2 \cdot \left(\frac{D_p}{L_p \cdot N_D} + \frac{D_n}{L_n \cdot N_A} \right)$$

where n and p are the carrier concentrations of electrons and holes, respectively. The index letter gives the region where the quantity is used, e.g. p_n is the hole density in the n region. The index 0 means the quantity at equilibrium. D is the diffusion constant and L the diffusion length. Both are indexed accordingly for electrons and holes. N_A and N_D are the doping concentrations for acceptors and donors, respectively.

The saturation current is determined by the doping concentrations and the minority charge carrier concentrations. A low leakage current device is heavily doped. Furthermore the saturation current is temperature dependent due to its relation to the minority charge carrier concentrations. This effect is usually more pronounced than the temperature dependency given in equation 2.44. The reverse current of a diode increases in exponential manner with higher temperatures.

Capacitance

The depletion layer forms a capacitance. Since the boundaries of the depletion layer depend on bias the capacitance is voltage dependent. In order to determine the capacitance per unit area one must calculate the derivative of the stored charge at the junction Q_c with respect to the applied voltage in reverse direction V_r . According to Sze the capacitance for a one-sided abrupt junction equals [9]

$$C = \frac{dQ_c}{dV} = \sqrt{\frac{q \cdot \epsilon \cdot N_B}{2 \cdot (V_{bi} + V_r - 2 \cdot k_B \cdot T/q)}} \quad (2.45)$$

where V_{bi} is the build-in voltage and N_B the lower doping concentration given as

$$N_B = \frac{N_A \cdot N_D}{N_A + N_D} \approx \begin{cases} N_D & \text{if } N_A \gg N_D \\ N_A & \text{if } N_D \gg N_A \end{cases}$$

For a linear graded junction with a impurity gradient a the capacitance is given as [9]

$$C = \frac{dQ_c}{dV} = \sqrt[3]{\frac{q \cdot a \cdot \epsilon^2}{12 \cdot (V_{bi} + V_r)}} \quad (2.46)$$

The dependence of the capacitance on the bias voltage is obvious from equation 2.45 and 2.46. The capacitance is crucial for the response speed of the device as this capacitance has to be charged. Applying a reverse bias to a photodiode decreases its capacitance and

therefore speeds up the device.

Besides the depletion capacitance there is the diffusion capacitance. However, this gets important in forward direction only. As a photodiode is typically reverse biased a discussion of the diffusion capacitance is omitted.

Quantum Efficiency

The fraction of the number of collected charge carriers n_c to the number of impinging photon n_{ph} is defined as the quantum efficiency QE .

$$QE = \frac{n_c}{n_{ph}} \quad (2.47)$$

The number of charge carriers can be expressed as the integral of current in respect to time over elementary charge.

$$n_c = \frac{1}{q} \cdot \int_{t_1}^{t_2} I dt \quad (2.48)$$

For a DC current the upper equation can be reduced to

$$n_c = \frac{I \cdot t}{q}$$

The number of impinging photons is the photonic flux $\vec{\Phi}$ integrated over the illuminated area A and time. For a homogenous and time-independent photonic flux the integrals simplifies to

$$n_{ph} = \Phi \cdot A \cdot t$$

Substitution of the number of charge carriers and photons in equation 2.47 yields

$$QE = \frac{I \cdot t/q}{\Phi \cdot A \cdot t} = \frac{I}{q \cdot \Phi \cdot A}$$

Normalize I to the illuminated diode area A assuming a homogenous current flow gives the current density J .

$$QE = \frac{J}{q \cdot \Phi} \quad (2.49)$$

An ideal, non-avalanche photodiode² has a maximum quantum efficiency of 1, for the case that each electron-hole pair of a photon is collected. Note that the quantum efficiency can exceed unity in avalanche photodiodes due to carrier multiplication.

Depending on the position where the photon flux Φ is measured one distinguishes between external and internal quantum efficiency. External quantum efficiency takes all photon impinging on the device into account. Since some photon get reflected or absorbed in the ARC or ILD not all impinging photons reach the silicon surface. Internal quantum efficiency considers the amount of photons reaching the silicon surface only.

²See section 2.2.3 for avalanche and non-avalanche photodiode.

Responsivity

The responsivity \mathfrak{R} relates the output current to the beam power³.

$$\mathfrak{R} = \frac{I}{P_{Beam}} \quad (2.50)$$

This quantity is used more frequently than the quantum efficiency and they are related to each other. Combining equations 2.2, 2.3, 2.49 and 2.50 yields

$$\mathfrak{R} = \frac{q}{h \cdot c} \cdot \lambda \cdot QE$$

The responsivity is proportional to the quantum efficiency times the wavelength. As mentioned for non-avalanche devices the maximum quantum efficiency is limited to unity. Thus there is a maximum responsivity given by

$$\mathfrak{R}_{max} = \frac{q}{h \cdot c} \cdot \lambda$$

Usually the responsivity is given as a plot over wavelength λ . Therefore the photocurrent and the beam power are measured for each wavelength and the responsivity calculated per equation 2.50. A exemplary responsivity curve is printed in figure 2.9.

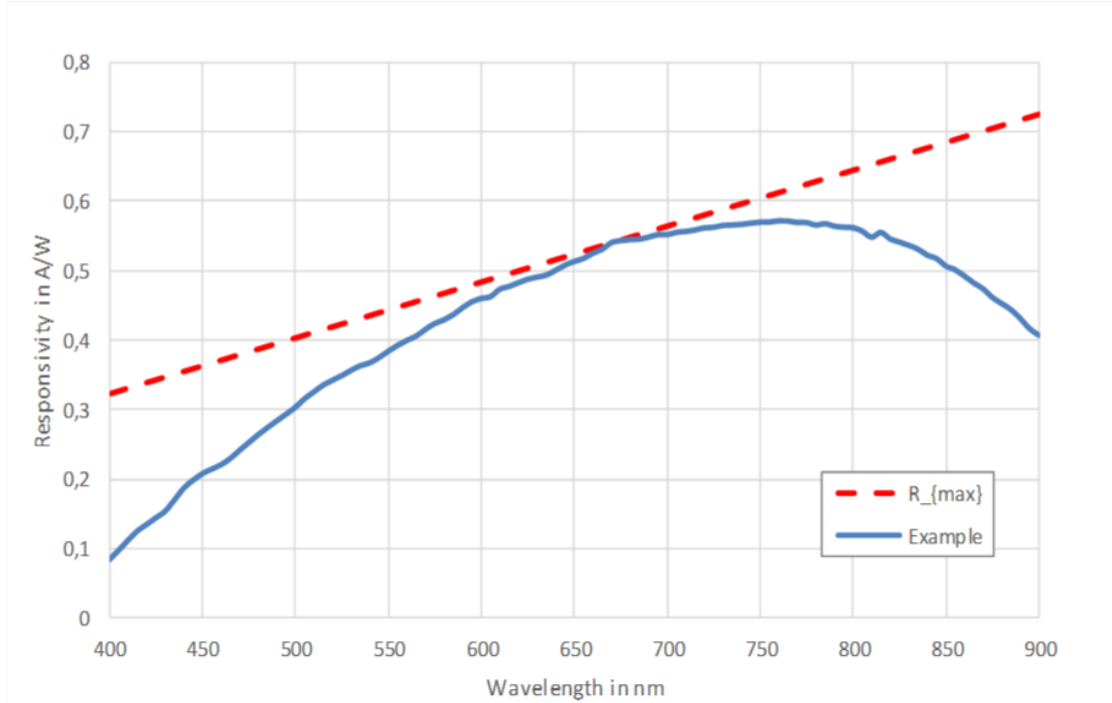


Figure 2.9: Exemplary responsivity plot. The solid line is the responsivity. The dashed line is the responsivity for a quantum efficiency $QE = 1$.

³In theory the beam power is not well defined. In the laboratory the beam power is easily measurable.

Frequency Response

So far all figures were valid for static operation. Dynamic properties are covered by the frequency response or Bode plot $H(f)$ and $H(\omega)$, respectively. It pictures the output current over the frequency of the impinging light signal. It is important to distinguish between the frequency of the signal f and the frequency of the light wave f_w . A small example will examine the difference.

A light source with a wavelength $\lambda = 600 \text{ nm}$ is turned on and off every second. This gives a signal frequency of $f = 1/T = 1 \text{ Hz}$ while the frequency of the light wave is $f_w = c/\lambda = 500 \text{ THz}$. Further on, the term frequency means the signal frequency while the wave frequency is referenced by the wavelength.

The frequency response is usually defined as the relation between input and output quantity. For low frequencies this relation is the responsivity. To avoid redundancy in the information the frequency response will be the set as the relation between the AC and the DC output values.

The response speed of a photodiode is primarily defined by the carrier movement through the device. The charge carriers must travel from the place of generation through the depletion layer and the quasi-neutral regions to the contacts. The response features a fast and a slow component. The fast component stems from the charge carriers in the depletion region. The slow component is caused by the charge carriers in the quasi-neutral region. There the charge carriers have to reach their equilibrium value. This means they either have to recombine or diffuse to the depletion layer. The latter are the cause of the slow component.

2.2.3 Structures of Photodiodes

Photodiodes usually consist of a photo-active volume where photoexcitation takes place and a protective surface layer. The latter often also serves as an anti-reflective coating (ARC) to either enhance or block the transmission of a certain wavelength.

First the photo-active area will be covered. The two basic types of photodiodes are the p-n and the p-i-n photodiode. The single letters indicate the doping profile of the device. A p-n photodiode consists of a p and an n doped region like a normal diode. A p-i-n photodiode comes with an intrinsic or lowly doped layer in between the p and n region. In both a single photon creates one electron-hole pair only, limiting its quantum efficiency to unity. The two structures are printed in figure 2.10.

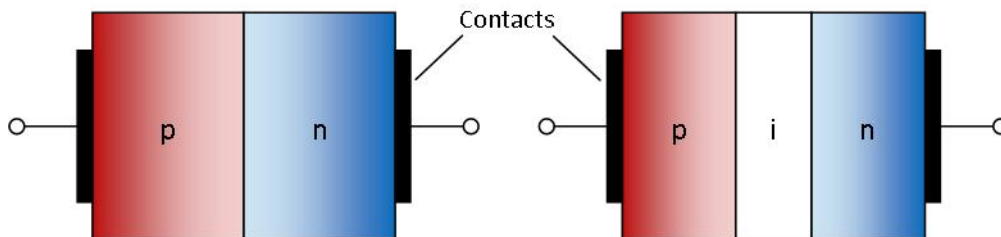


Figure 2.10: Structure of photodiodes. Left: p-n-photodiode, Right: p-i-n-photodiode

A special type worth to mention is the avalanche photodiode (APD) which multiplies the charge carriers created within by impact ionization. Thus a single photon results in several charge carriers in an APD and its quantum efficiency can reach values between 10^2 and 10^4 [9]. As the model is for non-avalanche devices a detailed discussion of the APD will be omitted.

The transmission filter on top the photodiode can be build in different ways. Simple color filters and complex multi-layered interference filters are two possible realizations. In either way their purpose is to tune the response of the photodiode to a certain wavelength.

p-n-Photodiode

A p-n-photodiode is the most simple photodiode. It is formed by a diode as used in non-optoelectronic applications. Its junction may be set to a certain distance from the surface to adjust the device response to light exposure. Since the absorption coefficient α depends on the wavelength as detailed in section 2.1.1 the position of the junction has a crucial impact on the response of the photodiode. A p-n-photodiode designed to detect long wavelength light will come with a big junction depth. To detect shorter wavelength more efficiently the junction is placed close to the surface.

p-i-n-Photodiode

The p-i-n-photodiode has an additional intrinsic or lowly doped layer between the p and the n region. This intrinsic layer spreads the electric field over a bigger distance and so increases the charge collecting volume. A p-i-n-photodiode can be tuned to utilize nearly all impinging photons, i.e. they are almost without loss. In addition its frequency response can be tuned as well although it is slightly slower than a p-n device [9]. As the intrinsic layer is grown by epitaxy the p-i-n-photodiode is more expensive and not available in every process.

Anti-Reflective Coating

An anti-reflective coating (ARC) minimizes the reflection of a certain wavelength in order to increase the photodiodes sensitivity. This ARC can be a single layer deposited on top the photodiode with a certain refractive index in simple cases. More complex transmission spectra can be obtained using interference filter. These are multi-layered structures of material with different refractive indexes.

The ARC is usually deposited on top of the inter-layer dielectrics (ILD) above the photodiode. This is called a top anti-reflective coating (TARC). If the ILDs are removed previously, i.e. the ARC is deposited directly on top the photodiode it is called bottom anti-reflective coating (BARC).

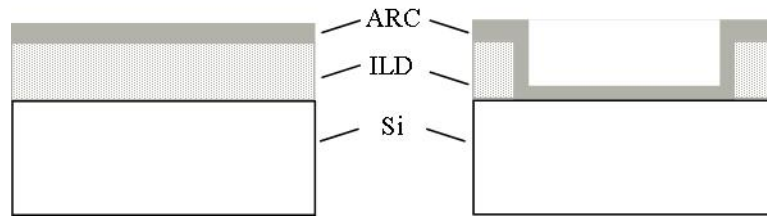


Figure 2.11: Different structures of anti-reflective coatings.
 Left: Top anti-reflective coating. Right: Bottom anti-reflective coating.

Top Anti-Reflective Coating

As the TARC is deposited on top of the ILD one has to calculate the reflectivity and transmission of a multi-layered material even if the TARC consists of a single layer. In addition there is usually very few information about the ILD properties like layer thickness, layer thickness variation and refractive index. However the TARC is much cheaper to produce than the BARC by a simple adjustment of the silicon nitride passivation layer thickness.

Bottom Anti-Reflective Coating

The BARC is positioned directly on top of the photodiode. Thus no additional layers have to be considered in a model. As an additional process step is required to remove the ILD above the photodiodes the BARC is more expensive to produce.

Chapter 3

Model Verification

The previous chapter contained the necessary knowledge to verify the photodiode model. Different photodiode structures and the continuity equation for charge carriers were presented. This chapter covers the principle assumptions of the model and investigates their validity.

The depletion layer is discussed first, since it is the easiest part to calculate and the most important one. Before solving the continuity equation for the quasi-neutral regions their general properties are derived as a common basis. Once the basic equations are given the calculations and assumptions of the particular regions are explained.

During the examination of the model different positions inside the device are referenced. These are pictured in figure 3.1. The model describes an n-well in an epitaxial layer deposited in a lightly p-doped epitaxial layer on a heavily p-doped substrate. The silicon surface is located at $x = 0$ m. The n-well extends to a depth of x_1 for the calculations. The depletion layer reaches from x_1 to x_2 . Below this comes the quasi-neutral region of lightly p-doped epitaxial layer which extends to x_L . Between the epitaxial layer and the substrate the doping concentration changes. This change occurs in a transition layer reaching from x_L to x_H . Due to the doping gradient in the transition layer, an electric field is created. The maximal electric field is located at x_3 . The substrate starts at x_H and extends to the rear side of the wafer. The penetration depth of light is below $100 \mu\text{m}$ for wavelength shorter than 900 nm as presented in figure 2.1. A substrate with a thickness of greater than $500 \mu\text{m}$ can therefore be assumed semi-infinite.

An exemplary doping profile of a photodiode is shown in figure 3.2. The doping profile is crucial for the behavior of the charge carriers traveling through the device. It influences diffusion and recombination, which are important for the photodiodes characteristics.

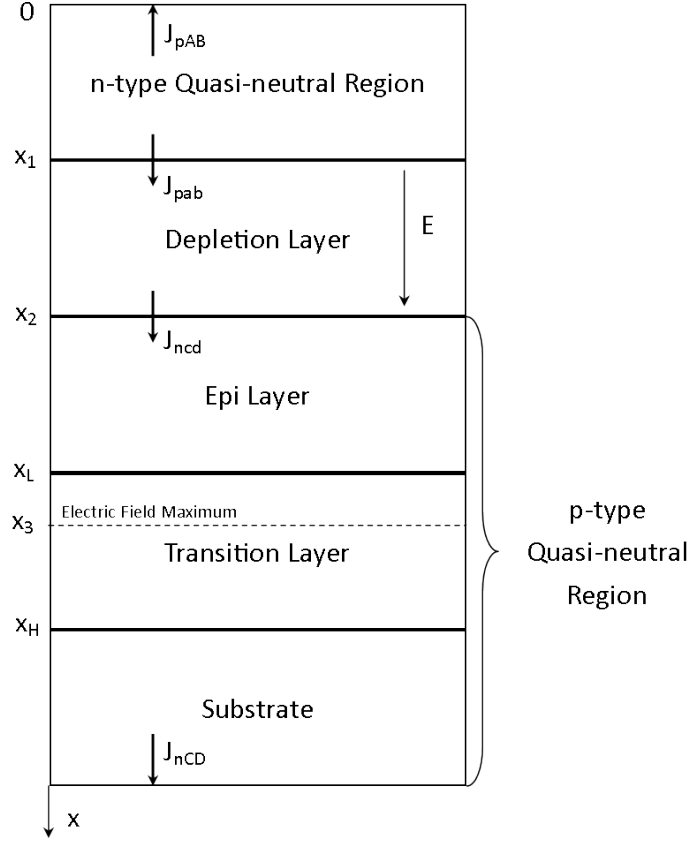


Figure 3.1: Geometry for the model verification.

3.1 Depletion Layer

The depletion layer is the most important layer in a photodiode. Its electric field separates the excess holes and electrons from each other. Thus carrier transport is dominated by drift current. The total photodiode current equals the one traveling through the depletion layer. This effect can be calculated by using the Laplace transform with respect to time. Electron and hole drift current densities travel in different directions with respect to the current flow direction. This causes a difference in time the charge carriers take to travel through the depletion layer. Hence the current densities for electrons and holes will be distinguished.

$$\mathbf{J}_{Depl}(x, t) = \mathbf{J}_p(x, t) + \mathbf{J}_n(x, t) \quad (3.1)$$

Integrating equation 3.1 over the width of the depletion layer gives

$$\begin{aligned} \int_{x_1}^{x_2} \mathbf{J}_{Depl}(x, t) dx &= \int_{x_1}^{x_2} \mathbf{J}_p(x, t) + \mathbf{J}_n(x, t) dx \\ \mathbf{J}_{Depl}(t) &= \frac{1}{d_{Depl}} \cdot \int_{x_1}^{x_2} \mathbf{J}_p(x, t) + \mathbf{J}_n(x, t) dx \end{aligned} \quad (3.2)$$

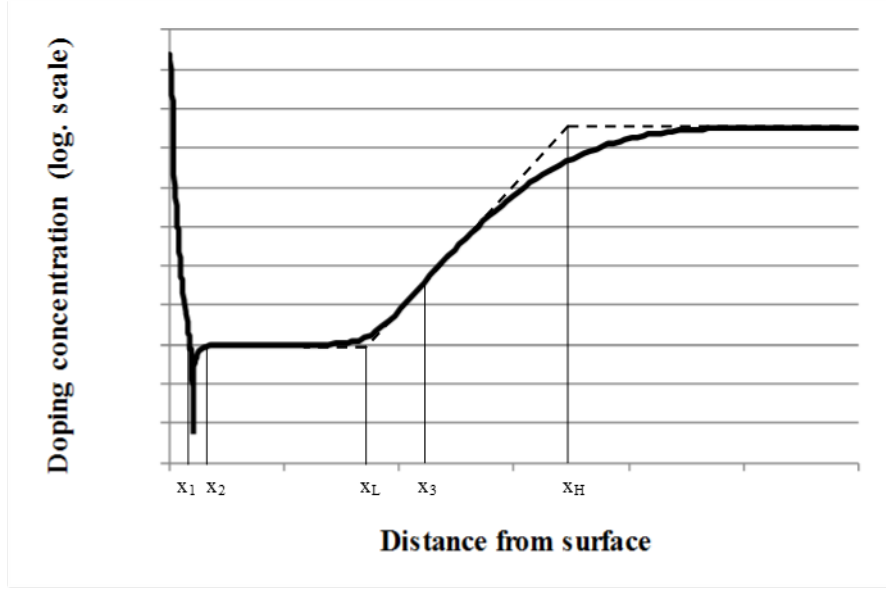


Figure 3.2: Exemplary doping profile of a photodiode.

where d_{Depl} is the depletion layer width defined as

$$d_{Depl} = x_2 - x_1$$

The carriers take a certain time to travel through the depletion layer. Applying the Laplace transform with respect to time on equation 3.2 results in

$$\bar{\mathbf{J}}_{Depl}(s) = \frac{1}{d_{Depl}} \cdot \int_{x_1}^{x_2} \bar{\mathbf{J}}_p(x, s) + \bar{\mathbf{J}}_n(x, s) dx \quad (3.3)$$

Furthermore the hole and electron current densities consist of two components. The first current density is generated in the quasi-neutral regions and the second one inside the depletion layer. The current densities arriving from the quasi-neutral regions are named \mathbf{J}_{pab} and \mathbf{J}_{ncd} , respectively, in accordance with figure 3.1. Note these current densities are constant along the depletion layer and do not depend on x . The current densities \mathbf{J}_{pO} and \mathbf{J}_{nO} are generated inside the depletion layer. Thus the individual current densities can be written as

$$\bar{\mathbf{J}}_n(x, s) = \bar{\mathbf{J}}_{ncd}(s) + \bar{\mathbf{J}}_{nO}(x, s) \quad (3.4a)$$

$$\bar{\mathbf{J}}_p(x, s) = \bar{\mathbf{J}}_{pab}(s) + \bar{\mathbf{J}}_{pO}(x, s) \quad (3.4b)$$

The current densities from the quasi-neutral regions are discussed prior to the one generated inside the depletion layer.

An electron current density travels from bottom to top starting at x_2 in the structure given in figure 3.1 and in the opposite direction of x . The time delay is therefore determined by

$$\bar{\mathbf{J}}_n(x, s) = \bar{\mathbf{J}}_{ncd} \cdot e^{-\frac{x_2-x}{v_n} \cdot s} \quad (3.5)$$

A hole current density travels in the direction of x starting at x_1 .

$$\bar{\mathbf{J}}_p(x, s) = \bar{\mathbf{J}}_{pab} \cdot e^{-\frac{x-x_1}{v_p} \cdot s} \quad (3.6)$$

\mathbf{v}_n and \mathbf{v}_p are the drift velocities for electrons and holes, respectively. These velocities are set equal to \mathbf{v} . This simplification is justified, as the dynamic behavior of a photodiode is determined by the quasi-neutral regions. Two different drift velocities for holes and electrons lead to an unnecessary complicated model of the depletion layer.

The current density through the depletion layer out of the quasi-neutral regions $\bar{\mathbf{J}}_{Depl1}(x, s)$ is obtained by equation 3.3. Substituting $\bar{\mathbf{J}}_n(x, s)$ by equation 3.5 and $\bar{\mathbf{J}}_p(x, s)$ by 3.6 gives

$$\begin{aligned} \bar{\mathbf{J}}_{Depl1}(s) &= \frac{1}{d_{Depl}} \cdot \int_{x_1}^{x_2} \bar{\mathbf{J}}_{pab} \cdot e^{-\frac{x-x_1}{v_p} \cdot s} + \bar{\mathbf{J}}_{ncd} \cdot e^{-\frac{x_2-x}{v_n} \cdot s} dx \\ \bar{\mathbf{J}}_{Depl1}(s) &= \frac{1 - e^{-\frac{d_{Depl}}{v} \cdot s}}{\frac{d_{Depl}}{v} \cdot s} \cdot (\bar{\mathbf{J}}_{pab} + \bar{\mathbf{J}}_{ncd}) \end{aligned}$$

The fraction of the depletion layer width d_{Depl} to the velocity \mathbf{v} is defined as the transit time t_r .

$$t_r = \frac{d_{Depl}}{\mathbf{v}} \quad (3.7)$$

The current density in the depletion layer caused by the quasi-neutral regions becomes

$$\bar{\mathbf{J}}_{Depl1}(s) = \frac{1 - e^{-s \cdot t_r}}{s \cdot t_r} \cdot (\bar{\mathbf{J}}_{pab} + \bar{\mathbf{J}}_{ncd}) \quad (3.8)$$

The current densities generated inside the depletion layer \mathbf{J}_{nO} and \mathbf{J}_{pO} are covered next. Again equal drift velocities for electrons and holes are assumed. The life time of the charge carriers is much larger than the mean transit time through the depletion layer. Hence recombination as well as diffusion is neglected. The current densities, equation 2.42a and 2.42b, can be written as

$$\mathbf{J}_{nO}(x, t) = q \cdot n \cdot \mathbf{v} \cdot \vec{e}_E \quad (3.9a)$$

$$\mathbf{J}_{pO}(x, t) = q \cdot p \cdot \mathbf{v} \cdot \vec{e}_E \quad (3.9b)$$

Solving for the carrier concentrations and substituting the results in equations 2.43a and 2.43b while neglecting diffusion and recombination gives

$$\frac{d\bar{\mathbf{J}}_{nO}}{dx} - \left(\frac{s}{v} + \frac{1}{L} \right) \bar{\mathbf{J}}_n - q \cdot \frac{d\bar{\Phi}}{dx} = 0 \quad (3.10a)$$

$$\frac{d\bar{\mathbf{J}}_{pO}}{dx} + \left(\frac{s}{v} + \frac{1}{L} \right) \bar{\mathbf{J}}_p + q \cdot \frac{d\bar{\Phi}}{dx} = 0 \quad (3.10b)$$

were the mean free path L equals

$$L = \mathbf{v} \cdot \tau \quad (3.11)$$

The solutions of the differential equations 3.10a and 3.10b are

$$\mathbf{J}_{nO}(x, s) = \int_{x_1}^x e^{-\left(\frac{s}{v} + \frac{1}{L}\right) \cdot (y-x)} \cdot q \cdot \frac{d\bar{\Phi}}{dy} dy \quad (3.12a)$$

$$\mathbf{J}_{pO}(x, s) = - \int_{x_1}^x e^{-\left(\frac{s}{v} + \frac{1}{L}\right) \cdot (x-y)} \cdot q \cdot \frac{d\bar{\Phi}}{dy} dy \quad (3.12b)$$

The two equations above are used in equation 3.3 and result in

$$\bar{\mathbf{J}}_{Depl2}(s) = -\frac{1}{d_{Depl}} \cdot \int_{x_1}^{x_2} \int_{x_1}^{x_2} e^{-\left(\frac{s}{v} + \frac{1}{L}\right) \cdot |x-y|} \cdot q \cdot \frac{d\bar{\Phi}}{dy} dy dx \quad (3.13)$$

The solution of the above integral is not trivial. Therefore some approximations are made to obtain manageable expressions for the circuit simulator.

The stationary solution is determined by the final value theorem of the Laplace transform.

$$\lim_{t \rightarrow \infty} f(t) = \lim_{s \rightarrow 0} (s \cdot \bar{F}(s))$$

Applying the final value theorem to equation 3.13 gives

$$\mathbf{J}_{Depl2}(t \rightarrow \infty) = -\frac{1}{d_{Depl}} \cdot \int_{x_1}^{x_2} \int_{x_1}^{x_2} e^{-\frac{|x-y|}{L}} \cdot q \cdot \frac{d\bar{\Phi}}{dy} dy dx \quad (3.14)$$

Furthermore the mean free path is usually large compared to the depletion layer width d_{Depl} . Thus the exponential is approximated by unity. The current density caused by the photogenerated charge carriers is obtained by performing the double integration in equation 3.15.

$$\mathbf{J}_{Depl2,DC} = \mathbf{J}_{Depl2}(t \rightarrow \infty) = q \cdot \bar{\Phi}(x_1) - q \cdot \bar{\Phi}(x_2) \quad (3.15)$$

The photogenerated current density equals the difference between the ideal photocurrent entering at x_1 and the one leaving at x_2 .

The dynamic behavior can be approximated by observing equation 3.13. The time delay of the individual charge carriers is

$$t(x, y) = \frac{|x - y|}{v} \quad (3.16)$$

This value is less or equal to the transit time t_r of the charge carriers coming from the quasi-neutral regions. However the transit time for all charge carriers traveling through the depletion layer is set to t_r . The inaccuracy caused by this simplification is considered negligible. The cut-off frequency of the depletion layer is usually much larger than the one of the quasi-neutral regions. Thus the total current of the depletion layer and photodiode equals

$$\bar{\mathbf{J}}_{Depl} = \frac{1 - e^{-s \cdot t_r}}{s \cdot t_r} \cdot q \cdot \bar{\Phi}_0 \cdot (e^{-\alpha \cdot x_1} - e^{-\alpha \cdot x_2}) + \frac{1 - e^{-s \cdot t_r}}{s \cdot t_r} \cdot (\bar{\mathbf{J}}_{pab} + \bar{\mathbf{J}}_{ncd}) \quad (3.17)$$

3.2 Quasi-neutral Regions

Starting with Einsteins relation

$$\frac{D}{\mu} = \frac{k_B \cdot T}{q} \quad (3.18)$$

with D the diffusion constant, μ the mobility, k_B the Boltzmann's constant and T the absolute temperature. Introducing the thermal voltage V_T

$$V_T = \frac{k_B \cdot T}{q} \quad (3.19)$$

one can rewrite the currents given in equation 2.42a and 2.42b

$$\vec{\mathbf{J}}_n = q \cdot D_n \cdot \left(\nabla n_p + n_p \cdot \frac{\vec{\mathbf{E}}}{V_T} \right) \quad (3.20a)$$

$$\vec{\mathbf{J}}_p = q \cdot D_p \cdot \left(-\nabla p_n + p_n \cdot \frac{\vec{\mathbf{E}}}{V_T} \right) \quad (3.20b)$$

The majority charge carriers can not travel across the depletion layer. The current density must become $J = 0 \text{ A/m}^2$. This results in a relation between the electric field and the charge carrier distribution.

$$\begin{aligned} \frac{\vec{\mathbf{E}}}{V_T} &= -\frac{\nabla n}{n} \\ \frac{\vec{\mathbf{E}}}{V_T} &= \frac{\nabla p}{p} \end{aligned}$$

The electron and hole densities consist of the equilibrium charge carriers n_0 and p_0 and the photogenerated excess electrons \hat{n} and holes \hat{p} , respectively. All donor and acceptor impurities are assumed to be ionized, i.e. $n_0 \approx N_D$ and $p_0 \approx N_A$. The number of generated charge carriers is assumed to be significantly less than the doping concentrations.

$$\begin{aligned} \frac{\vec{\mathbf{E}}}{V_T} &\cong -\frac{\nabla N_D}{N_D} & \hat{n} &\ll N_D \\ \frac{\vec{\mathbf{E}}}{V_T} &\cong \frac{\nabla N_A}{N_A} & \hat{p} &\ll N_A \end{aligned}$$

Using the obtained electric field for the minority carrier current density in equation 3.20a and 3.20b

$$\vec{\mathbf{J}}_n = \frac{q \cdot D_n}{N_A} \cdot \nabla (\hat{n}_p \cdot N_A) \quad (3.21a)$$

$$\vec{\mathbf{J}}_p = -\frac{q \cdot D_p}{N_D} \cdot \nabla (\hat{p}_n \cdot N_D) \quad (3.21b)$$

Substituting the above equations in the steady state carrier concentrations in equation 2.40a and 2.40b assuming negligible recombination yields

$$\nabla (\hat{n} \cdot N_A) = \frac{N_A}{D_n} \cdot \Phi + \frac{N_A}{D_n} \cdot c_n \quad (3.22a)$$

$$\nabla (\hat{p} \cdot N_D) = \frac{N_D}{D_p} \cdot \Phi + \frac{N_D}{D_p} \cdot c_p \quad (3.22b)$$

where c_n and c_p are constants of integration. Equation 3.22a and 3.22b show an ideal photocurrent contribution in the first addend and a constant in the second one. The constant of integration must therefore be negative as the collected current is less than the ideal photocurrent.

Substituting equation 3.22a in 3.21a and analogously for equation 3.22b in 3.21b gives

$$\vec{\mathbf{J}}_n = q \cdot (\Phi + c_n) \quad (3.23a)$$

$$\vec{\mathbf{J}}_p = -q \cdot (\Phi + c_p) \quad (3.23b)$$

The equations for the carrier distribution 3.22a and 3.22b are used to obtain the constants c_p and c_n . These are substituted in equation 3.23a and 3.23b to obtain the current density. But recombination was neglected to obtain the upper equations and this assumption has to be verified in each region.

The electric field in the depletion layer inhibits any majority carrier flow out of the quasi neutral region. The properties of a certain region are determined by its minority carriers. In order to obtain the current contributed by a quasi-neutral region the continuity equations 2.40a and 2.40b are integrated over the volume.

$$\nabla \cdot \vec{\mathbf{J}}_n = q \cdot \left((\nabla \cdot \vec{\Phi}) + \frac{\partial \hat{n}}{\partial t} + \frac{\hat{n}}{\tau_n} \right)$$

$$\nabla \cdot \vec{\mathbf{J}}_p = -q \cdot \left((\nabla \cdot \vec{\Phi}) + \frac{\partial \hat{p}}{\partial t} + \frac{\hat{p}}{\tau_p} \right)$$

Applying Gauss' theorem

$$\int_{\mathbf{V}} \nabla \cdot \vec{f} \, d\mathbf{V} = \oint_A \vec{f} \cdot \vec{n} \, dA$$

gives

$$\begin{aligned}\int_{\mathbf{V}} \nabla \cdot \vec{\mathbf{J}}_n d\mathbf{V} &= q \cdot \int_{\mathbf{V}} \nabla \cdot \vec{\Phi} d\mathbf{V} + \frac{\partial}{\partial t} \int_{\mathbf{V}} q \cdot \hat{n} d\mathbf{V} + \int_{\mathbf{V}} \frac{q \cdot \hat{n}}{\tau_n} d\mathbf{V} \\ \int_A \vec{\mathbf{J}}_n \cdot \vec{n} dA &= q \cdot \int_A \vec{\Phi} \cdot \vec{n} dA + \frac{\partial}{\partial t} \int_{\mathbf{V}} q \cdot \hat{n} d\mathbf{V} + \int_{\mathbf{V}} \frac{q \cdot \hat{n}}{\tau_n} d\mathbf{V}\end{aligned}\quad (3.24a)$$

$$\begin{aligned}\int_{\mathbf{V}} \nabla \cdot \vec{\mathbf{J}}_p d\mathbf{V} &= -q \cdot \int_{\mathbf{V}} \nabla \cdot \vec{\Phi} d\mathbf{V} - \frac{\partial}{\partial t} \int_{\mathbf{V}} q \cdot \hat{p} d\mathbf{V} + \int_{\mathbf{V}} \frac{q \cdot \hat{p}}{\tau_p} d\mathbf{V} \\ \int_A \vec{\mathbf{J}}_p \cdot \vec{n} dA &= -q \cdot \int_A \vec{\Phi} \cdot \vec{n} dA - \frac{\partial}{\partial t} \int_{\mathbf{V}} q \cdot \hat{p} d\mathbf{V} + \int_{\mathbf{V}} \frac{q \cdot \hat{p}}{\tau_p} d\mathbf{V}\end{aligned}\quad (3.24b)$$

The surface integral on the left hand side is the sum of the current towards the surface \mathbf{J}_{pAB} and the current to the depletion layer \mathbf{J}_{pab} as shown in figure 3.1.

In the p-type quasi-neutral region the surface integral over the current density equals the sum of the current to the depletion layer \mathbf{J}_{ncd} and to the rear side surface \mathbf{J}_{nCD} . As the substrate is assumed to be semi-infinite extended all electrons recombine in the volume. Thus the surface recombination velocity (SRV) on the rear side has no influence and \mathbf{J}_{nCD} becomes 0.

The surface integral over the photon flux in the n-well under perpendicular irradiation is the difference between the light impinging on the surface and the one leaving through the boundary to the depletion layer.

$$-q \cdot \int_A \Phi dA = q \cdot (\Phi(0) - \Phi(x_1)) \cdot A \quad (3.25a)$$

In the semi-infinite p-type quasi-neutral region the surface integral over the photon flux is the light passing through the depletion layer.

$$-q \cdot \int_A \Phi dA = q \cdot \Phi(x_2) \cdot A \quad (3.25b)$$

The third integral in equation 3.24b and 3.24a is the total photogenerated excess minority charge stored in the volume. The fourth integral is Q_{tot}/τ assuming the life time does not change along the depth of the region. If the life time changes a weighted average is used.

The current collected inside the quasi-neutral region is the one reaching the boundary to the depletion layer

$$\mathbf{J}_{ncd} = q \cdot \Phi_0(x_2) - \left(\frac{\partial Q_n}{\partial t} + \frac{Q_n}{\tau_n} \right) \quad (3.26a)$$

$$\mathbf{J}_{pab} = (q \cdot \Phi_0(0) - q \cdot \Phi_0(x_1)) - \left(\frac{\partial Q_p}{\partial t} + \frac{Q_p}{\tau_p} + \mathbf{J}_{pAB} \right) \quad (3.26b)$$

The dynamic behavior, i.e. the response time is characterized by the charge control concept. This is a so called quasi-static approximation as the dynamic properties are determined by static quantities. The dynamic behavior is then modeled as a single pole.

The charge control concept regards the time t_s it takes to remove all stored charge carriers Q by the device current.

$$t_s = \frac{Q}{\mathbf{J}} \quad (3.27)$$

The single pole in Laplace space is then given as

$$\bar{\mathbf{J}} = \frac{\mathbf{J}_{DC}}{1 + s \cdot t_s} \quad (3.28)$$

This implies the assumption that all stored charge carriers are removed by the collected photocurrent. An additional sink is the surface recombination. Thus only a portion of the stored charge is actually removed by the collected photocurrent. This can be considered by introducing a collection efficiency $0 < \xi < 1$ in equation 3.28

$$\bar{\mathbf{J}} = \frac{\mathbf{J}_{DC}}{(1 + s \cdot t_s)^\xi}$$

This results in an additional phase which may be realized by an delay line in a commercial circuit simulator. Zoltan Huszka, the author of the model omitted this delay line to reduce the models complexity until measurements results indicate its necessity [11].

3.2.1 n-Well Region

The n-well is the front most layer in the photodiode model. It is approximated by a Gaussian doping profile. The model also features a thin $n+$ diffusion below the surface. There the life time is small and it is assumed that all minority charge carriers generated there immediately recombine. The $n+$ is used to model the surface recombination velocity (SRV) and the parasitic series resistance.

The shape of the minority carrier distribution is assumed to be close to the one with zero recombination. This assumption is justified by the large diffusion length of 80 to 100 μm compared to the small n-well width of usually smaller than 10 μm .

The n-well is created by a diffusion process during fabrication. Hence the doping profile in the n-well is approximated by a Gaussian fit.

$$N_D(x) = N_0 \cdot e^{-\left(\frac{x}{L_N}\right)^2} \quad (3.29)$$

where L_N is the characteristic diffusion length of the n-well doping profile.

The doping profile and the photon flux are substituted in equation 3.22b and integrate results in

$$\hat{p} = \frac{\sqrt{\pi} \cdot \Phi_0 \cdot L_N}{2 \cdot D_p} \cdot \left(c_1 \cdot e^{\left(\frac{x}{L_N}\right)^2} + c_2 \cdot \text{erfcx}\left(\frac{x}{L}\right) - e^{-\alpha \cdot x} \cdot \text{erfcx}\left(\frac{x}{L_N} + \frac{\alpha \cdot L_N}{2}\right) \right) \quad (3.30)$$

As the diffusion constant and the lifetime both depend on the doping concentration average values are used. erfcx is the normalized complimentary error function.

$$\operatorname{erfcx}(y) = e^{y^2} \cdot \operatorname{erfc}(y)$$

In order to obtain the constants c_1 and c_2 in equation 3.30 boundary conditions are necessary. The excess minority holes density becomes 0 at the depletion layer boundary x_1 and the SRV at the silicon-oxide interface determines the slope of the doping concentration.

$$\hat{p}(x_1) = 0/m^3 \quad D_p \cdot \left(\frac{d\hat{p}}{dx} + \hat{p} \cdot \frac{d(\ln N_D)}{dx} \right) = S_p \cdot \hat{p} \Big|_{x=0} \quad (3.31)$$

where S_p is the SRV. Introducing the normalized SRV

$$s_p = \frac{\sqrt{\pi} \cdot S_p \cdot L_N}{2 \cdot D_p}$$

the solutions for the constants c_1 and c_2 are

$$c_1 = \frac{(1 + s_p) \cdot e^{(\frac{\alpha \cdot L_N}{2})^2} \cdot \operatorname{erfc}\left(\frac{x_1}{L_N} + \frac{\alpha \cdot L_N}{2}\right) - \operatorname{erfc}\left(\frac{x_1}{L_N}\right) \cdot (1 + s_p \cdot \operatorname{erfc}\left(\frac{\alpha \cdot L_N}{2}\right))}{1 + s_p \cdot \operatorname{erf}\left(\frac{x_1}{L_N}\right)} \quad (3.32)$$

$$c_2 = \frac{1 + s_p \cdot e^{(\frac{\alpha \cdot L_N}{2})^2} \cdot (\operatorname{erfc}\left(\frac{\alpha \cdot L_N}{2}\right) - \operatorname{erfc}\left(\frac{x_1}{L_N} + \frac{\alpha \cdot L_N}{2}\right))}{1 + s_p \cdot \operatorname{erf}\left(\frac{x_1}{L_N}\right)} \quad (3.33)$$

Integrating equation 3.30 from the surface to the depletion layer boundary x_1 and multiplying with the elementary charge q results in the stored minority charge Q_p . Which is expressed by the intrinsic time constant t_{iF} of the n-well

$$t_{iF} = \frac{L_N^2}{D_p} \quad (3.34)$$

and the normalized charge integral

$$\Sigma_F = L_N \cdot \frac{\sqrt{\pi}}{2} \cdot \int_0^{x_1} c_1 \cdot e^{\left(\frac{x}{L_N}\right)^2} + c_2 \cdot \operatorname{erfcx}\left(\frac{x}{L_N}\right) - e^{-\alpha \cdot x} \cdot \operatorname{erfcx}\left(\frac{x}{L_N} + \frac{\alpha \cdot L_N}{2}\right) dx \quad (3.35)$$

as

$$Q_p = q \cdot \Phi_0(0) \cdot t_{iF} \cdot \Sigma_F \quad (3.36)$$

In order to obtain the current density equation 3.30 is substituted in equation 3.22b to determine the constant c_p .

$$c_p = -\Phi_0 \cdot c_2$$

The constant is used along with equation 3.23b to calculate the current at the silicon-oxide boundary J_{pAB} .

$$\mathbf{J}_{pAB} = \mathbf{J}_p(0) = q \cdot \Phi_0(0) \cdot (1 - c_2)$$

The collected photocurrent is according to equation 3.26b.

$$\begin{aligned}\mathbf{J}_{pab} &= (q \cdot \Phi_0(0) - q \cdot \Phi_0(x_1)) - \left(q \cdot \Phi_0(0) \cdot \frac{t_{iF}}{\tau_p} \cdot \Sigma_F + q \cdot \Phi_0(0) \cdot (1 - c_2) \right) \\ \mathbf{J}_{pab} &= q \cdot \Phi_0(0) \cdot \left(c_2 - e^{-\alpha \cdot x_1} - \frac{t_{iF}}{\tau_p} \cdot \Sigma_F \right)\end{aligned}$$

The response time t_{sF} can be calculated using equation 3.27

$$t_{sF} = \frac{Q_p}{\mathbf{J}_{pab}} = \frac{t_{iF} \cdot \Sigma_F}{c_2 - e^{-\alpha \cdot x_1} - \frac{t_{iF}}{\tau_p} \cdot \Sigma_F}$$

This results in the dynamic photocurrent collected in the n-well

$$\bar{\mathbf{J}}_{pab} = \frac{q \cdot \Phi_0(0)}{1 + s \cdot t_{sF}} \cdot \left(c_2 - e^{-\alpha \cdot x_1} - \frac{t_{iF}}{\tau_p} \cdot \Sigma_F \right) \quad (3.37)$$

3.2.2 Bulk Quasi-neutral Region

As already pictured in figure 3.1 the bulk quasi-neutral region is composed of three different segments.

- Epitaxial layer
- Transition layer
- Substrate

In contrast to the n-well these regions can not be solved individually but have to be computed together. First the general properties of the bulk region are discussed in order to validate assumptions that will simplify the calculation. The homogeneously doped substrate and the epitaxial layer are covered afterward. The transition layer is a result of the diffusion of the dopants from the substrate to the epitaxial layer during the fabrication process. Therefore its doping concentration is changing along the depth of the device. This has to be considered in the charge carrier movement.

The doping profile of the bulk quasi-neutral region is shown in figure 3.2 from x_2 to the right hand side of the plot. The epitaxial layer extends from x_2 to x_L . In the transition layer between x_L and x_H the doping changes from the epitaxial and the substrate doping concentration. A gradient in the doping concentration is associated with an electric field. Its maximum is located at x_3 . Below the transition layer comes the substrate from x_3 onward.

The doping profile is approximated by a piecewise exponential function for the calculation of the minority carrier concentration. The exponential function in the transition layer is fixed to x_3 . At this point the doping concentration equals N_3 . The approximation features a parameter a_E which adjusts the slope and the width of the doping profile. Along with the dimensions of the transition layer the electric field is controlled by a_E . The electric field equals the maximum electric field at x_3 times a_E .

Substrate

At the rear side of the substrate the minority charge carrier density n is assumed to be its equilibrium value n_0 , i.e. the photogenerated carrier density is 0. Thus no surface recombination occurs on the rear side and equation 2.43a for the steady-state becomes

$$\frac{d^2 \hat{n}}{dx^2} - \frac{\hat{n}}{L_{nS}^2} = \frac{1}{D_{nS}} \cdot \frac{d\Phi}{dx}$$

Where the subscript S stands for the substrate.
The boundary conditions for the substrate are

$$\hat{n}(x \rightarrow \infty) = 0/\text{m}^3 \quad \hat{n}(x_H) = \hat{n}_H \quad (3.38)$$

This results in

$$\hat{n}_S(x) = \hat{n}_H \cdot e^{-\frac{x-x_H}{L_{nS}}} + \frac{\Phi_0 \cdot e^{-\alpha x_H}}{\alpha \cdot D_{nS}} \cdot \frac{\alpha^2 \cdot L_{nS}^2}{1 - \alpha^2 \cdot L_{nS}^2} \cdot \left(e^{-\alpha(x-x_H)} - e^{-\frac{x-x_H}{L_{nS}}} \right) \quad (3.39)$$

The diffusion current at x_H is

$$\begin{aligned} \mathbf{J}_{DS}(x_H) &= q \cdot D_{nS} \cdot \left. \frac{d\hat{n}_S}{dx} \right|_{x=x_H} \\ \mathbf{J}_{DS}(x_H) &= q \cdot \Phi_0(x_H) \cdot \left(\frac{\alpha \cdot L_{nS}}{1 + \alpha \cdot L_{nS}} - \frac{\hat{n}_H \cdot D_{nS}}{L_{nS}} \cdot \frac{1}{\Phi_0 \cdot e^{-\alpha x_H}} \right) \end{aligned} \quad (3.40)$$

In order to obtain the solution the value \hat{n}_H at the boundary is needed. This quantity is determined by the transition layer.

Epitaxial Layer

The recombination in the lightly doped epitaxial layer is small and thus neglected in the continuity equation 2.43a. The differential equation becomes

$$\frac{d^2 \hat{n}_E}{dx^2} = \frac{1}{D_{nE}} \cdot G(x)$$

Applying the integral twice yields

$$\hat{n}_E(x) = -\frac{\Phi_0}{\alpha \cdot D_{nE}} \cdot e^{-\alpha x} + c_{2E} \cdot x + c_{1E}$$

With the boundary conditions

$$\hat{n}(x_2) = 0/\text{m}^3 \quad \hat{n}(x_L) = \hat{n}_L$$

the minority charge carrier concentration becomes

$$\begin{aligned} \hat{n}_E(x) = & -\frac{\Phi_0}{\alpha \cdot D_{nE}} \cdot e^{-\alpha \cdot x_2} \cdot \left(e^{-\alpha \cdot (x-x_2)} - 1 \right) \\ & + \left(\hat{n}_L + \frac{\Phi_0}{\alpha \cdot D_{nE}} \cdot e^{-\alpha \cdot x_2} \cdot \left(e^{-\alpha \cdot w_{Epi}} - 1 \right) \right) \cdot \frac{x - x_2}{w_{Epi}} \end{aligned} \quad (3.41)$$

Where $w_{Epi} = x_L - x_2$ is the width of the epitaxial layer. In order to calculate the current density in the epitaxial layer $\mathbf{J}_E(x)$ equations 3.22a and 3.23a are used. The derivative of the electron concentration times the epitaxial doping equals

$$\begin{aligned} \frac{d}{dx}(N_E \cdot \hat{n}_E) &= N_E \cdot \frac{\Phi_0}{D_{nE}} \cdot e^{-\alpha \cdot x} \\ &+ \left(\hat{n}_L + \frac{\Phi_0}{\alpha \cdot D_{nE}} \cdot e^{-\alpha \cdot x_2} \cdot \left(e^{-\alpha \cdot w_{Epi}} - 1 \right) \right) \cdot \frac{N_E}{w_{Epi}} \\ \frac{d}{dx}(N_E \cdot \hat{n}_E) &= \frac{N_E}{D_{nE}} \cdot \Phi(x) + \frac{N_E}{D_{nE}} \cdot \underbrace{\left(\frac{D_{nE}}{w_{Epi}} \cdot \hat{n}_L + \frac{\Phi_0 \cdot e^{-\alpha \cdot x_2}}{\alpha \cdot w_{Epi}} \cdot \left(e^{-\alpha \cdot w_{Epi}} - 1 \right) \right)}_{c_n} \end{aligned} \quad (3.42)$$

Comparing this with equation 3.22a gives the integration constant c_n as marked in equation 3.42. Therefore the current density according to equation 3.23a reads as

$$\mathbf{J}_{DE}(x) = q \cdot \left(\frac{D_{nE}}{w_{Epi}} \cdot \hat{n}_L + \frac{\Phi_0 \cdot e^{-\alpha \cdot x_2}}{\alpha \cdot w_{Epi}} \cdot \left(e^{-\alpha \cdot w_{Epi}} - 1 \right) + \Phi_0 \cdot e^{-\alpha \cdot x} \right) \quad (3.43)$$

Transition Layer

In the previously discussed substrate and epitaxial layer the quantities \hat{n}_H and \hat{n}_L are still unknown. The transition layer links both quantities. The changing doping concentration leads to a more sophisticated calculation of the minority charge carrier distribution. As already mentioned at the beginning of this section the doping profile is approximated by an exponential function for the calculation of the minority charge carrier concentration. In a logarithmic plot this functions is a straight line, which slope is adjusted by a parameter aE . This parameter is the relation of the slope of the approximated function and the maximum slope of the real doping profile.

The point x_3 , N_3 is determined by the electric field maximum. The electric field is caused by the gradient of the doping concentration as

$$\mathbf{E} = V_T \cdot \frac{1}{N_T} \cdot \frac{dN_T}{dx}$$

The doping profile for the calculation of the electric field maximum is not approximated by an exponential function. Instead the complimentary error function is used.

$$N_T = N_E + \frac{N_S - N_E}{2} \cdot \operatorname{erfc}\left(\frac{w_{Epi} - x}{L_{ES}}\right) \quad (3.44)$$

Where L_{ES} is the characteristic diffusion length of the doping profile in the transition layer. Using the normalized position u

$$\begin{aligned} u &= \frac{w_{Epi} - x}{L_{ES}} \\ du &= -\frac{1}{L_{ES}} \cdot dx \end{aligned} \quad (3.45)$$

Thus the electric field becomes

$$\mathbf{E} = \frac{V_T}{N_T \cdot L_{ES}} \cdot \frac{dN_T}{du} \quad (3.46)$$

The maximum is obtained by setting the first derivative along u to 0

$$\frac{d\mathbf{E}}{du} \stackrel{!}{=} 0$$

$$\frac{d}{du} \left(\frac{1}{N_T} \cdot \frac{dN_T}{du} \right) = 0 \quad (3.47)$$

Calculating the outermost derivation

$$\frac{d}{du} \left(\frac{1}{N_T} \cdot \frac{dN_T}{du} \right) = - \left(\frac{1}{N_T} \cdot \frac{dN_T}{du} \right)^2 + \frac{1}{N_T} \cdot \frac{d^2 N_T}{du^2} \quad (3.48)$$

The first and second derivatives equal

$$\begin{aligned} \frac{dN_T}{du} &= \frac{N_S - N_E}{\sqrt{\pi}} \cdot e^{-u^2} \\ \frac{d^2 N_T}{du^2} &= -2 \cdot u \cdot \frac{dN_T}{dx} = -2 \cdot u \cdot \frac{N_S - N_E}{\sqrt{\pi}} \cdot e^{-u^2} \end{aligned}$$

Using the doping profile of equation 3.44 and substitute the derivatives in equation 3.47 and 3.48 yields

$$\frac{1}{N_E + \frac{N_S - N_E}{2} \cdot \operatorname{erfc}(u)} \cdot \left(\frac{N_S - N_E}{\sqrt{\pi}} \right)^2 \cdot e^{-2 \cdot u^2} + 2 \cdot u \cdot \frac{N_S - N_E}{\sqrt{\pi}} \cdot e^{-u^2} = 0$$

Separating u gives

$$\ln \left| \frac{e^{-u^2}}{u \cdot \pi} - \operatorname{erfc}(u) \right| = -\ln \left| \frac{N_S - N_E}{2 \cdot N_E} \right|$$

The left hand side is approximated by a second order parabola and u_{max} can be determined by

$$u_{max} = -1.1433 + \sqrt{1.307 + \frac{\ln \left| \frac{N_S - N_E}{2 \cdot N_E} \right| - 0.4321}{0.8373}} \quad (3.49)$$

Denormalizing back to x according to equation 3.45 results in the position of the electric field maximum.

$$x_3 = w_{Epi} - L_{ES} \cdot u_{max} \quad (3.50)$$

The electric field itself is determined by

$$\mathbf{E}_{Tm} = \frac{1}{L_{ES} \cdot \sqrt{\pi} \cdot \frac{N_3}{N_S - N_E} \cdot e^{u_{max}^2}} \quad (3.51)$$

with N_3 the doping concentration given by equation 3.44 at position x_3 .

As the doping profile and the resulting electric field are determined the charge carrier density is computed next. Introducing

$$M(x) = \frac{N(x)}{D(x)} \quad (3.52)$$

one can reformulate equation 3.22a to

$$\nabla (\hat{n}_T \cdot N_T) = M(x) \cdot \Phi(x) + M(x) \cdot c_{nT} \quad (3.53)$$

Where the index T symbolizes the transition layer. During the derivation of equation 3.22a and therefore 3.53 recombination was neglected. This assumption is not as well met as in the lightly doped epitaxial layer. However it is justified as the slope in the doping profile causes an electric field which removes charge carriers. This effectively increases the mean free path of the charge carriers. In addition the typical width of the transition layer is about $4\mu m$ while the electron diffusion length in the highly doped substrate is about $8\mu m$. As the doping concentration increases from the epitaxial concentration to the one in the substrate the effective mean free path is larger than in the substrate. Thus the mean free path of the electrons exceeds the width of the transition layer again justifying the assumption of negligible recombination.

The minority charge carrier concentration is determined while approximating the doping profile, the function $M(x)$ and the reciprocal diffusion constant D_n by an exponential function.

$$N(x) = N_E \cdot e^{a_E \cdot E_{Tm} \cdot (x - x_L)} \quad (3.54a)$$

$$M(x) = \frac{N_E}{D_{nE}} \cdot e^{a_E \cdot \beta_M \cdot (x - x_L)} \quad (3.54b)$$

$$\frac{1}{D(x)} = \frac{1}{D_{nE}} \cdot e^{a_E \cdot \beta_D \cdot (x - x_L)} \quad (3.54c)$$

These assumptions basically generate a homogeneous electric field across the transition layer. The quantity a_E approximates the electric field and is a parameter of the model as will be discussed in chapter 4. The electric field of the approximation is given by substituting equation 3.54a in 3.46. This results in an approximated electric field of $a_E \cdot E_{Tm}$.

The unknown β_M is given by the boundary conditions

$$\begin{aligned} x = x_H : \quad M(x_H) &= \frac{N_S}{D_{nS}} \\ N_T(x_H) &= N_S \\ \\ x = x_L : \quad N_T(x_L) &= N_E \end{aligned}$$

Introducing the transition layer width w_T

$$w_T = x_H - x_L \tag{3.55}$$

and using equation 3.54b in the first boundary condition results in

$$\frac{N_E}{D_{nE}} \cdot e^{a_E \cdot \beta_M \cdot (x_H - x_L)} = \frac{N_S}{D_{nS}}$$

Reordering the equation gives

$$e^{a_E \cdot \beta_M \cdot w_T} = \frac{N_S}{N_E} \cdot \frac{D_{nE}}{D_{nS}} \tag{3.56}$$

The relation between the substrate and the epitaxial layer doping concentration can be expressed by combining the second and third equation listed in the boundary condition.

$$\frac{N_S}{N_E} = e^{a_E \cdot E_{Tm} \cdot w_T}$$

Thus β_M is obtained by equation 3.56

$$\begin{aligned} e^{a_E \cdot \beta_M \cdot w_T} &= \frac{D_{nE}}{D_{nS}} \cdot e^{a_E \cdot E_{Tm} \cdot w_T} \\ e^{a_E \cdot (\beta_M - E_{Tm}) \cdot w_T} &= \frac{D_{nE}}{D_{nS}} \\ \beta_M &= \frac{1}{a_E \cdot w_T} \cdot \ln \left| \frac{D_{nE}}{D_{nS}} \right| + E_{Tm} \end{aligned}$$

Introducing β_D

$$\beta_D = \frac{1}{a_E \cdot w_T} \cdot \ln \left| \frac{D_{nE}}{D_{nS}} \right|$$

results in

$$\beta_M = \beta_D + E_{Tm} \quad (3.57)$$

The charge carrier concentration is obtained by equation 3.53. Expanding this formula as given below

$$\begin{aligned} \frac{d}{dx} (\hat{n}_T \cdot N_T) &= M(x) \cdot c_{2T} + M(x) \cdot \Phi(x) & / \cdot \frac{\Phi(x_L)}{\alpha \cdot w_T} \\ \frac{d}{dx} (\hat{n}_T \cdot N_T) &= \frac{\Phi(x_L)}{\alpha \cdot w_T} \cdot \left(M(x) \cdot \underbrace{\frac{c_{nT}}{\frac{\Phi(x_L)}{\alpha \cdot w_T}}}_{c_{2T}} + M(x) \cdot \alpha \cdot w_T \cdot e^{-\alpha \cdot (x-x_L)} \right) \end{aligned} \quad (3.58)$$

In order to determine the charge carrier density normalized quantities are used to achieve manageable expressions. The normalized carrier concentration equals

$$n_T(x) = \frac{\alpha \cdot D_{nE}}{\Phi(x_L)} \cdot \hat{n}_T(x) \quad (3.59)$$

The normalization is used in equation 3.58.

$$\begin{aligned} \frac{d}{dx} (\hat{n}_T \cdot N_T) &= \frac{\Phi(x_L)}{\alpha \cdot w_T} \cdot \left(M(x) \cdot c_{2T} + M(x) \cdot \alpha \cdot w_T \cdot e^{-\alpha \cdot (x-x_L)} \right) & / \cdot \frac{\alpha \cdot D_{nE}}{\Phi(x_L)} \\ \frac{d}{dx} (n_T \cdot N_T) &= \frac{D_{nE}}{w_T} \cdot M(x) \cdot c_{2T} + D_{nE} \cdot M(x) \cdot \alpha \cdot e^{-\alpha \cdot (x-x_L)} \end{aligned} \quad (3.60)$$

The original constant c_n has been replaced as marked above by

$$c_{nT} = \frac{\Phi(x_L)}{\alpha \cdot w_T} \cdot c_{2T} \quad (3.61)$$

The constant c_{2T} is obtained by substituting $M(x)$ of equation 3.54b in 3.60

$$\begin{aligned} \frac{d}{dx} (n_T \cdot N_T) &= \frac{N_E}{D_{nE}} \cdot e^{a_E \cdot \beta_M \cdot (x-x_L)} \cdot \left(\frac{D_{nE}}{w_T} \cdot c_{2T} + D_{nE} \cdot \alpha \cdot e^{-\alpha \cdot (x-x_L)} \right) \\ \frac{d}{dx} (n_T \cdot N_T) &= N_E \cdot e^{a_E \cdot \beta_M \cdot (x-x_L)} \cdot \frac{c_{2T}}{w_T} + N_E \cdot e^{a_E \cdot \beta_M \cdot (x-x_L)} \cdot \alpha \cdot e^{-\alpha \cdot (x-x_L)} \end{aligned} \quad (3.62)$$

An integration of equation 3.62 yields

$$n_T(x) = \underbrace{e^{-a_E \cdot E_{Tm} \cdot (x-x_L)}}_{p(x)} \cdot c_{1T} + \underbrace{\frac{e^{a_E \cdot \beta_D \cdot (x-x_L)}}{a_E \cdot \beta_M \cdot w_T}}_{q(x)} \cdot c_{2T} + \underbrace{\frac{\alpha \cdot e^{(a_E \cdot \beta_D - \alpha) \cdot x}}{a_E \cdot \beta_D - \alpha}}_{r(x)} \cdot e^{-(a_E \cdot \beta_D - \alpha) \cdot x_L} \quad (3.63)$$

The three functions marked above are introduced to simplify the expressions to come. The coefficients c_{1T} and c_{2T} are determined by the boundary conditions.

$$\begin{aligned} x = x_L : \quad \hat{n}(x_L) &= \hat{n}_L \\ x = x_H : \quad \hat{n}(x_H) &= \hat{n}_H \end{aligned}$$

During the calculation of c_{1T} and c_{2T} and in the following sections the following notations will be used

$$\begin{vmatrix} a(x_L) & b(x_L) \\ a(x_H) & b(x_H) \end{vmatrix} = (a, b)$$

$$\frac{a}{(p, q)} = \tilde{a}$$

Thus the coefficients can be written as

$$\begin{aligned} c_{1T} &= \frac{(n_T, q) - (r, q)}{(p, q)} \\ c_{2T} &= \frac{(n_T, p) + (r, p)}{(p, q)} \end{aligned}$$

The current density of the transition layer is obtained by replacing c_{nT} in equation 3.23a by the relation given in 3.61.

$$J_{DT}(x) = q \cdot \left(\Phi(x) + \frac{c_{2T}}{\alpha \cdot w_T} \cdot \Phi(x_L) \right) \quad (3.64)$$

Bulk Region Current

During the investigation of the bulk quasi-neutral region two still unknown quantities have been introduced. These are the minority charge carrier densities at the boundaries between the different layers \hat{n}_L and \hat{n}_H . They are expressed by the constants c_{1T} and c_{2T} of the transition layer. The photocurrent at the zone boundaries x_L and x_H has to be continuous. The current densities of the different regions are given in equation 3.40, 3.43 and 3.64, respectively.

c_{2S} and c_{2E} are defined before starting with the calculation of \hat{n}_L and \hat{n}_H . They are constants of integration similar to c_{1T} and c_{2T} in the transition layer.

$$c_{2S} = \frac{\alpha \cdot D_{nS}}{\Phi(x_H)} \cdot \hat{n}_H + \frac{\alpha \cdot L_{nS}}{1 + \alpha \cdot L_{nS}} \quad (3.65)$$

$$c_{2E} = \frac{\alpha \cdot D_{nE}}{\Phi(x_2)} \cdot \hat{n}_L - 1 + e^{-\alpha \cdot w_E} \quad (3.66)$$

At the boundary between epitaxial and transition layer x_L the current densities are

$$\begin{aligned}\mathbf{J}_{DE}(x_L) &= q \cdot \left(\Phi(x_L) + \frac{c_{2E}}{\alpha \cdot w_E} \cdot \Phi(x_2) \right) \\ \mathbf{J}_{DT}(x_L) &= q \cdot \left(\Phi(x_L) + \frac{c_{2T}}{\alpha \cdot w_T} \cdot \Phi(x_L) \right)\end{aligned}$$

and therefore

$$q \cdot \left(\Phi(x_L) + \frac{c_{2E}}{\alpha \cdot w_E} \cdot \Phi(x_2) \right) = q \cdot \left(\Phi(x_L) + \frac{c_{2T}}{\alpha \cdot w_T} \cdot \Phi(x_L) \right)$$

This leads to a relation between c_{2E} and c_{2T}

$$c_{2E} \cdot \frac{w_T}{w_E} = c_{2T} \cdot e^{-\alpha \cdot w_E} \quad (3.67)$$

The current densities on the boundary at x_H are

$$\begin{aligned}\mathbf{J}_{DT}(x_H) &= q \cdot \left(\Phi(x_H) + \frac{c_{2T}}{\alpha \cdot w_T} \cdot \Phi(x_L) \right) \\ \mathbf{J}_{DS}(x_H) &= q \cdot \Phi_0(x_H) \cdot \left(\frac{\alpha \cdot L_{nS}}{1 + \alpha \cdot L_{nS}} - \frac{\hat{n}_H \cdot D_{nS}}{L_{nS}} \cdot \frac{1}{\Phi_0 \cdot e^{-\alpha \cdot x_H}} \right)\end{aligned}$$

Applying the current continuity

$$\begin{aligned}q \cdot \left(\Phi(x_H) + \frac{c_{2T}}{\alpha \cdot w_T} \cdot \Phi(x_L) \right) &= q \cdot \Phi(x_H) \cdot \left(\frac{\alpha \cdot L_{nS}}{1 + \alpha \cdot L_{nS}} - \frac{\hat{n}_H \cdot D_{nS}}{L_{nS}} \cdot \frac{1}{\Phi(x_H)} \right) \\ q \cdot \Phi(x_H) \cdot \left(1 + \frac{c_{2T}}{\alpha \cdot w_T} \cdot e^{\alpha \cdot w_T} \right) &= q \cdot \Phi(x_H) \cdot \left(\frac{\alpha \cdot L_{nS}}{1 + \alpha \cdot L_{nS}} - \frac{D_{nS}}{L_{nS}} \cdot \frac{\hat{n}_H}{\Phi(x_H)} \right) \\ \frac{c_{2T}}{\alpha \cdot w_T} \cdot e^{\alpha \cdot w_T} &= -\frac{1}{1 + \alpha \cdot L_{nS}} - \frac{D_{nS}}{L_{nS}} \cdot \frac{\hat{n}_H}{\Phi(x_H)} \\ \frac{L_{nS}}{w_T} \cdot c_{2T} \cdot e^{\alpha \cdot w_T} &= -\underbrace{\left(\frac{\alpha \cdot D_{nS}}{\Phi(x_H)} \cdot \hat{n}_H + \frac{\alpha \cdot L_{nS}}{1 + \alpha \cdot L_{nS}} \right)}_{c_{2S}}\end{aligned}$$

and the relation between c_{2T} and c_{2S}

$$c_{2T} \cdot \frac{L_{nS}}{w_T} = -c_{2S} \cdot e^{-\alpha \cdot w_T} \quad (3.68)$$

The constants c_2 in equation 3.67 and 3.68 are substituted as given in their particular sections

$$\frac{\alpha \cdot D_{nE}}{\Phi(x_2)} \cdot \frac{w_T}{w_E} \cdot \hat{n}_E(x_L) + \frac{(n_T, p)}{(p, q)} \cdot e^{-\alpha \cdot w_E} = (1 - e^{-\alpha \cdot w_E}) \cdot \frac{w_T}{w_E} + \frac{(r, p)}{(p, q)} \cdot e^{\alpha \cdot w_E} \quad (3.69a)$$

$$\frac{(n_T, p)}{(p, q)} \cdot \frac{L_{nS}}{w_T} - \frac{\alpha \cdot D_{nS}}{\Phi(x_H)} \cdot e^{-\alpha \cdot w_T} \cdot \hat{n}_S(x_H) = \frac{(r, p)}{(p, q)} \cdot \frac{L_{nS}}{w_T} + \frac{\alpha \cdot L_{nS}}{1 + \alpha \cdot L_{nS}} \cdot e^{-\alpha \cdot w_T} \quad (3.69b)$$

In order to obtain a linear system of equations for \hat{n}_L and \hat{n}_H the normalized carrier concentrations in the transition layer n_T and the carrier concentration in the substrate \hat{n}_S have to be replaced. First the carrier concentrations in the epitaxial layer and the substrate are normalized

$$n_E(x) = \frac{\alpha \cdot D_{nE}}{\Phi_0 \cdot e^{-\alpha \cdot x_2}} \cdot \hat{n}_E(x) \quad (3.70)$$

$$n_S(x) = \frac{\alpha \cdot D_{nS}}{\Phi_0 \cdot e^{-\alpha \cdot x_H}} \cdot \hat{n}_S(x) \quad (3.71)$$

The carrier concentrations of the transition layer and the substrate are formulated using the carrier concentrations in the epitaxial layer

$$n_T(x_L) = \frac{\alpha \cdot D_3}{\Phi_0 \cdot e^{-\alpha \cdot x_L}} \cdot \hat{n}_L \quad / \cdot \frac{\frac{\Phi_0 \cdot e^{-\alpha \cdot x_2}}{\alpha \cdot D_{nE}}}{\frac{\Phi_0 \cdot e^{-\alpha \cdot x_2}}{\alpha \cdot D_{nE}}}$$

$$n_T(x_H) = \frac{\alpha \cdot D_3}{\Phi_0 \cdot e^{-\alpha \cdot x_L}} \cdot \hat{n}_H \quad / \cdot \frac{\frac{\Phi_0 \cdot e^{-\alpha \cdot x_2}}{\alpha \cdot D_{nE}}}{\frac{\Phi_0 \cdot e^{-\alpha \cdot x_2}}{\alpha \cdot D_{nE}}}$$

$$n_S(x_H) = \frac{\alpha \cdot D_{nS}}{\Phi_0 \cdot e^{-\alpha \cdot x_H}} \cdot \hat{n}_H \quad / \cdot \frac{\frac{\Phi_0 \cdot e^{-\alpha \cdot x_2}}{\alpha \cdot D_{nE}}}{\frac{\Phi_0 \cdot e^{-\alpha \cdot x_2}}{\alpha \cdot D_{nE}}}$$

The carrier concentration at the zone boundaries are also normalized to the concentration in the epitaxial layer

$$n_{LE} = \frac{\hat{n}_L}{\frac{\Phi(x_2)}{\alpha \cdot D_{nE}}} \quad (3.72a)$$

$$n_{HE} = \frac{\hat{n}_H}{\frac{\Phi(x_2)}{\alpha \cdot D_{nE}}} \quad (3.72b)$$

This results in

$$n_T(x_L) = n_{LE} \cdot \frac{D_3}{D_{nE}} \cdot e^{\alpha \cdot w_E}$$

$$\tilde{n}_T(x_H) = n_{HE} \cdot \frac{D_3}{D_{nE}} \cdot e^{\alpha \cdot w_E}$$

$$n_S(x_H) = n_{HE} \cdot \frac{D_{nS}}{D_{nE}} \cdot e^{\alpha \cdot (w_E + w_T)}$$

Using the normalized quantities in equation 3.69a and 3.69b gives

$$\left(\frac{w_T}{w_E} + \tilde{p}_H \right) \cdot n_{LE} - \tilde{p}_L \cdot n_{HE} = (1 - e^{-\alpha \cdot w_E}) \cdot \frac{w_T}{w_E} + \frac{(r, p)}{(p, q)} \cdot e^{\alpha \cdot w_E} \quad (3.73a)$$

$$\begin{aligned} \frac{L_{nS}}{w_T} \cdot \tilde{p}_H \cdot n_{LE} + \left(-\frac{L_{nS}}{w_T} \cdot \tilde{p}_L - \frac{D_{nS}}{D_{nE}} \right) \cdot n_{HE} \\ = \frac{(r, p)}{(p, q)} \cdot \frac{L_{nS}}{w_T} \cdot e^{-\alpha \cdot w_E} + \frac{\alpha \cdot L_{nS}}{1 + \alpha \cdot L_{nS}} \cdot e^{-\alpha \cdot (w_E + w_T)} \end{aligned} \quad (3.73b)$$

The above equations can be transformed in a matrix notation

$$\begin{aligned} \begin{bmatrix} \frac{w_T}{w_E} + \tilde{p}_H & -\tilde{p}_L \\ \frac{L_{nS}}{w_T} \cdot \tilde{p}_H & -\frac{L_{nS}}{w_T} \cdot \tilde{p}_L - \frac{D_{nS}}{D_{nE}} \end{bmatrix} \cdot \begin{pmatrix} n_{LE} \\ n_{HE} \end{pmatrix} \\ = \begin{pmatrix} (1 - e^{-\alpha \cdot w_E}) \cdot \frac{w_T}{w_E} + \frac{(r, p)}{(p, q)} \cdot e^{\alpha \cdot w_E} \\ \frac{(r, p)}{(p, q)} \cdot \frac{L_{nS}}{w_T} \cdot e^{-\alpha \cdot w_E} + \frac{\alpha \cdot L_{nS}}{1 + \alpha \cdot L_{nS}} \cdot e^{-\alpha \cdot (w_E + w_T)} \end{pmatrix} \end{aligned} \quad (3.74)$$

The normalized carrier concentrations n_{LE} and n_{HE} are obtained by inverting the matrix. They are used to calculate the quantities encountered throughout the computation of the bulk quasi-neutral region. Most notable the constants c_{2S} by equation 3.65, c_{2E} by 3.66 and c_{2T} by 3.67.

The collected photocurrent from the bulk quasi-neutral region is given in equation 3.43. Using the constant of integration c_{2E} from equation 3.66 the collected photocurrent can be simplified to

$$\mathbf{J}_{DE}(x_2) = q \cdot \Phi(x_2) \cdot \left(1 + \frac{c_{2E}}{\alpha \cdot w_E} \right) \quad (3.75)$$

According to equation 2.49 the quantum efficiency QE_B of the bulk quasi-neutral region becomes

$$QE_B = e^{-\alpha \cdot x_2} \cdot \left(1 + \frac{c_{2E}}{\alpha \cdot w_E} \right)$$

The response time is calculated as the stored minority charge in the region over the photocurrent. The stored minority charge is expressed by the intrinsic time constant t_i

and the normalized charge integral Σ similar to the n-well region. The total charge is the sum of the individual charges of the epitaxial layer, transition layer and the substrate. The charge stored of the latter is obtained by integrating equation 3.39 from x_H to inf . The intrinsic time constant equals the minority electron lifetime in the substrate τ_{nS} .

$$QE_S = q \cdot \Phi(x_2) \cdot \tau_{nS} \cdot \Sigma_S \quad (3.76)$$

The normalized charge integral of the substrate equals

$$\Sigma_S = \left(\frac{n_S(x_H)}{\alpha \cdot L_{nS}} + \frac{1}{1 + \alpha \cdot L_{nS}} \right) \cdot e^{-\alpha \cdot (w_E + w_T)} \quad (3.77)$$

The charge stored in the epitaxial layer is obtained by integrating equation 3.41 from x_2 to x_L .

$$QE_E = q \cdot \Phi(x_2) \cdot t_E \cdot \Sigma_E \quad (3.78)$$

The intrinsic time constant of the epitaxial layer is

$$t_{iE} = \frac{w_E}{\alpha \cdot D_{nE}} \quad (3.79)$$

The normalized charge integral of the substrate equals

$$\Sigma_E = 1 + \frac{n_{EL}}{2} - \left(0.5 + \frac{1}{\alpha \cdot L_{nS}} \right) \cdot (1 - e^{-\alpha \cdot w_E}) \quad (3.80)$$

The intrinsic time constant of the transition layer is

$$t_{iT} = \frac{1}{a_E \cdot \alpha \cdot E_{Tm} \cdot D_{nE}} \quad (3.81)$$

The charge stored in the transition layer is calculated by integrating equation 3.63 from x_L to x_H .

$$QE_T = q \cdot \Phi(x_2) \cdot t_{iT} \cdot \Sigma_T \quad (3.82)$$

The normalized charge integral of the substrate equals

$$\Sigma_T = (\Sigma_{T1} + \Sigma_{T2} + \Sigma_{T3}) \cdot e^{-\alpha \cdot w_E} \quad (3.83)$$

were Σ_{T1} , Σ_{T2} and Σ_{T3} are

$$\begin{aligned} \Sigma_{T1} &= p_L \cdot (1 - e^{-a_E \cdot E_{Tm} \cdot w_T}) \\ \Sigma_{T2} &= q_L \cdot \frac{E_{Tm}}{\beta_D} \cdot (e^{a_E \cdot \beta_D \cdot w_T} - 1) \\ \Sigma_{T3} &= r_L \cdot \frac{a_E \cdot E_{Tm}}{a_E \cdot \beta_D - \alpha} \cdot (e^{(a_E \cdot \beta_D - \alpha) \cdot w_T} - 1) \end{aligned}$$

Thus the response time of the bulk quasi-neutral region is determined by

$$t_{sB} = \frac{Q_S + Q_E + Q_T}{J_{DE}(x_2)}$$

Substituting the stored charges with equation 3.76, 3.78 and 3.82 as well as the current density in equation 3.75 results in

$$t_{sB} = \frac{t_{iE} \cdot \Sigma_E + t_{iT} \cdot \Sigma_T + \tau_{nS} \cdot \Sigma_S}{1 + \frac{c_{2E}}{\alpha \cdot w_E}} \quad (3.84)$$

Thus the collected photocurrent of the bulk quasi-neutral region is determined by

$$\bar{J}_{ncd} = q \cdot \Phi_0(0) \cdot e^{-\alpha \cdot x_2} \cdot \frac{1 + \frac{c_{2E}}{\alpha \cdot w_E}}{1 + s \cdot t_{sB}} \quad (3.85)$$

3.3 Equivalent Circuit

In order to efficiently solve the equation stated in the previous sections of this chapter an equivalent circuit is used. The quantum efficiencies and response times for the five aforementioned regions are represented as component values. These are calculated by Verilog-A, a hardware description language. It allows for an easy implementation of complex relations into simple circuit components. The result is an equivalent circuit. This equivalent circuit is then simulated by an appropriate program, e.g. SPICE. In this section the structure of the equivalent circuit is presented.

Figure 3.3 displays the equivalent circuit of a photodiode with epitaxial grown layer. Different groups of components represent a specific region of the model as pictured by the dashed boxes in figure 3.3. Number 1 incorporates the transmittance of the ARC as well as the absorption coefficient. Group 2 covers the response time of the depletion layer. Its special position inside the circuit stems from the fact that each collected charge carrier has to travel through the depletion layer as given in equation 3.17. Groups 3, 5, 6 and 7 are the responsivity and response time of the n-well, epitaxial layer, transition layer and substrate. Number 4 represents the stationary responsivity of the depletion layer only as its response time is already integrated in 2. The non-opto-electronic properties like dark current and capacitance of the photodiode are collected in a separate standard diode model [11]. Along with a series resistance this diode is located in 8.

The dynamic behavior of the individual regions is modeled by equation 3.28. Therefore first order RC filters can be used to implement the response times. This is done by setting $R = 1\Omega$ and C to the calculated response time.

Temperature, doping concentrations and all other contributions mentioned before change the values of the individual components in the equivalent circuit. The configuration itself is determined by the device structure. For example group number 5 for the epitaxial layer

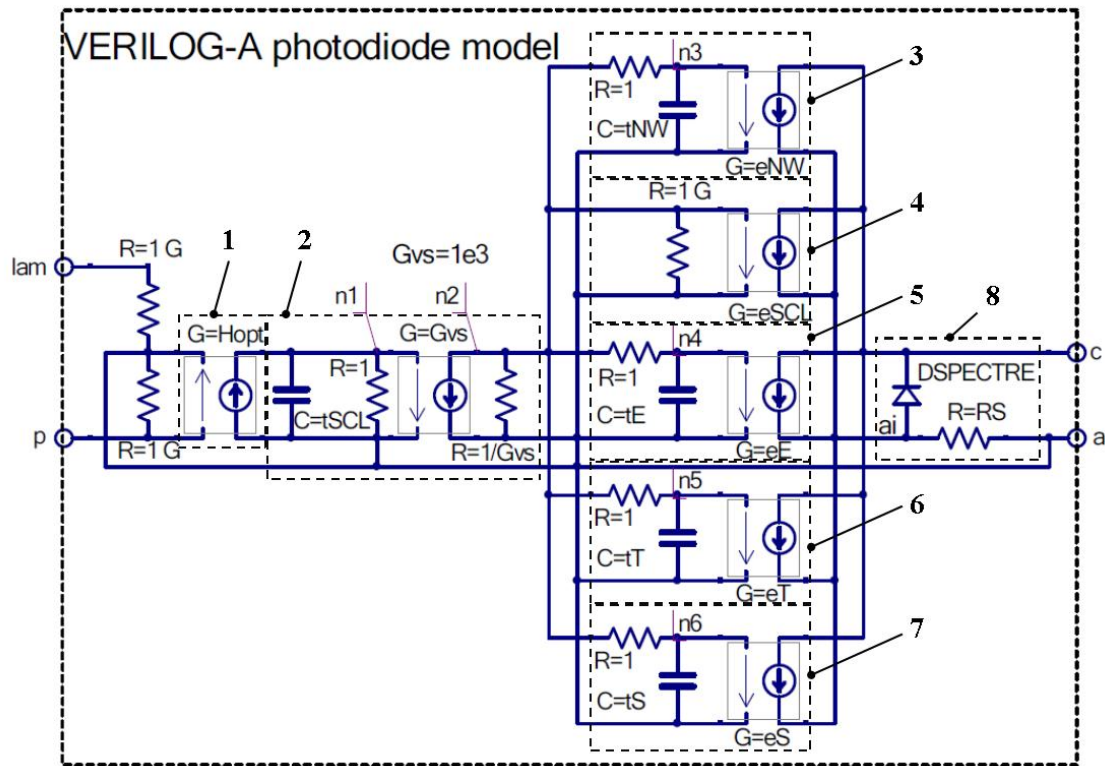


Figure 3.3: Equivalent circuit of a photodiode with epitaxial grown layer [11], page 101, modified. The groups of components serve the following purpose:

- 1: ARC transmittance and absorption coefficient
- 2: Response time space charge layer
- 3: n-well
- 4: Responsivity space charge layer
- 5: Epitaxial layer
- 6: Transition layer
- 7: Substrate
- 8: Standard diode model and series resistance

and 6 for the transition layer would not be included in a model for a photodiode without epitaxial layer.

Chapter 4

Parameter Extraction Strategy

In the previous chapter, a model was introduced and verified regarding the assumptions and simplifications to obtain a model suitable for a circuit simulator. A set of parameters are used to fit this model to measurements. These parameters will be classified into process parameters (e.g. doping, distances), instance parameters (e.g. width and length) and pure fitting parameters.

In this chapter, the characteristics detailed in section 2.2.2 are subject to a sensitivity analysis. The impact is investigated and the parameters are ordered accordingly to obtain a parameter extraction strategy. A characteristic is typically influenced by a fraction of the parameter set. Therefore only the parameters with detectable impact are discussed. The parameters will be fitted one at a time as a first step. A subsequent multiparameter fit optimizes the parameters. Starting with a multiparameter fit may cause difficulties for the convergence of the optimizer. The optimizer itself processes the parameters in an user defined order. The sequence of parameters for the single- and multiparameter fit has to be retained.

The diode parameters for dark condition are extracted using a well established strategy [12, 13, 14]. This thesis focuses on the optical parameters.

Parameters associated with the doping profile and device dimensions are fixed. Doping concentrations and related distances are extracted from the doping profile. Device width W and length L are set by the circuit designer. The parameters used for the extraction strategy are detailed at the beginning of this chapter.

4.1 Parameters

$dbarc$ sets the thickness of the BARC on top of the photodiode. This significantly changes the transmittance as discussed in section 2.1.3. The position of $dbarc$ in the photodiode is illustrated in figure 4.1.



Figure 4.1: Parameter $dbarc$ sets BARC thickness.

$dnpp$ is the width of the heavily doped n-layer below the ARC of the photodiode. Charge carriers are assumed to immediately recombine there. Hence this volume does not contribute to the photocurrent. The position of $dnpp$ in the photodiode is pictured in the doping profile given in figure 4.2.

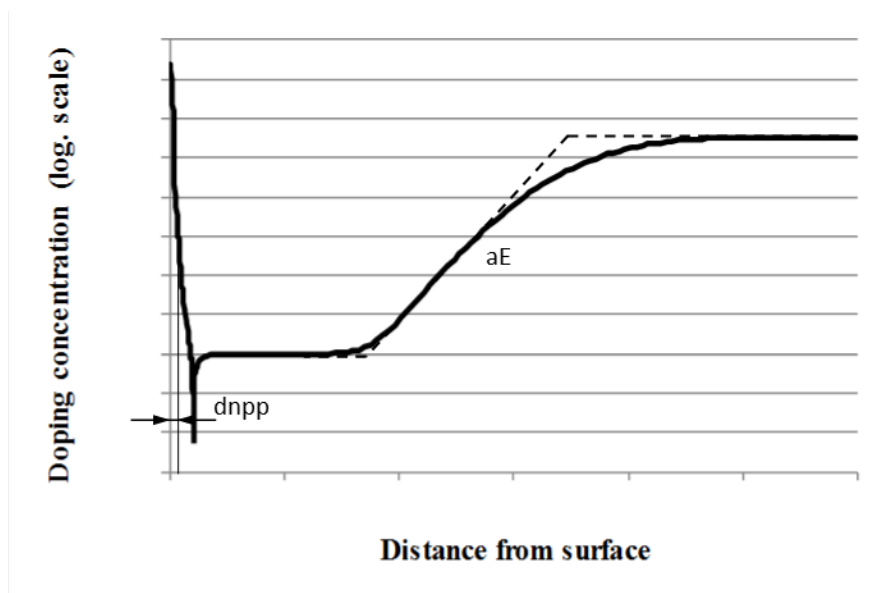


Figure 4.2: Exemplary doping profile to emphasize the position of $dnpp$ and aE . The parameter $dnpp$ sets the thickness of the heavily doped n-layer. The parameter aE sets the slope of the approximated doping profile.

aE is the relation between the slopes of the approximated and the real doping profiles in the transition layer. It therefore sets the slope of the approximated doping profile and its associated quantities. The mathematical representation of aE can be seen in

equation 3.54a. The sketch of a doping profile in figure 4.2 presents the position of aE inside the photodiode.

The approximated electric field in the transition layer must be greater than 0 and must not exceed the real electric field maximum. Thus aE is limited to values between 0 and 1.

ктаuns is a correction factor for the minority electron life time in the substrate. The principle data from literature used for modeling the life time is based on high purity silicon [11, 15, 16]. During production the wafer is doped and experiences several heating cycles. Thus the real life times differ from the ones given in literature. This can be considered by the parameter *ктаuns*.

ksrv scales the SRV at the silicon-ILD and the silicon-ARC interface, respectively. The values from literature are measured on high quality interfaces [11, 17]. However, a wafer undergoes several heat cycles during production. This influences the interface and therefore the surface recombination. The parameter *ksrv* accommodate for this effect.

4.2 Responsivity Parameter Extraction

The responsivity \mathfrak{R} is influenced by three parameters as pictured by figure 4.3. The initial values for $d\text{barc}$ can be obtained from the process parameter document. Likewise the doping profile is used for the initial value of $d\text{np}$. The value for aE has to be estimated. As discussed in the previous section 4.1 the value of aE has to be between 0 and 1. A value close to 1 is recommended. The parameters were changed by $\pm 50\%$ in the sensitivity analysis. The wavelength range is determined by the measurement equipment.

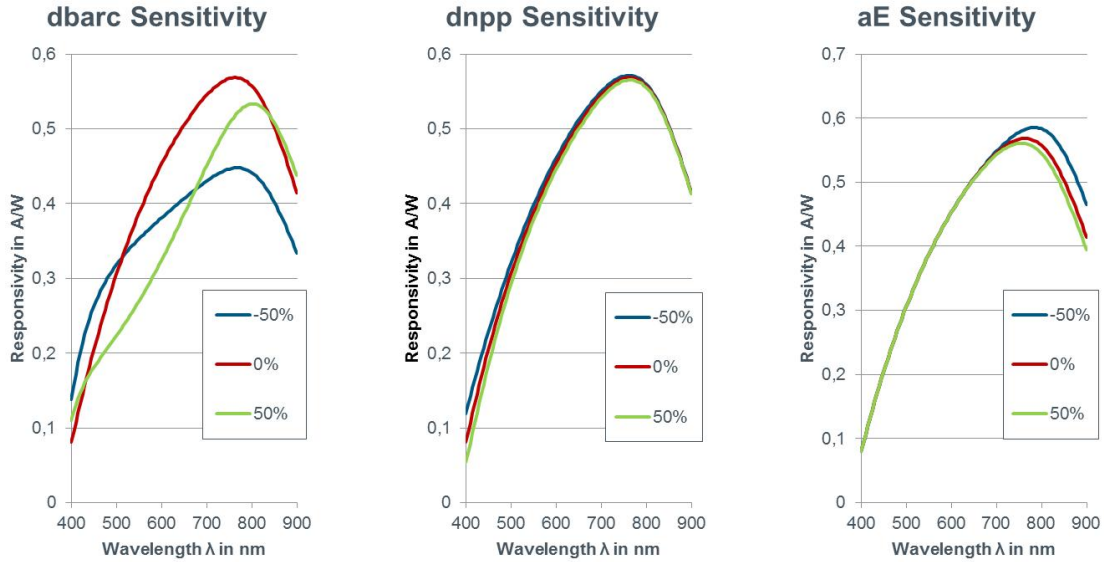


Figure 4.3: Responsivity parameter impact varying λ from 400 nm to 900 nm. left: $d\text{barc}$, middle: $d\text{np}$, right: aE

The parameter $d\text{barc}$ changes the principal shape of the responsivity, as shown in figure 4.3 left. It therefore will be the first parameter to be optimized to measurement readings. The parameters $d\text{np}$ and aE influence a different part of the responsivity, as they are associated to separated regions of the device as presented in figure 4.2. $d\text{np}$ impacts near to the top interface of the silicon while aE contributes to the behavior towards the substrate. As seen in section 2.1.1 the absorption coefficient is wavelength dependent. Short wavelength light is absorbed near the surface and long wavelength light penetrates deeper into the device. Therefore $d\text{np}$ changes the responsivity for short wavelength and aE for long wavelength as can be observed in the center and right hand side of figure 4.3. As $d\text{np}$ contributes to a larger wavelength range it will be optimized prior to aE . However the order can be varied for a different photodiode.

4.3 Frequency Response Parameter Extraction

The parameters impact on the magnitude of the frequency response $H(\omega)$ is investigated at two different wavelength of $\lambda = 670$ nm and $\lambda = 850$ nm. They are chosen in accordance with the available laser sources in the laboratory. The parameters with detectable influence on the frequency response are aE , $ktauns$ and $ksrv$. The parameters are varied by $\pm 50\%$ in the sensitivity analysis. The highest frequency of 10 GHz in the simulation is chosen to cover the measurable frequency band.

The simulation results for $\lambda = 670$ nm in figure 4.4 displays little influence of the parameters in the observed frequency range.

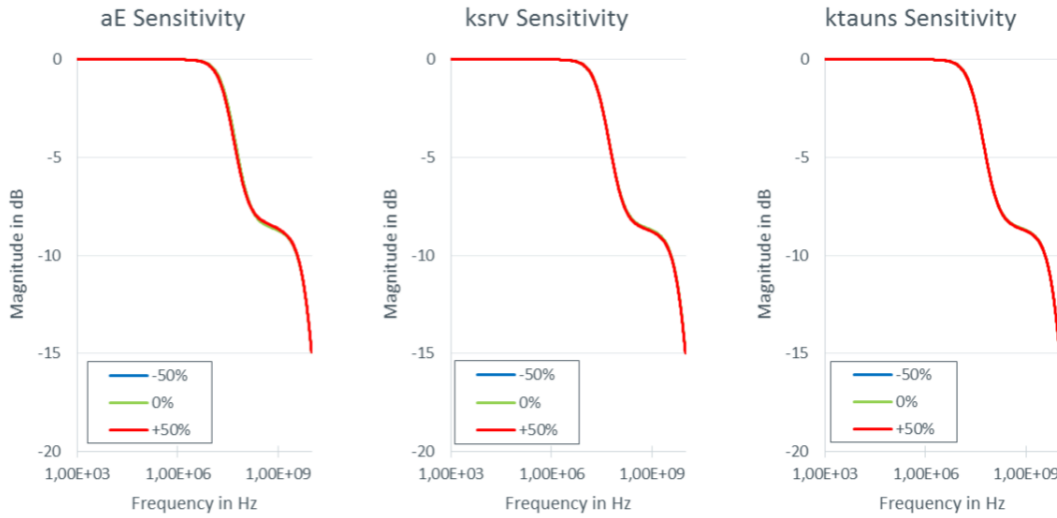


Figure 4.4: Frequency response parameter impact at $\lambda = 670$ nm in a logarithmic plot. left: aE , middle: $ksrv$, right: $ktauns$

The parameter impact on the magnitude of the frequency response at $\lambda = 850$ nm is plotted in figure 4.5. The magnitude shows a significant parameter dependence compared to the simulation at $\lambda = 670$ nm.

The difference in parameter impact between $\lambda = 670$ nm and $\lambda = 850$ nm is caused by the charge carrier distribution in the photodiode. At $\lambda = 670$ nm the charge carriers are generated closer to the depletion layer compared to a generation at $\lambda = 850$ nm. As the parameters aE and $ktauns$ change the properties near the substrate their influence is more pronounced at $\lambda = 850$ nm. As expected the attenuation is less for $\lambda = 670$ nm due to the fast response of the depletion layer.

$ksrv$ changes the properties next to the top surface. Both of the available wavelength generated a major fraction of charge carrier deeper inside the device. Thus the influence of $ksrv$ decreases. In order to investigate its impact more closely are short wavelength light source is needed.

The parameter impact at $\lambda = 670$ nm is insufficient for an extraction. Further discussion will therefore focus on $\lambda = 850$ nm.

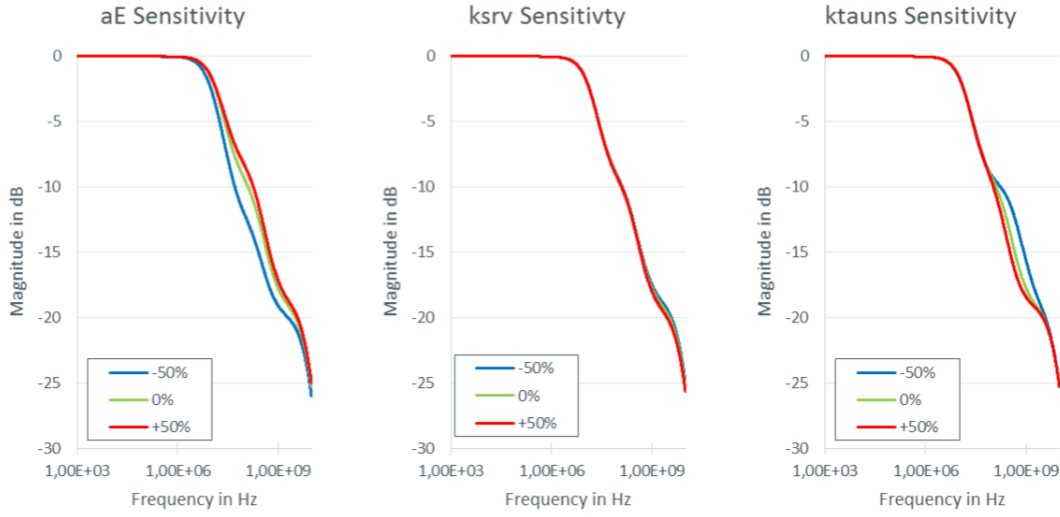


Figure 4.5: Frequency response parameter impact at $\lambda = 850$ nm in a logarithmic plot. left: aE , middle: $ksrv$, right: $ktauns$

The parameter aE changes the position of the drop-off, but also influences the responsivity. A trade-off between the responsivity and the frequency response fit with respect to the parameter aE has to be made.

The parameter for the surface recombination velocity $ksrv$ does not change the frequency response significantly. Therefore the parameter left for fitting is $ktauns$. As can be seen on the right hand side of figure 4.5 $ktauns$ sets the position of the second drop-off. There is no possibility to influence the frequency response in the lower frequency range. This results in difficulties in the fitting process as encountered in chapter 6.

4.4 Extraction Strategy

Table 4.1: The parameters are optimized in the given sequence.

Optimization Sequence	Parameter Category	Parameter Name
1	Process parameters	$N_0, N_E, N_S, L_N, L_{ES}, x_1, x_2, x_L, x_H, D_p, D_{nE}, D_{nS}, L_{nS}, \tau_p, \tau_n$
2	Instance parameters	Device dimensions (width W , length L , number of fingers n_F), T
3	Process parameter	d_{barc}
4	Fitting parameter	$dnpp$
5	Fitting parameter	aE
6	Fitting parameter	$ktauns$
7	Fitting parameter	$ksrv$

Chapter 5

Measurement of Photodiode Characteristics

The characteristics of photodiodes were discussed in section 2.2.2. This chapter covers the measurement of these aforementioned characteristics responsivity \mathfrak{R} and frequency response $H(f)$.

The device under test (DUT) is a p-i-n-photodiode implemented in a $0.35\ \mu\text{m}$ CMOS process. All measurements were performed on-wafer and at a nominal temperature $T_{Nom} = 27^\circ\text{C}$. The DUTs were contacted with needles on micromanipulators. A glass fiber was used to illuminate the photodiodes. Care has to be taken as ambient light must neither impinge on the photodiode nor on its surrounding area. During the measurement the wafer was placed into a light impenetrable prober and all unnecessary light sources in the laboratory were switched off. The microscope light must be turned off as well.

The prober and nearby measurement equipment is shown in figure 5.1. During the measurements the screens are turned off and the prober is covered with a black cloth.

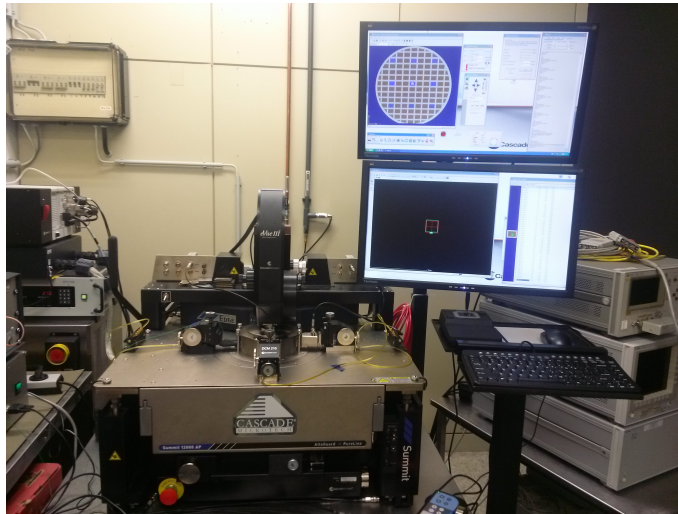


Figure 5.1: Photo of the opto-laboratory.

A photo of the wafer inside the prober with the optical fiber and two needles is presented in figure 5.2. The top plate and one of the side plates were removed and the microscope moved into its upper position for taking this photo. The fiber is marked with a green arrow and visible at the left hand side. The needles for electrical contact are indicated by a blue arrow. The wafer can be seen underneath and is marked with a white arrow.

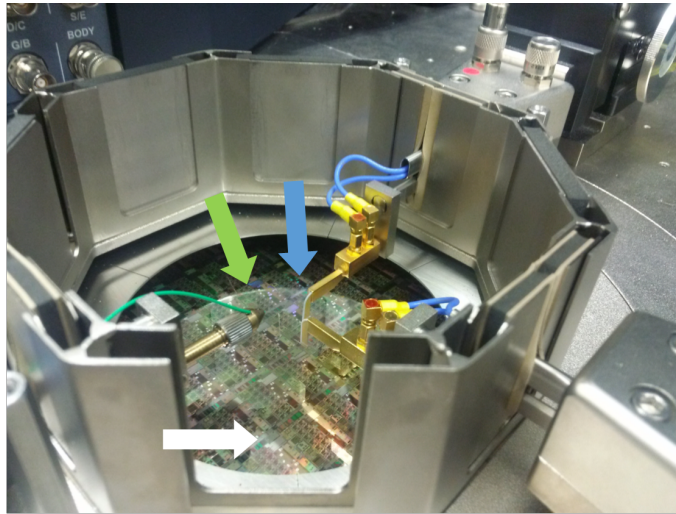


Figure 5.2: Photo of a wafer inside the prober. The green arrow on the left hand side indicates the fiber. The blue arrow on the right hand side marks the needles. The white arrow below points at the wafer.

The glass fiber is fixed on a micromanipulator and its cladding is removed. A lighter is used to heat the fiber and thus make it bendable. The fiber is bend until its tip points perpendicular to the wafer surface. A photo of the final assembly is presented in figure 5.3.

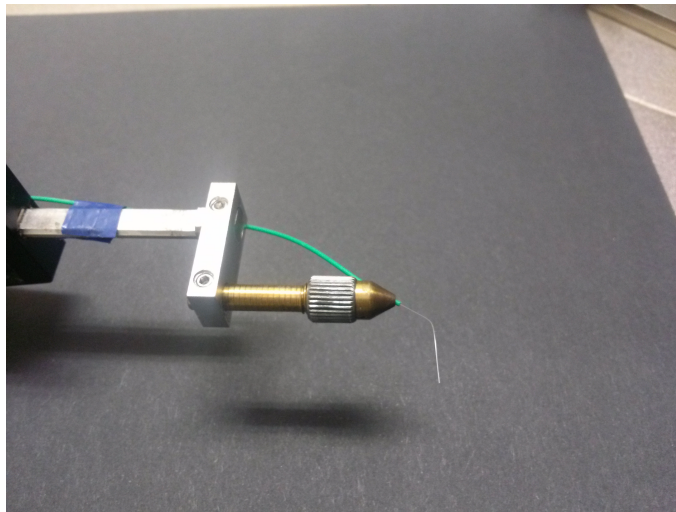


Figure 5.3: Photo of the fiber assembly.

The fiber should be placed close to the surface of the DUT without actually touching it.

The fiber may break or scratch the surface of the photodiode. Typically a microscope on a probestation offers no possibility to change its viewing angle. Hence the distance between fiber tip and wafer surface can not be seen directly. But the fiber tip becomes more detailed and defined as it approaches the surface. This can be used to estimate the distance between tip and wafer. A proper fiber position is shown in figure 5.4.

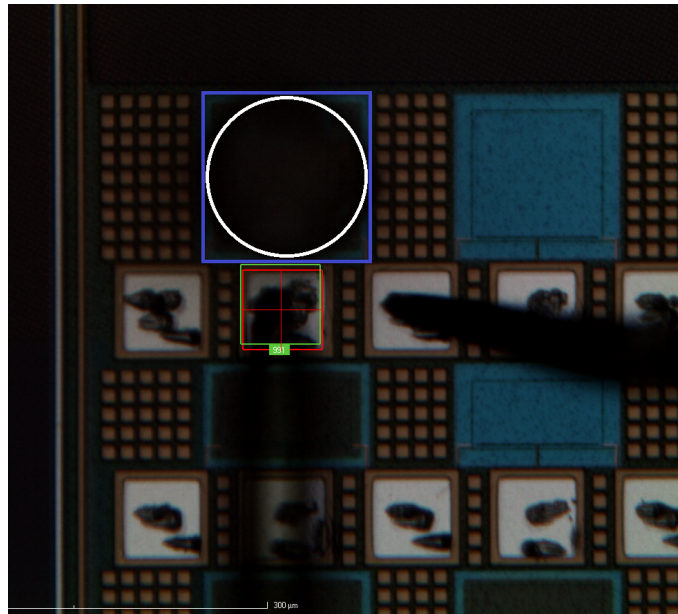


Figure 5.4: Fiber (white) position over a $150\ \mu\text{m} \times 150\ \mu\text{m}$ photodiode (blue) seen through the prober microscope. Also visible are the needles (black) used during responsivity measurements to contact the photodiode.

The rapid motion of the chuck when moving to the next DUT causes vibrations in the prober which are transferred to the fiber. Thus the fiber is possibly no longer aligned with the DUT after movement. Depending on the unsupported length of the fiber it may be necessary to lower the movement speed of the probestation.

5.1 Responsivity Measurement

The optical power and the reverse current of the illuminated photodiode are measured. This is done for a given set of wavelength λ . The recorded optical power and photodiode current at each wavelength are used in equation 2.50 to obtain the responsivity \mathfrak{R} over λ . The output wavelength of the tunable light source (TLS) ranges from $\lambda = 400$ nm to $\lambda = 900$ nm. The light source features an internal photodiode to monitor the optical power during measurements. This improves accuracy and reduces the impact of drift in long-term measurements.

Prior to the actual measurement the internal photodiode of the variable light source must be calibrated. The schematic calibration setup is illustrated in figure 5.5.

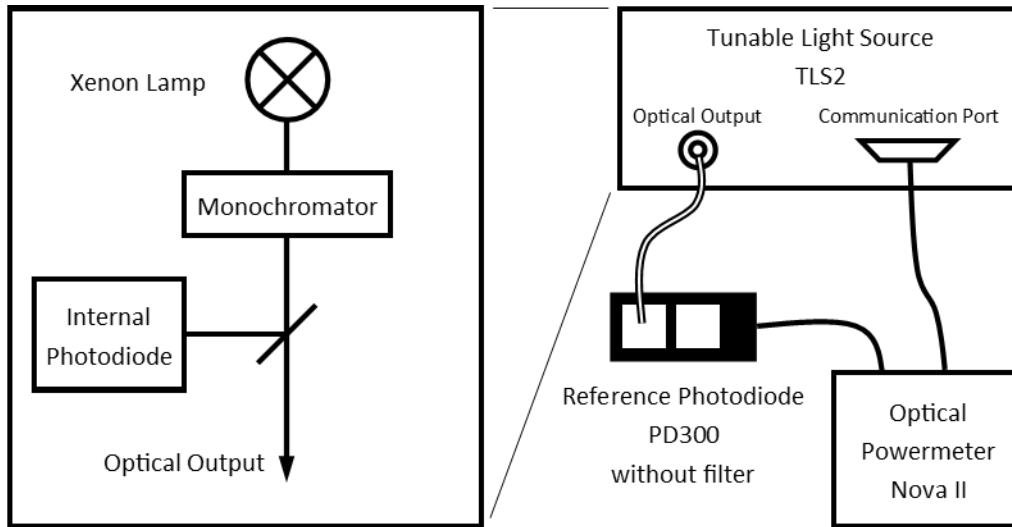


Figure 5.5: Schematic for the calibration of the tunable light source TLS2 internal photodiode.

The tunable light source is turned on and left to settle for about 15 minutes. The fiber is then positioned over a reference photodiode connected to an optical power meter. The reference photodiode is a differential type device. It features two photodiodes, where only the one on the far side of the connection cable is illuminated by the device to be calibrated. The second one measures the ambient light power in order to eliminate its influence. The reference photodiode comes with a removable filter. This filter has to be removed during calibration [18].

The light source offers a communication port for the optical power meter and stores the calibration data. The calibration is performed every $\Delta\lambda = 5$ nm from $\lambda = 400$ nm to $\lambda = 900$ nm. The calibration data is used to calculate the actual optical power from the monochromator during measurements. The calibration is a very sensitive stage. During the calibration run a change in illumination must not occur.

After calibration the fiber is placed above the DUT. The fiber is connected to the tunable light source and the contacts of the photodiode are connected to source-measurement-units (SMUs) of the parameter analyzer. A schematic of the setup is given in figure 5.6.

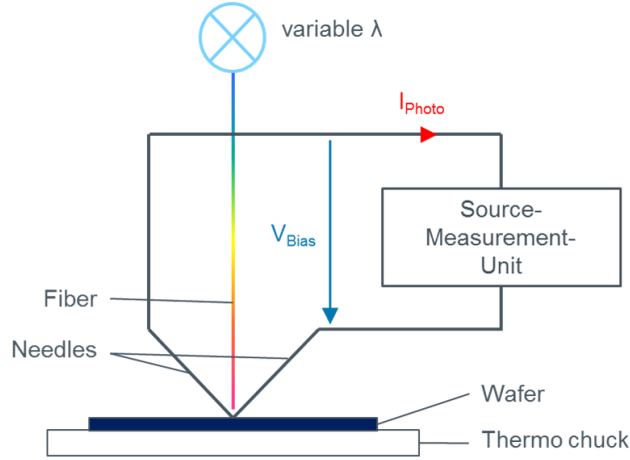


Figure 5.6: Schematic responsivity measurement setup.

A list of used equipment is given in table 5.1.

Table 5.1: List of equipment used for the responsivity measurement.

Type	Manufacturer	Model
Parameter Analyzer	Agilent	4156C
Optical Power Meter	Ophir	Nova II
Reference Photodiode	Ophir	PD 300
Tunable Light Source	A ³ PICs	TLS2

For responsivity measurements the bias voltage is constant and usually $V_{ac} = 0$ V. The current compliance must be set properly. In case the DUT is short-circuited due to a failure a high current flows. This may damage the needles or other components of the setup. A compliance of several μ A prevents damaging the equipment. The individual measurement devices are computer controlled. The program sets the wavelength and triggers the current sampling of the SMU. The number of samples per wavelength λ taken can be set by the user. The program calculates the average of all samples at a wavelength.

The measured current and the optical power spectrum are plotted in figure 5.7. Each individual data point is the average of three samples. Most of the features visible in the optical spectrum stem from the xenon lamp, e.g. the two peaks between $\lambda = 800$ nm and $\lambda = 900$ nm. The step at $\lambda = 650$ nm originates from the internal optical setup of the TLS. The internal grating is moved to change the order of interference, causing a change in irradiation [18, 8].

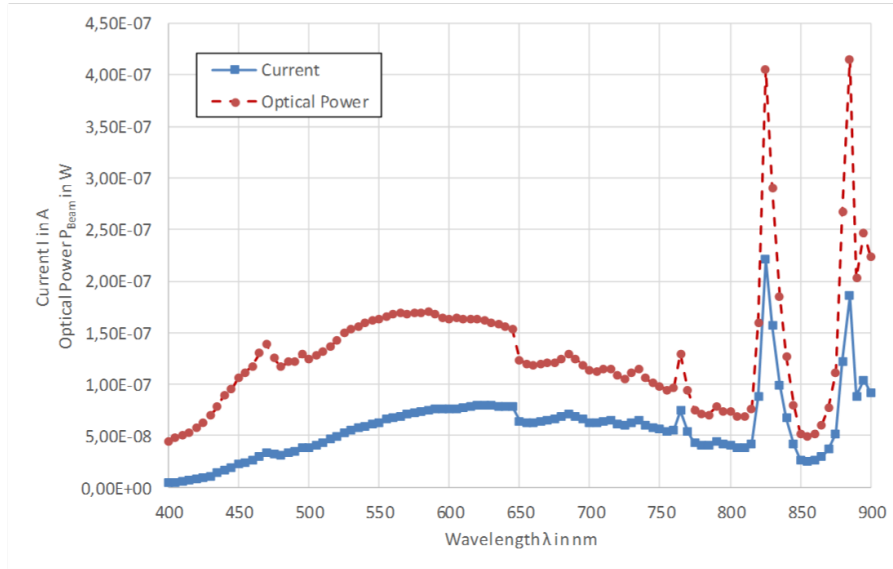


Figure 5.7: p-i-n-photodiode current and optical power for responsivity measurement from $\lambda = 400$ nm to $\lambda = 900$ nm in $\Delta\lambda = 5$ nm steps at $V_{ac} = 0$ V bias voltage.

Once the photocurrent and the optical power are obtained the responsivity \mathfrak{R} is calculated by equation 2.50. The resulting responsivity is plotted in figure 5.8.

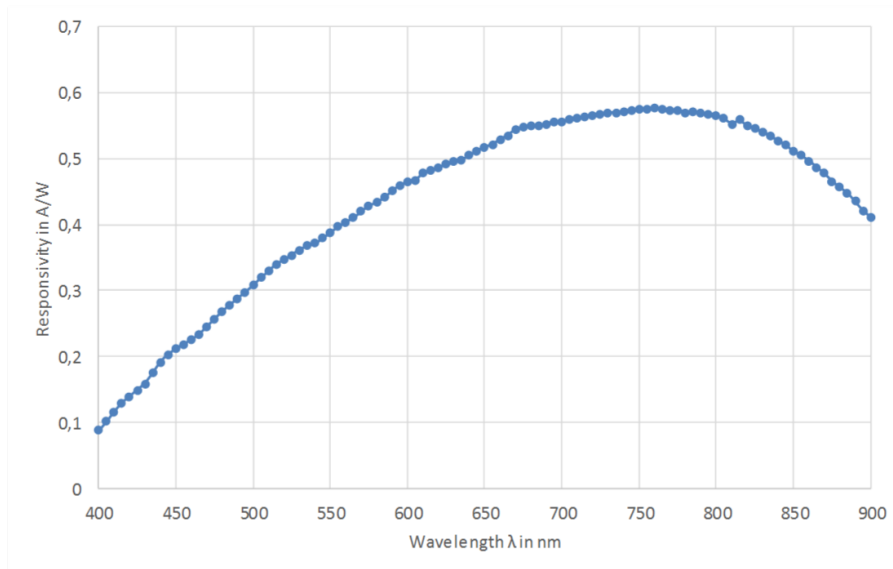


Figure 5.8: p-i-n-photodiode responsivity measurement result from $\lambda = 400$ nm to $\lambda = 900$ nm in $\Delta\lambda = 5$ nm steps at $V_{ac} = 0$ V bias voltage.

The responsivity is a smooth curve in the measured wavelength range. This is explained by the behavior of the BARC. Its single layer inhibits multiple reflections and interference. For comparison the calculated transmittance printed in figure 2.6 gives the same smooth

curve for an arbitrary BARC. A TARC would result in variations of responsivity over wavelength.

The responsivity \mathfrak{R} reaches a maximum value at around $\lambda = 750$ nm. The wavelength for this maximum responsivity can be controlled by two parameters. The first is the position of the p-n-junction. The second is the thickness of the BARC.

For shorter and longer wavelength either the transmittance T of the BARC decreases or more charge carriers recombine as they are generated at a larger distance from the depletion layer.

5.2 Frequency Response Measurement

Several papers deal with the measurement of the frequency response [19, 20, 21, 22]. The optical heterodyne detection uses two laser beams with different wavelength to generate an optical beat signal [19, 20]. However, this technique is mainly used to characterize photodiodes in optical communication systems. Their typical operation wavelength of $\lambda = 1,55 \mu\text{m}$ is beyond the wavelength range covered in this thesis. Furthermore optical modulators as utilized in [22] are mainly available for said wavelength. Electro-optical modulators for wavelength between $\lambda = 400 \text{ nm}$ and $\lambda = 900 \text{ nm}$ offer insufficient modulation frequencies of several MHz [23, 24].

Another method is called the pulse spectrum analysis (PSA). Short laser pulses are directed onto the photodiode and its response is measured. From the data the frequency response can be obtained. However, the accuracy of the result depends on the pulse width [19, 21]. The available equipment is not suited for this method. The laser source offers rise and fall times smaller than 350 ps as specified by the manufacturer [25]. But for a PSA the pulse width needs to be in the range of several ps.

The frequency response of integrated electronic devices is usually measured by a Vector Network Analyzer (VNA). This device applies a sinusoidal signal to the DUT and measures its response. Unfortunately the available laser source 'LS1' can not be modulated in a sinusoidal manner. A different approach has to be used.

The output of the laser source are square-shaped laser pulses. They are used to illuminate the photodiode while its response is measured in the time domain. Once the transient time response is recorded the frequency response is calculated by a Laplace transformation. A detailed derivation is given in appendix A. The fitting process in the time domain is not practicable. It would require a transient simulation of the model for each iteration during optimization. An AC simulation is performed faster. The frequency response is used in order to minimize the time required for an optimization run.

The measurement setup is schematically printed in figure 5.9.

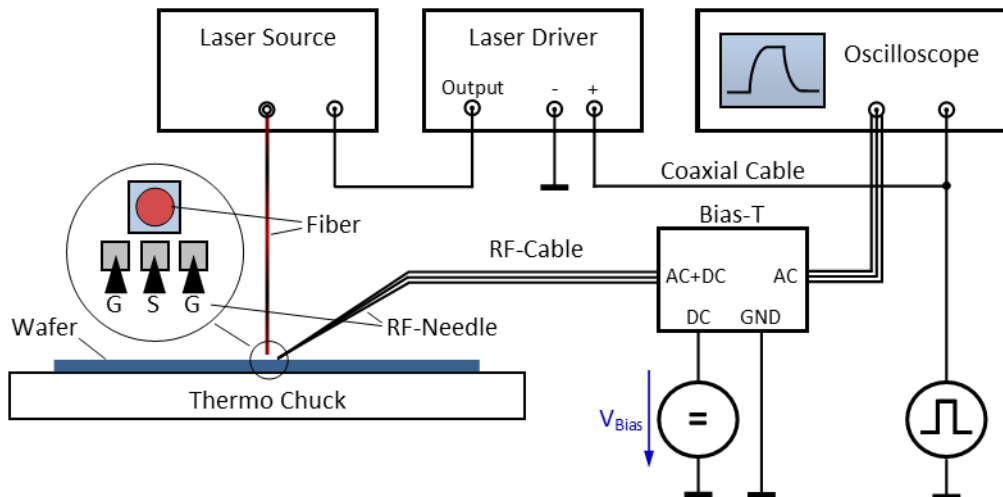


Figure 5.9: Schematic frequency response measurement setup.

The equipment used for the frequency response measurement is listed in table 5.2.

Table 5.2: List of equipment used for the frequency response measurement.

Type	Manufacturer	Model
Oscilloscope	Lecroy	SDA 760Zi-A
Laser Source	A ³ PICs	LS1
Digital Laser Driver	A ³ PICs	DLD1
Waveform Generator	Tabor Electronics	WW5061
Bias-T	Picosecond Pulse Labs	5546
DC Source	Agilent	E3631A

The laser source is not directly driven by the waveform generator. A laser driver is used to achieve the steep slopes and correct voltage levels needed to operate the laser source. The waveform generator output voltage is set to a square shaped signal with 50 % duty cycle. The waveform generator's amplitude is determined by the input limits of the digital laser driver ($V_{in,max} = \pm 400$ mV). For safe operation the amplitude is set to $V_{in} = \pm 250$ mV. The frequency must be selected in accordance with the bias-T. It is a bandpass filter and will influence the measurement at a too low frequency. Therefore a frequency high enough to pass the bias-T but at least a decade below the corner frequency of the photodiode has to be chosen. A frequency of 100 kHz is used for the measurement. An oscilloscope detects the response of the photodiode. Thus the current generated by the light pulses has to be transformed into a voltage. This voltage however changes the bias condition of the photodiode. The current slope for a zero-biased device is steeper than for a negatively-biased one. Therefore to minimize the impact of bias voltage changes the device is reversed-biased with $V_{ac} = 3$ V. This is close to the maximum operating voltage of $V_{GS,max} = 3.3$ V for MOS transistors in this process.

The maximum measurable frequency with the equipment listed in table 5.2 is limited by the oscilloscope to 6 GHz. Due to the high frequencies a special RF-needle and cables have to be used. Conventional coaxial cables are not suitable. They would lead to too much loss in signal amplitude at high frequencies. The needle is composed of three individual tips as shown in the inlay in figure 5.9. The outermost ones marked with 'G' are grounded. The needle between indicated with 'S' is the signal line. Thus the wire is shielded all the way to the contacts on the wafer.

However, during measurements interfering signals were detected. These occur randomly but are constant in amplitude and shape. A potential source is the in-house telephone system. To reduce the impact on the measurement the average function of the oscilloscope is used. The results were obtained by averaging 100 individual measurements. An additional benefit is the reduced impact of noise in the obtained data.

The equivalent circuit of the measurement setup is shown in figure 5.10.

Note that the potential decreases when the light is turned on. The current has to flow through the capacitor C due to its rapid change. The inductor L inhibits a fast current alteration. The oscilloscope detects a drop in voltage.

The measurement result in the time domain is given in figure 5.11 for $\lambda = 670$ nm and figure 5.12 for $\lambda = 850$ nm.

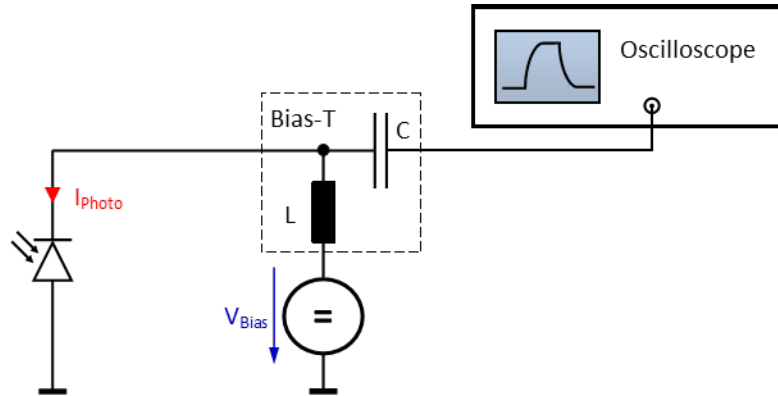


Figure 5.10: Equivalent circuit of the frequency response measurement setup.

The measurements for $\lambda = 670$ nm show a difference in light on and light off response. The light off response is a single steep slope while the light on response is an exponential drop-off. This asymmetric behavior can not be described with the model. Its transient response is caused by a combination of first order RC filters as given in section 3.3. Hence the model has a symmetric rise and fall sequence.

Contrary the response for $\lambda = 850$ nm is symmetric as given in figure 5.12.

The difference in light on and light off response at $\lambda = 670$ nm and the slow decrease after the initial slope at $\lambda = 850$ nm may indicate problems with the measurement setup. Multiple reflections along the fiber may have occurred.

The transient response of a photodiode features a fast and a slow component as detailed in chapter 2. The fast component is caused by the charge carriers in the depletion layer. The charge carriers generated in the quasi-neutral regions however take more time to reach their equilibrium value. The charge carriers have either to recombine or to diffuse to the depletion layer. The latter contributes to the current and causes the slow component of the transient response.

The measured data was fit by a combination of exponential functions. The number of exponential functions was increased until the fit matches the measured data. Three exponential functions are sufficient to achieve a fit. Before the fitting process was started the logarithm was applied to the amplitudes. Thus the fit for small values is improved. The obtained exponential functions are used to calculate the frequency response as given in appendix A. The fitted curves of the transient records are given in figure 5.13 for $\lambda = 670$ nm and figure 5.14 for $\lambda = 850$ nm.

The Bode plot obtained by the Laplace transform of the turn-on response for $\lambda = 670$ nm is printed in figure 5.15 and for $\lambda = 850$ nm in 5.16.

Comparing the two figures with each other shows a faster response of the photodiode on $\lambda = 670$ nm compared to $\lambda = 850$ nm. This is in accordance with the simulated frequency response discussed in section 4.3. At $\lambda = 670$ nm more charge carriers are generated near the depletion layer. This lowers the distance they have to travel by diffusion. An illumination with $\lambda = 850$ nm generates more charge carriers towards the substrate. The charge carriers have to diffuse over a larger distance and slow the response down.

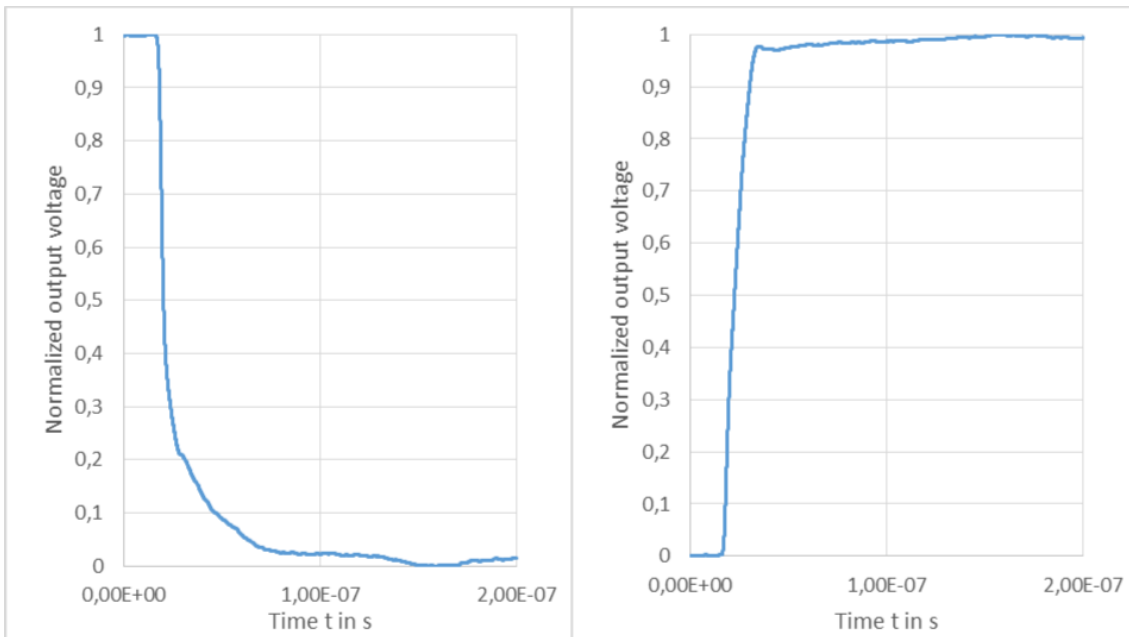


Figure 5.11: p-i-n-photodiode transient response measurement results for $\lambda = 670$ nm and a reverse bias-voltage of $V_{ac} = 3$ V. Left: Light turn on sequence. Right: Light turn off sequence.

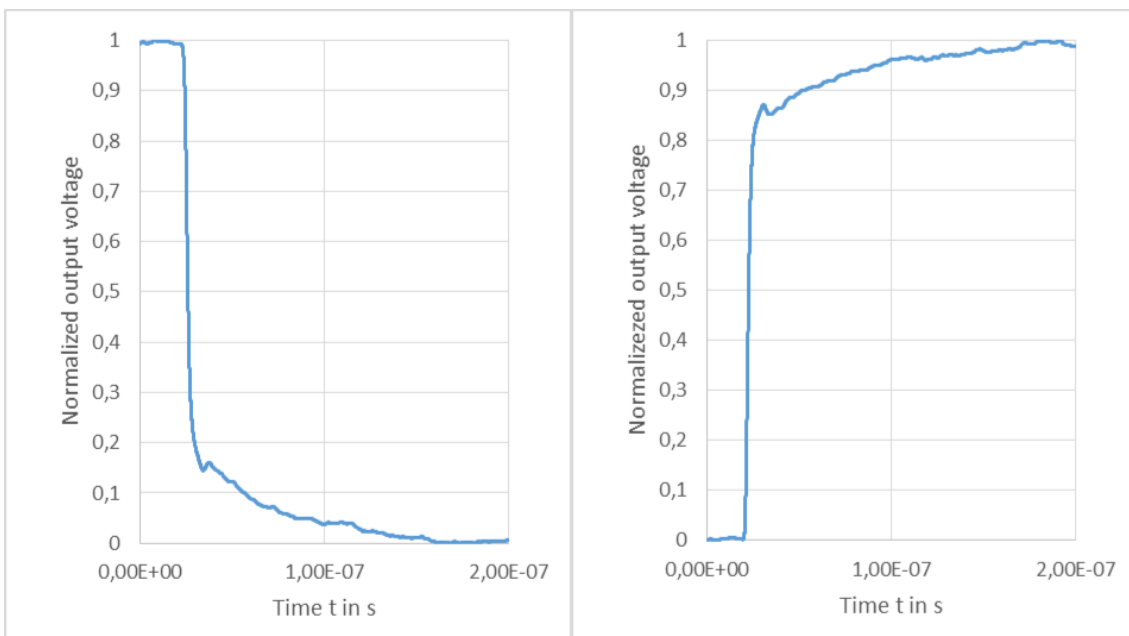


Figure 5.12: p-i-n-photodiode transient response measurement results for $\lambda = 850$ nm and a reverse bias-voltage of $V_{ac} = 3$ V. Left: Light turn on sequence. Right: Light turn off sequence.

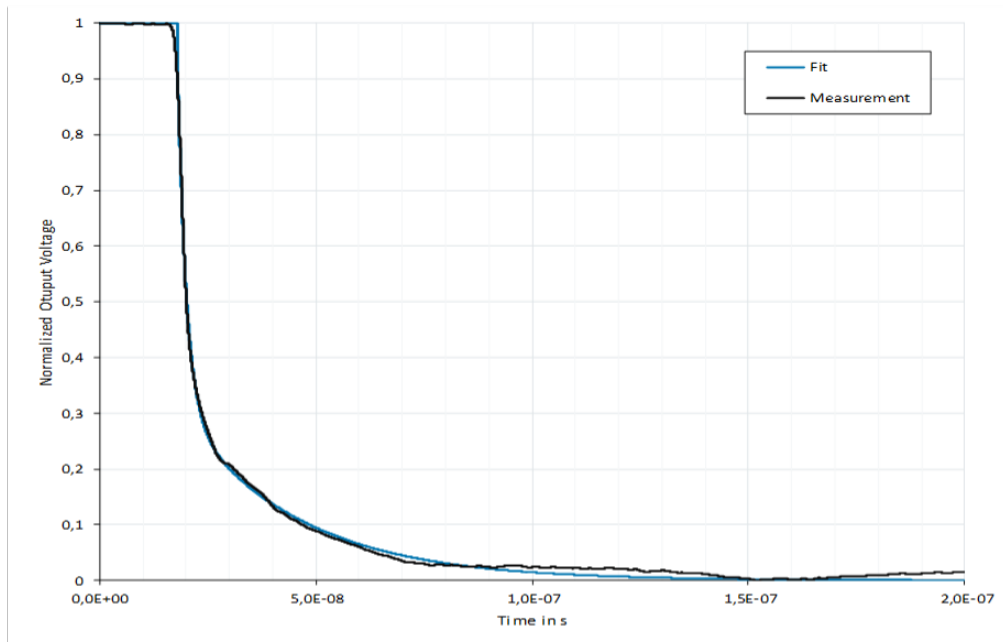


Figure 5.13: Fit of the p-i-n-photodiode transient response measurement results for $\lambda = 670$ nm using three exponential functions.

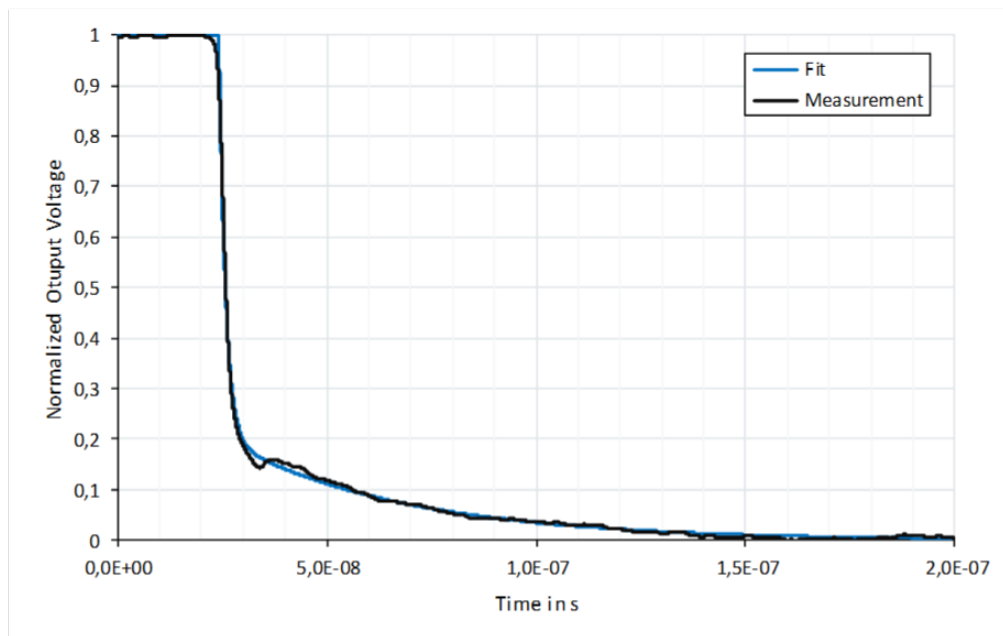


Figure 5.14: Fit of the p-i-n-photodiode transient response measurement results for $\lambda = 850$ nm using three exponential functions.

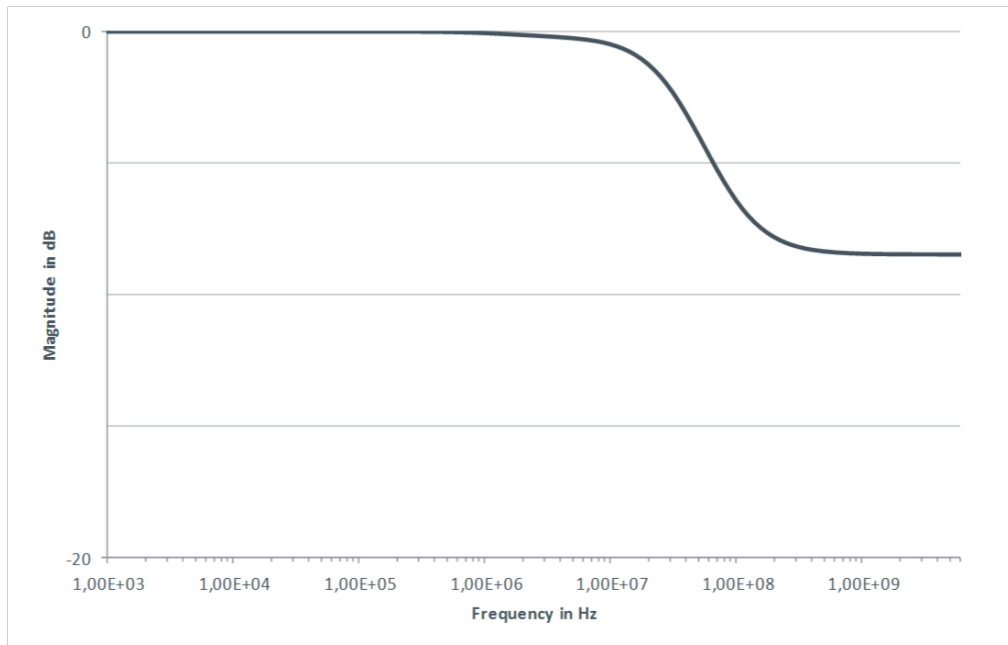


Figure 5.15: p-i-n-photodiode Bode plot for $\lambda = 670$ nm illumination obtained by Laplace transform of the transient data.

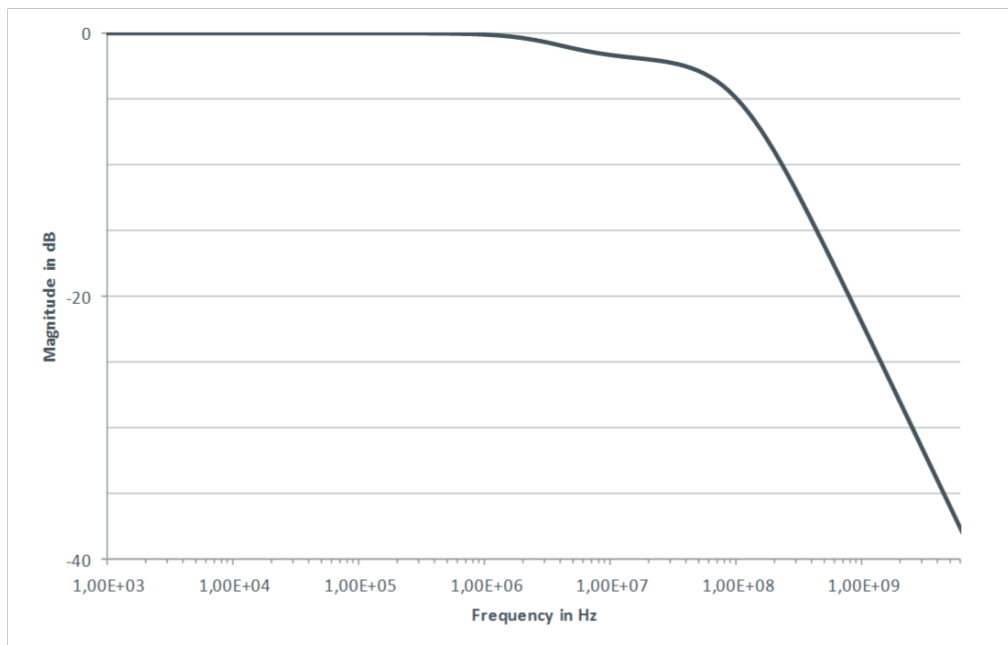


Figure 5.16: p-i-n-photodiode Bode plot for $\lambda = 850$ nm illumination obtained by Laplace transform of the transient data.

In figure 5.16 the slow and the fast component can easily be identified. The slow component has a time constant of approximately $1 \mu s$ and is close to the charge carrier lifetime in the substrate. The fast component's time constant is about 10 ns. It has to correspond to the charge carrier's travel time through the depletion layer. The travel time through the depletion layer can be estimated by the depletion layer thickness over the saturation velocity. This results in a travel time of 1 ps for a depletion layer width of $10 \mu m$. However, the fast component may exceed the limits of the measurement equipment. Thus the reported fast component is an upper limit to the real fast component.

Chapter 6

Parameter Optimization and Results

This chapter covers the determination of the model parameters. Furthermore the results are presented as a comparison between measurement readings and simulation. Mismatches between measurement and simulation as well as their origins are discussed.

The parameter extraction strategy deduced in chapter 4 is applied. The measurement data was obtained according to the methods detailed in chapter 5.

Furthermore a p-i-n-photodiode is used for the parameter extraction. As the model describes p-n-photodiodes it is not perfectly suitable for the chosen device. The depletion region extends into the heavily doped substrate. However, this study is used to evaluate the need for a special p-i-n-photodiode model and the limits of the currently available one. The characteristics of the photodiode were optimized by an Levenberg-Marquardt optimizer [26]. It compares the simulation result to the measurement readings by a least-squares method. The simulation results are obtained by a Spectre testbench. The circuit simulator is called and the result containing file loaded automatically by the program and handed over to the optimizer. The optimizer observes the changes in the characteristic and alters the parameters. This process is repeated until a certain deviation between measurement data and simulation result is achieved.

The optimizer offers the possibility to weight certain data ranges differently. The weights were set to unity during the optimization process. Hence no region was set apart. The weights can be used for special devices to focus on a particular wavelength range and frequency range, respectively.

6.1 Responsivity Fitting

The result of the Levenberg-Marquardt optimizer for the responsivity \mathfrak{R} is given in figure 6.1. The hollow circles represents the measurement readings. The fitted simulation results are printed as a solid line. The simulation results match the measurement readings with small deviations due to measurement uncertainties.

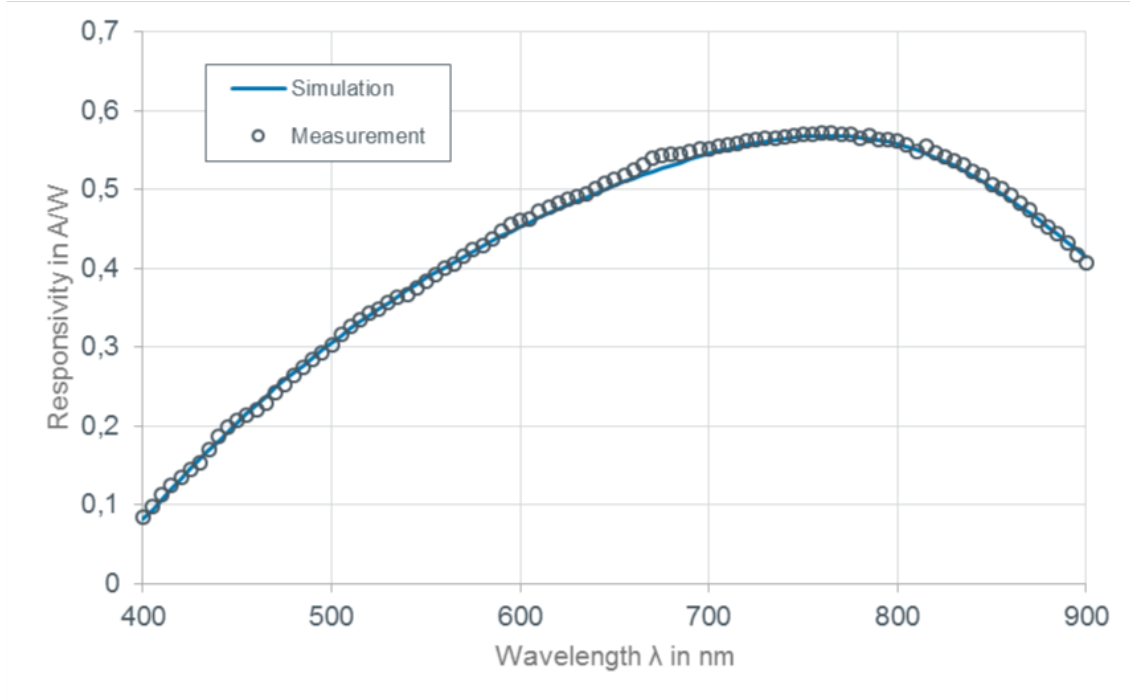


Figure 6.1: Fitted Responsivity.

The parameters obtained by the curve fitting of the responsivity are given in table 6.1.

Table 6.1: Model parameters obtained by fitting the responsivity \mathfrak{R} .

Parameter	Value
d_{barc}	8.3547E-2
d_{npp}	8.2825E-2
aE	7.7784E-1

6.2 Frequency Response Fitting

The parameter extraction of the frequency response discussed in section 4.3 gives no significant parameter impact for a wavelength of $\lambda = 670$ nm. Thus the optimization is done at $\lambda = 850$ nm. However, the curves for both wavelength are printed and discussed in this section.

The frequency response for $\lambda = 670$ nm is printed in figure 6.2. The hollow circles are obtained by measurement. The solid line represents the simulation results. Above 10 MHz there is a mismatch between simulation and measurement. At first the simulation gives higher magnitude and then drops below the measurement data at around 3 GHz.

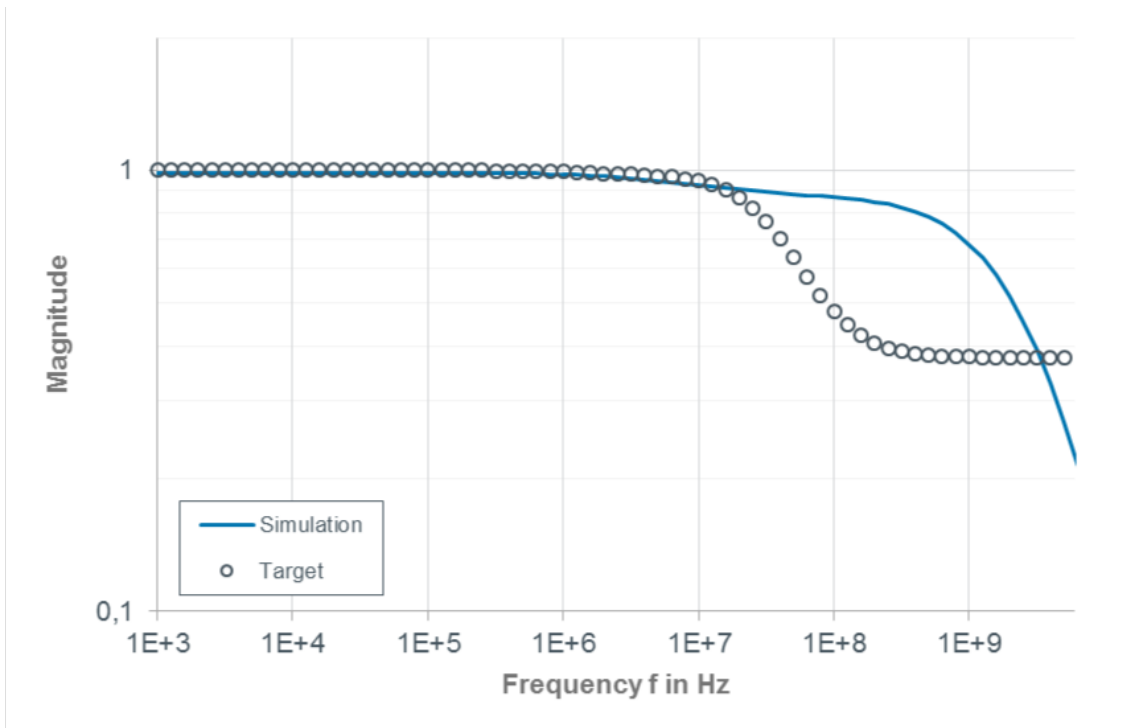


Figure 6.2: Frequency response for $\lambda = 670$ nm illumination.

Figure 6.3 shows the frequency response for $\lambda = 850$ nm. The hollow circles are the measured frequency response used as target for the fitting process. The solid line is the simulation results.

The parameters obtained by the frequency response fitting are given in table 6.2. The parameter $ksrv$ has little impact on the frequency response as discussed in section 4.3. This causes difficulties in convergence of the optimizer. Hence the parameter $ksrv$ is set to its default value of 0.

The deviation in the frequency response is severe. However the more interesting quantity for a circuit design is the transient response.

The simulation results are plotted along with measurement readings in figure 6.4 and 6.5 for $\lambda = 670$ nm and $\lambda = 850$ nm illumination, respectively.

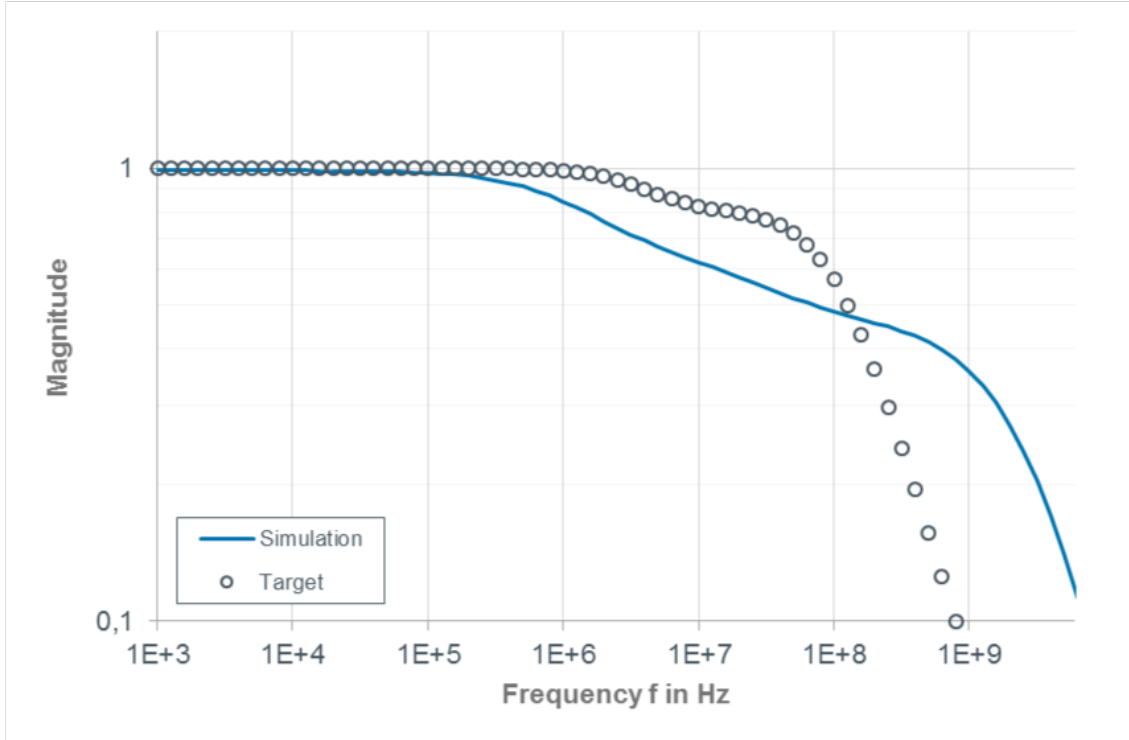


Figure 6.3: Fitted Frequency Response for $\lambda = 850$ nm illumination.

Parameter	Value
k_{tauns}	4,843E-3
k_{srv}	0

Table 6.2: Model parameters obtained by fitting the frequency response $H(f)$ at $\lambda = 850$ nm.

The initial slopes in the transient simulation for $\lambda = 850$ nm are quite accurate to the measurement results. The measured signal then slows down at 0.15 before reaching its final value. The reason for the deviation could be parasitic effects in the measurement setup, e.g. parasitic capacitance, the bias-T, instability of the laser source or multiple reflection of the laser. These effects have not been investigated so far. The rise and fall times for 20-80% however are considered accurate enough for use in a circuit simulator. The result for $\lambda = 670$ nm is not as close as the one for $\lambda = 850$ nm. The asymmetric behavior of the photodiode was already encountered in section 5.2. As expected the model is unable to mimic this effect. However, the obtained results for the transient response describe the qualitative behavior related to the wavelength λ , i.e. the photodiode responds faster on wavelengths which are absorbed closer to the depletion layer. The simulated transient response is sufficiently accurate for a first generation photodiode model. TCAD simulations were performed and compared to the measurement readings and model output. The results of all three do not agree with each other as shown in figure 6.6.

The reason was under investigation at the time this thesis was concluded.

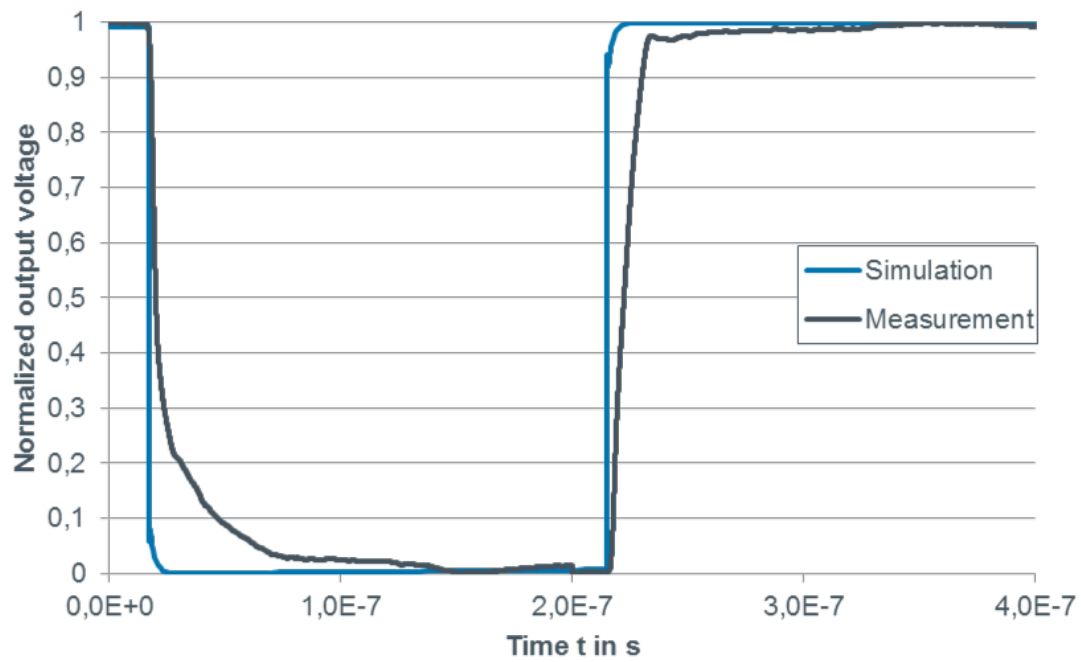


Figure 6.4: Transient response for $\lambda = 670$ nm illumination.

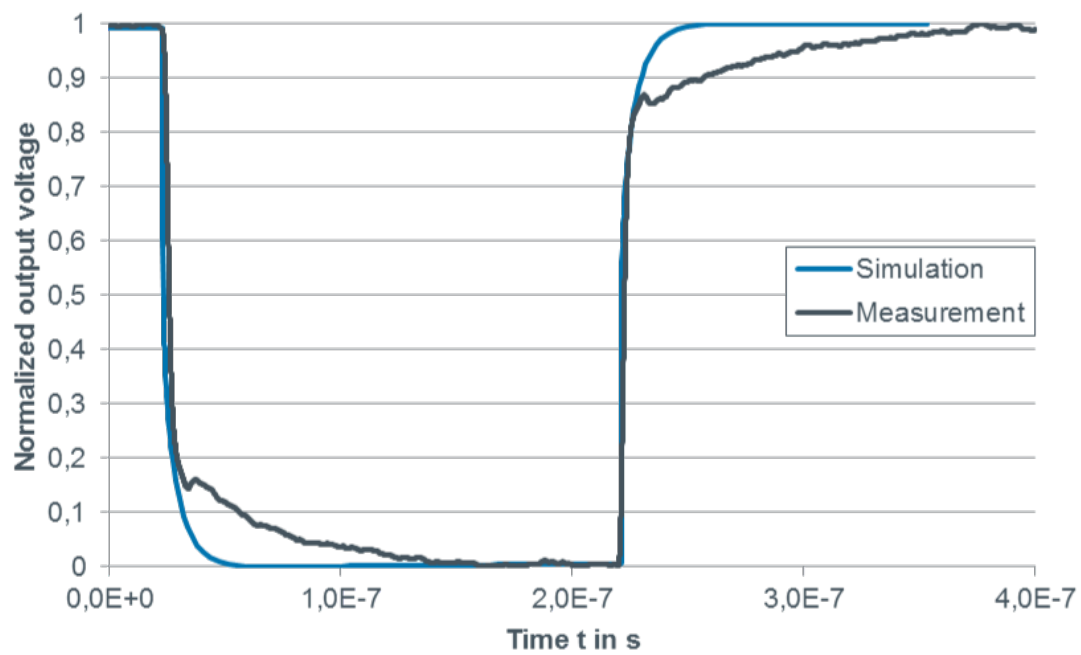


Figure 6.5: Transient response for $\lambda = 850$ nm illumination.

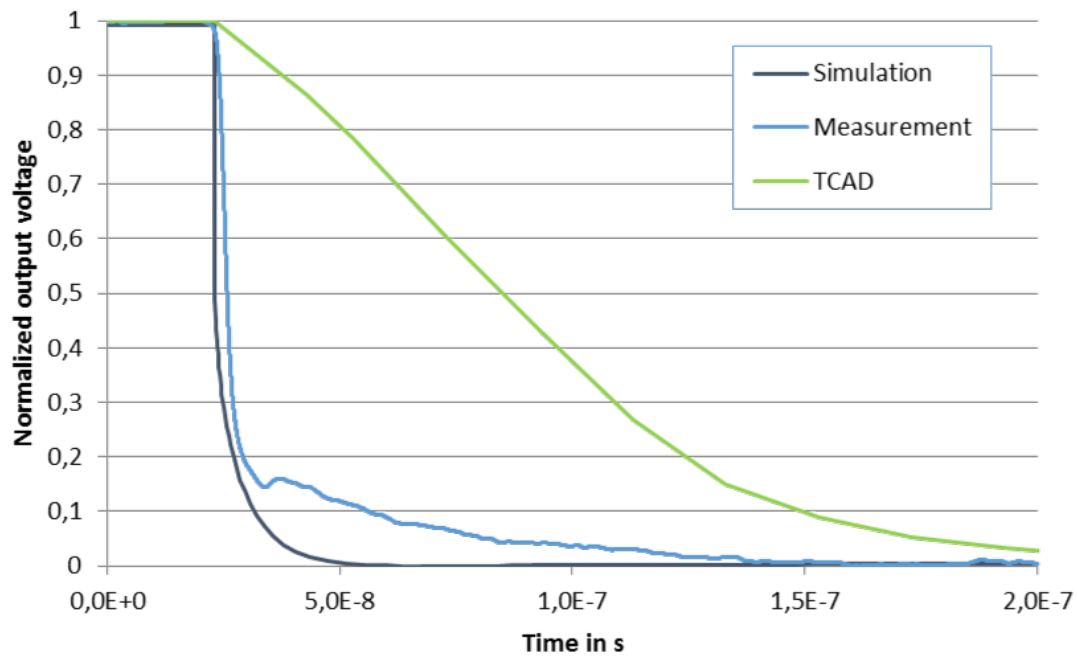


Figure 6.6: Comparison between measurement, model output and TCAD simulation of the transient response for $\lambda = 850$ nm illumination.

Chapter 7

Conclusion

State-of-the-art simulators able to calculate the opto-electronic phenomena in a photodiode are costly. They are expensive and the simulation takes a long time compared to circuit simulations. Special models are necessary to efficiently perform the calculations for circuit simulation. The verification of these models were discussed in this thesis. The assumptions and simplifications were investigated. The parameters for fitting the simulation results to measurement readings were covered and a parameter extraction strategy developed. A Levenberg-Marquardt algorithm was used to optimize the parameters. The parameters of future photodiodes can be optimized using the obtained parameter extraction strategy.

The capability of the p-n-photodiode model was investigated by using a p-i-n-photodiode as the device under test. The measurements of the major optical photodiodes characteristics responsivity and frequency response were discussed. Static quantities like the responsivity are well covered by the model. However major mismatches are encountered in the frequency response. These mismatches are considered acceptable for a first generation photodiode model.

The model enables circuit designers to simulate opto-electronic integrated circuits. Thus decreasing the development time, the risk of redesign and cost.

Bibliography

- [1] N. Desai, K. V. Hoang, and G. Sonek, “Applications of pspice simulation software to the study of optoelectronic integrated circuits and devices,” *Education, IEEE Transactions on*, vol. 36, no. 4, pp. 357–362, 1993.
- [2] T. Ezaki, G. Suzuki, K. Konno, O. Matsushima, Y. Mizukane, D. Navarro, M. Miyake, N. Sadachika, H. Mattausch, and M. Miura-Mattausch, “Physics-based photodiode model enabling consistent opto-electronic circuit simulation,” in *Electron Devices Meeting, 2006. IEDM’06. International*. IEEE, 2006, pp. 1–4.
- [3] W.-J. Liu, O.-C. Chen, L.-K. Dai, P.-K. Weng, K.-H. Huang, and F.-W. Jih, “A cmos photodiode model,” in *Behavioral Modeling and Simulation, 2001. BMAS 2001. Proceedings of the Fifth IEEE International Workshop on*, 2001, pp. 102–105.
- [4] T. Naeve, M. Hohenbild, and P. Seegrebrecht, “A novel physically based photodiode model for optoelectronic circuit simulations,” in *Electron Devices for Microwave and Optoelectronic Applications, 2003. EDMO 2003. The 11th IEEE International Symposium on*, 2003, pp. 163–169.
- [5] T. Naeve and P. Seegrebrecht, “A physical based photodiode model,” in *Optoelectronic and Microelectronic Materials and Devices, 2006 Conference on*, 2006, pp. 228–231.
- [6] R. Perry and K. Arora, “Using pspice to simulate the photoresponse of ideal cmos integrated circuit photodiodes,” in *Southeastcon ’96. Bringing Together Education, Science and Technology., Proceedings of the IEEE*, 1996, pp. 374–380.
- [7] L. Ravezzi, G.-F. Dalla Betta, D. Stoppa, and A. Simoni, “A versatile photodiode spice model for optical microsystem simulation,” *Microelectronics journal*, vol. 31, no. 4, pp. 277–282, 2000.
- [8] M. Born and E. Wolf, *Principles of optics: electromagnetic theory of propagation, interference and diffraction of light*. CUP Archive, 1999.
- [9] S. M. Sze and K. K. Ng, *Physics of semiconductor devices*. Wiley. com, 2006.
- [10] C. Weißmantel, C. Hamann, and H. Burghardt, *Grundlagen der Festkörperphysik*. Springer Berlin, Heidelberg, New York, 1979.
- [11] Z. Huszka, “Spice modeling of photodiodes,” 2013, unpublished.

- [12] N. Arora, *MOSFET Models for VLSI Circuit Simulation: Theory and Practice*. Se-caucus, NJ, USA: Springer-Verlag New York, Inc., 1993.
- [13] Y. Cheng and C. Hu, *MOSFET modeling & BSIM3 user's guide*. Springer, 1999.
- [14] G. Gildenblat, *Compact Modeling: Principles, Techniques and Applications*. Springer, 2010.
- [15] M. Law, E. Solley, M. Liang, and D. Burk, "Self-consistent model of minority-carrier lifetime, diffusion length, and mobility," *Electron Device Letters, IEEE*, vol. 12, no. 8, pp. 401–403, Aug 1991.
- [16] K. A. Moen, "Modeling of minority carrier recombination and resistivity in sige bic-mos technology for extreme environment applications," 2008.
- [17] R. King, R. Sinton, and R. Swanson, "Studies of diffused phosphorus emitters: saturation current, surface recombination velocity, and quantum efficiency," *Electron Devices, IEEE Transactions on*, vol. 37, no. 2, pp. 365–371, 1990.
- [18] *A³PICs Tunable Light Source TLS2*, A³PICs Electronics Development GmbH, Melde-mannstrasse 18, A-1200 Vienna, Austria, 2011.
- [19] S. Kawanishi, A. Takada, and M. Saruwatari, "Wideband frequency-response mea-surement of optical receivers using optical heterodyne detection," *Lightwave Technol-ogy, Journal of*, vol. 7, no. 1, pp. 92–98, Jan 1989.
- [20] R. Schimpe, J. Bowers, and T. Koch, "Characterisation of frequency response of 1.5 um ingaasp dfb laser diode and ingaas pin photodiode by heterodyne measurement technique," *Electronics Letters*, vol. 22, no. 9, pp. 453–454, April 1986.
- [21] A. Singh, "Impact of optical pulsewidth on the frequency response of p-i-n photodi-odes," *Photonics Technology Letters, IEEE*, vol. 22, no. 8, pp. 589–591, April 2010.
- [22] T. Tangmala, S. Potha, U. Mankong, K. Inagaki, and T. Kawanishi, "Optoelectronic frequency response measurement using standard mach-zehnder modulator," in *Optical Communications and Networks (ICOCN), 2012 11th International Conference on*, Nov 2012, pp. 1–4.
- [23] "Thorlabs , Inc." <http://www.thorlabs.de/>, accessed: 2014-10-06.
- [24] "Qubig GmbH," <http://www.qubig.com/index.htm>, accessed: 2014-10-06.
- [25] *A³PICs Laser Source LS1*, A³PICs Electronics Development GmbH, Melde-mannstrasse 18, A-1200 Vienna, Austria, 2011.
- [26] W. H. Press, *Numerical recipes 3rd edition: The art of scientific computing*. Cam-bridge university press, 2007.

Appendix A

Laplace Transformation of Transient Response

The Laplace transform is used to obtain the frequency response of the measured transient signal. It is given as

$$\mathcal{F}(\omega) = \mathcal{L}(f(t)) = \int_0^{\infty} f(t) \cdot e^{-s \cdot t} dt$$

The photodiode is illuminated by square-shaped light pulses. This signal can be written as a sequence of step functions. Defining the step or Heavyside function ς

$$\varsigma(t) = \begin{cases} 1 & \text{if } t \geq 0 \\ 0 & \text{if } t < 0 \end{cases} \quad (\text{A.1})$$

A Heavyside-shaped signal is transformed to

$$\mathcal{L}(\varsigma(t)) = \int_0^{\infty} e^{-s \cdot t} dt$$

$$\mathcal{L}(\varsigma(t)) = -\frac{1}{s} \cdot e^{-s \cdot t} \Big|_0^{\infty}$$

$$\mathcal{L}(\varsigma(t)) = \frac{1}{s} \quad (\text{A.2})$$

The step response current of the photodiode is assumed to be composed of exponential functions starting at $t = 0$ s.

$$I_{on}(t) = \sum_{k=1}^K a_k^2 \cdot \left(1 - e^{-\frac{t}{\tau_k}}\right) \cdot \zeta(t) \quad (\text{A.3})$$

Where K gives the order of the approximation. Using the Laplace transform results in

$$\begin{aligned} \mathcal{L}(I_{on}(t)) &= \int_0^\infty \sum_{k=1}^K a_k^2 \cdot \left(1 - e^{-\frac{t}{\tau_k}}\right) \cdot \zeta(t) \cdot e^{-s \cdot t} dt \\ \mathcal{L}(I_{on}(t)) &= \sum_{k=1}^K a_k^2 \cdot \left(-\frac{1}{s}\right) \cdot e^{-s \cdot t} \Big|_0^\infty - \sum_{k=1}^K a_k^2 \cdot \left(-\frac{1}{\frac{1}{\tau_k} + s}\right) \cdot e^{-\frac{1}{\tau_k + s} \cdot t} \Big|_0^\infty \\ \mathcal{L}(I_{on}(t)) &= \sum_{k=1}^K a_k^2 \cdot \frac{1}{s} - \sum_{k=1}^K a_k^2 \cdot \frac{1}{\frac{1}{\tau_k} + s} \\ \mathcal{L}(I_{on}(t)) &= \sum_{k=1}^K a_k^2 \cdot \frac{1}{s} - a_k^2 \cdot \frac{\tau_k}{1 + s \cdot \tau_k} \end{aligned} \quad (\text{A.4})$$

Merging the two terms in equation A.4 results in

$$\begin{aligned} \mathcal{L}(I_{on}(t)) &= \sum_{k=1}^K a_k^2 \cdot \frac{1}{s} - a_k^2 \cdot \frac{\tau_k}{1 + s \cdot \tau_k} \\ \mathcal{L}(I_{on}(t)) &= \sum_{k=1}^K a_k^2 \cdot \frac{1 + s \cdot \tau_k}{s \cdot (1 + s \cdot \tau_k)} - a_k^2 \cdot \tau_k \cdot \frac{s}{s \cdot (1 + s \cdot \tau_k)} \\ \mathcal{L}(I_{on}(t)) &= \sum_{k=1}^K \frac{1}{\tau_k} \cdot \frac{1}{s} \cdot \frac{a_k^2}{s + \frac{1}{\tau_k}} \end{aligned} \quad (\text{A.5})$$

The transfer function in the complex frequency domain $H(s)$ is given by the output (equation A.5) over the input quantity (equation A.2).

$$\begin{aligned} H(s) &= \frac{\mathcal{L}(I_{on}(t))}{\mathcal{L}(\zeta(t))} \\ H(s) &= \sum_{k=1}^K \frac{1}{\tau_k} \cdot \frac{a_k^2}{s + \frac{1}{\tau_k}} \end{aligned} \quad (\text{A.6})$$

The time constants τ_k and the coefficients a_k^2 are used to fit the approximated transient response in equation A.3 to measurement readings. For normalized signals the coefficients sum has to be unity.

$$\sum_{k=1}^K a_k^2 = 1 \quad (\text{A.7})$$

Thus there are $K - 1$ independent variables which have to be optimized according to measurement results. The coefficients are collected into an unit vector.

$$\mathbf{a}_K = [a_1, a_2 \dots a_K]$$

Using the vector notation equation A.7 becomes

$$\mathbf{a}_K \cdot \mathbf{a}_K^T = 1$$

The coefficients of the unit vector are its projections on the axes. They are expressed as the angles φ from the axes. For different orders K the individual coefficients become

$$\begin{aligned} K = 1 : a_1 &= 1 \\ K = 2 : a_1 &= \cos(\varphi_2) & a_2 &= \sin(\varphi_2) \\ K = 3 : a_1 &= \cos(\varphi_3) & a_2 &= \sin(\varphi_3) \cdot \cos(\varphi_2) & a_3 &= \sin(\varphi_3) \cdot \sin(\varphi_2) \end{aligned}$$

For a general K the unity vector can be obtained by

$$\mathbf{a}_K = [\cos(\varphi_K), \sin(\varphi_K) \cdot \mathbf{a}_{K-1}]$$

The measurement data of the photodiode is approximated using equation A.3 and $K = 3$. Thus 5 quantities ($\varphi_2, \varphi_3, \tau_1, \tau_2, \tau_3$) have to be fitted. The resulting values are used to obtain the transfer function by equation A.6.